STRESS MONITORING OF CYLINDRICAL STRUCTURES USING GUIDED WAVES

Jabid E. Quiroga Méndez

Director: Luis Mujica

Co-director: Rodolfo Villamizar

This dissertation is submitted for the degree of
Doctor in Civil Engineering

April 2018

I would like to dedicate this thesis to my wife Juliana Alvarez

Declaration

I hereby declare that except where specific reference is made to the work of others, the contents of this dissertation are original and have not been submitted in whole or in part for consideration for any other degree or qualification in this, or any other university. This dissertation is my own work and contains nothing which is the outcome of work done in collaboration with others, except as specified in the text and Acknowledgements.

Jabid E. Quiroga Méndez
April 2018

Acknowledgements

I would like to acknowledge to my supervisors Professor Luis E. Mujica and Rodolfo Villamizar whithout whom this work wouldn't have been possible. I would like to thank them for encouraging my research and for allowing me to grow as a research scientist. I will appreciate all they have done for me forever. I owe my deepest gratitude to Control, Dynamics and Applications (CoDAlab) and its all members for all valuable days that I spent working in this group. I would like to show my greatest appreciation to reviewers of my thesis Professor Ekhi Zugasti Uriguen from University of Mondragon and Professor Miguel Díaz from Andes University for their brilliant comments, suggestions and feedbacks. Special thanks to the Colombian government through its department Colciencias for the grant that allowed me stayed in Barcelona and to complete this thesis. Finally, I am grateful to the tribunal members, professor Fernando Martínez Rodríguez from IKERLAN, professor Franscesc Pozo Montero and Yolanda Vidal from Universitat Politècnica de Catalunya and professor Antonio Fernández López from Escuela Técnica Superior de Ingeniería Aeronáutica y del Espacio, Universidad Politécnica de Madrid

Abstract

This thesis presents some approaches for guided wave based stress monitoring as a part of Structural Health Monitoring (SHM). SHM systems include different levels, from damage detection to prognosis, however, this work is focused on detection and on an estimation of the actual stress. The proposed stress monitoring strategies are based on different statistical and signal processing approaches such as Principal Component Analysis and Residuals. These techniques are applied on signals of elastic guided waves generated and sensed via Piezoelectrical (PZT) or Magnetostrictive transducers. Transducer devices are chosen in this work to generate longitudinal, flexural and torsional guided waves in cylindrical specimens, since their high performance, low energy consumption, weight and reasonable price. In order to guarantee the efficacy of the proposed techniques, they are tested in laboratory by emulating real installations and abnormal conditions. Experimental tests revealed that temperature and bonding layer between the PZT and the specimen influence on the performance of the monitoring scheme by changes in the guided wave propagation. Thus, the temperature effect on guided wave propagation was examined by checking the sensitivity of the PCA-based proposed approach. Then, a temperature compensation strategy is applied to improve stability and robustness of the scheme for structures subjected temperature changes.

On the other hand, since the acoustoelasticity effect is predominant in the propagation of stressed guided waves, it was observed its incidence on the dispersion curves by using a SAFE method (Semi-Analytical Finite Element) to generate stressed dispersion curves via Effective Elastic Constants (EEC).

Finally, as a consequence of some observations in the experimentation stage, it is proposed a scheme for monitoring the supports rigidity in pipelines based on a guided waves energy leakage perspective. The proposed approaches may promise the ability and capability of being implemented in different fields such as aerospace and gas/oil industry.

Table of contents

List of figures

Chapter 1

Introduction

1.1 Research Motivation

According to [10], "Structural Health Monitoring (SHM) is the integration of sensing and possibly also actuation devices to allow the loading and damaging conditions of a structure to be recorded, analyzed, localized, and predicted in a way that nondestructive testing (NDT) becomes an integral part of the structure and a material". Some of the benefits obtained by implementing SHM systems are breakdowns avoidance, reduction of time and maintenance costs, continuous remote diagnosis and economic benefits in terms of operational life extension.

On the other hand, the high demand of energy has increased the attention on Oil and Gas industries; particularly, exploration, production and consequently transportation of hydrocarbons. Monitoring of extracting, transportation, storage and refining facilities is highly complex, but it is an essential and fundamental task. Pipelines in service are continuously affected by different factors such as: corrosion, erosion, chemical attack, stress, fatigue, extreme climate conditions. Therefore, it is imperative to develop and implement fast and accuracy tools for pipeline monitoring to improve both safety and environmental aspects.

Structural monitoring usually involves the use of either NDT techniques or SHM. Some NDT methods as ultrasonic thickness gauging, radiography, eddy current, thermography, and magnetic flux are commonly used for testing pipes but they are time demanding for covering the whole installation.

Nowadays, screening of pipelines by using guided waves is gaining attention. This technique is fast, accurate and costly effective. The use of this high-covered scheme can identify potential areas of discontinuities or abnormal conditions, enabling the accomplishment of a reliable detection and reduction of monitoring costs.

The presence of mechanical stresses in pipelines has great influence in their operation in issues such as strength, expected operational life and dimensional stability. Some stresses in the pipeline are developed during service and they are difficult to identify and diagnose because they can unexpectedly appear and turn into invisible due to the apparent absence of an external load (such as the associated with the loss of rigidity between the support and ground).

Stress in a structural element can be measured by using either non-destructive or destructive methods. Destructive methods are based on measuring the strain relaxation (change of length), when a part of an element in service is removed. This method is expensive in real installations due to the high costs that represent the production stoppage. On the other hand, the use of strain gauges is one of the most common non-destructive methods to measure relative surface stress.

Strain gages are limited to determine stress changes i.e. the variation of the stress respect to the initial stress condition (after the sensor is attached to the element). Thus, they cannot be directly used to measure, for example, residual stresses introduced in the manufacture or the stress state of a previously without instrumentation structure. Additionally, the use of the strain gauge is limited to determine the strain in a specific position, which is a disadvantage when the specimen is subjected to variable stress in magnitude and position, as the case of a pipeline with bending. Finally, strain gages are highly sensible to the condition of the adhesive layer used to attach the strain gage to the surface of the pipe .

In general, some of the current limitations in the available techniques for monitoring stress are: low depth level, relative stress measurement, high sensitivity to other variables and restricted use in field due to the nature of the required equipment. Thus, a suitable alternative is the use of low-frequency ultrasonic guided waves or simple named guided waves.

Ultrasonic testing is one of the most widely used methods for Non-Destructive Evaluation (NDE) and SHM. Traditional ultrasonic testing, based on bulk waves, is performed locally on specimens by examining the information contained by the wave traveling across large structural components, where high sensitivity to small discontinuities in the material and quite time consuming are presented.

Otherwise, guided wave inspection is a recent growing technique, which is non-invasive and economically affordable capable of examining long lengths of pipes from a single location [95]. Generally, guided waves are launched at one spot location using a circumferential actuator around the pipe and they are partially reflected when they encounter discontinuities (such as welds, branches, drains, corrosion patches and any material discontinuity).

The interaction of guided waves with material discontinuities in pipes is a complicated physical phenomenon, which has not been totally described for all of the possible instances

encountered in industrial applications. One of them is the presence of stress in pipelines or cylindrical specimens which is a more complex phenomenon due to is not a material discontinuity, is a volumetric alteration of the propagation path lacking reflections and mode conversion.

Although, the guided waves present a different response to stress compared with the rest of the material alterations, it is expected variations of the guided wave field in presence of it, which can be mainly tracked under two approaches. The first one is based on the Acoustoelastic Effect (AE) that involves the evaluation of guided wave velocity change, and the second one relies on observing particular features in the waveform attributed to the propagation in a medium under stress, which can be detected by statistics tools.

Some recent works in fault detection or detection of abnormal conditions by implementing statistical tools can be found in [30, 12, 104, 42, 103, 82]; they involve experimentally validated statistical algorithms on different structures such as pipelines, laminate plates, aircraft sections and composite materials. Some of them were performed in CODALAB, host research group, with a considerable background and research works in statistical-based monitoring schemes.

On the other hand, some challenges still persist in the understanding of the guided waves applied to condition monitoring, in [95] some specific challenges are identified :

1. Modeling accuracy is critically dependent on accurate input parameters. These parameters often are difficult to obtain – (especially for anisotropic and viscoelastic properties, interface conditions, and defect characteristics)

2. Signal interpretations are often difficult (since multi-mode propagation and mode conversion with special test structure geometric features)

3. Sensor robustness to environmental situations like: temperature, humidity, stress, mechanical vibrations, shock, and radiation

4. Adhesive bonding challenges for mounting sensors and sustainability in an SHM environment

5. Merger of guided wave developments with energy harvesting and wireless technology

This thesis aims on contributing to challenges 2,3,4; focused on the case of guided waves propagating in a medium subjected to mechanical stress, where specific results will be detailed throughout this document.

In summary, this thesis is focused on developing stress monitoring schemes in cylindrical structures by employing guided waves, statistical data-driven models, signal-based detection and wave features, in order to improve the overall condition identification performance.

1.2 Objectives

The main objective of this thesis is to propose a monitoring scheme based on guided waves for the detection of different stress levels in cylindrical structures. This aim is achieved tracking wave propagation features in the sensing signal attributed to the guided wave field variations and changes in the transducer operation due to the presence of mechanical stress in the structure (waveguide). In this study, longitudinal and flexural modes are generated by piezoelectrics transducers, while torsional modes are generated by means of magnetostrictive actuators. Mechanical stresses in the specimen under investigation are detected by means of a statistical tool (Principal Component Analysis) and signal processing (Residuals) both of them in the time domain. Due to the acoustoelasticity effect, that governs the dynamic of stressed guided waves, an important part of this thesis is devoted to analyze the influence of this effect in the proposed monitoring scheme and mainly in the dispersion curves.

1.2.1 Main Objective

To propose a robust methodology founded on statistical and signal-based schemes for monitoring mechanical stress in cylindrical structures using the piezo-actuation and magnetostriction principles. The proposed monitoring schemes are numerically and analytically studied and experimentally validated in pipes and rods under recreated environmental and process conditions.

1.2.2 Specific Objectives

- To implement the suitable setup to launch longitudinal, flexural and torsional waves by piezoelectrics and magnetostriction transducers.
- To propose statistical features for monitoring stress level in cylindrical structures based on changes of the guided wave field.
- To evaluate the effect of different coupling layers in the guided wave propagation along a pipeline in terms of the transmitted energy and mode conversion.
- To propose a data-driven based stress monitoring approach for cylindrical waveguides, robust to varying room temperatures using non axisymmetric guided waves modes in a PCA framework.
- To validate the proposed methodology in a dedicated pipe and rod test rig, where stress scenarios are created and tested.

- To study the acoustoelasticity effect in the propagation of stressed guided waves since an analytical, numerical and an experimental perspective.
- To propose a computational scheme for determining the dispersion curves of stressed waveguides.

1.3 Outline of the contribution

This thesis is devoted to present a new approach for monitoring stress variations in cylindrical structures. To achieve this goal, a series of statistical and signal processing techniques are presented to detect and classify different stress levels in structures based on features associated with the guided wave propagation. The new indices to stress detection or stress estimation are based on different statistical and signal approaches such as Principal Component Analysis (PCA), Root means square (RMS), time delay and peak position. The indices are validated and tested on different cylindrical structures such as steel pipe tubes and rods. Additionally, it is studied the sensitivity to the room temperature of the implemented indices for stress monitoring and when this effect may mask the presence of stress, it is attenuated using an appropriate temperature compensation method.

Next, an approach to calculate the dispersion curves in a waveguide in presence of stress, based on Effective Elastic Constants (EEC), is presented and compared with previous works. The dispersion curves are generated using a Semi-Analytical Finite Element (SAFE) frame in order to simplify the determination of dispersion curves. Otherwise, torsional waves obtained by the magnetostriction principle are used to study numerically, analytically and experimentally the effect of the stress in the wave propagation and some concluding remarks are made. Finally, a new scheme for pipeline support stiffness monitoring based on the energy leakage and mode conversion of the fundamental torsional mode is proposed and experimentally validated.

Chapter 2

Theoretical research overview

2.1 SHM principles and concepts

In general, SHM refers to the use in situ of non-destructive sensing and analysis of system response features –in time, frequency or modal domains – with the purpose of detecting changes, which may indicate damage, abnormal condition or degradation. The diagnosis is achieved by configuring, in a proper way, three major components: Sensor system, data processing system and health evaluation system.

The monitoring system inputs correspond to acquired signals from sensors (acceleration, strain, and displacements) which may catch the dynamical response of the system. In this sense, many types of sensors have been used such as accelerometers, optical fiber, electromagnetic systems, PZT devices, among others. The PZT and magnetostrictive technology has shown promising results since their low cost, reliability, wide frequency response range and good electromechanical coupling features. Once physical measurements are acquired, the data processing system provides specific features with enough information to predict the current structural condition.

On the other hand, the structural health evaluation system must incorporate models with the capability of discriminating between healthy and abnormal states. In the literature three detection schemes are reported: signal-based, model-based and non-traditional-based [100]. Signal-based methods use signal features associated with the system response for a specific state. Variations with respect to a reference signal may be interpreted as an abnormal condition. Model-based methods propose to correlate experimental scenarios measurements with analytical or numerical models in order to identify the current structural state. Finally, the non-traditional methods apply pattern recognition algorithms such as genetic algorithms, neural networks, combined with digital signal processing techniques such as wavelet analysis, Wigner-Ville transforms among others in order to detect abnormal structural conditions.

On the other hand, it is common to classify condition-based algorithms in performance levels, which refers to the degree of the diagnosis goal [29]. These levels are: level 1 (Detection), level 2 (Location), level 3 (Quantification) and level 4 (Prognosis). In this research, the stress detection and its location are equivalent because stresses are a volumetric phenomenon. Thus, the proposed monitoring schemes belong to a combination of level 1 and level 2 because the stress detection is the result of features obtained when the guided wave propagation is in a stressed waveguide to which implies a location process. In addition, after an appropriate setting, an estimation or quantification of the likely stress can be obtained

2.2 Statistical Models

The utilization of statistical models belongs to non-traditional detection schemes, which recently has gained the researchers' attention thanks to the progress in capturing, saving and data processing. Statistical models of the monitored structure is often used, even when the physical process being modeled is or not deterministic or with high analytical complexity.

Statistical models are based on pattern recognition technique, whose goal is the classification of objects into a number of categories or classes. The pattern recognition method classifies data (patterns), in this case wavefields, based on either a priori knowledge or on the statistical information extracted from the patterns. The patterns to be classified are usually the groups of measurements, defining points in an appropriate multidimensional space. The measurements used for the classification are known as features and can be organized in vector or matrices.

The features vector generation is determined by the system under monitoring, and the features selection is critical for the success of the classification system. There are two types of pattern recognition: supervised and unsupervised. For supervised pattern recognition, training data for each class are available for the classifier design, while for unsupervised they are not available. For the unsupervised pattern recognition problem, the goal is to cluster "similar" feature vectors by unraveling their underlying similarities [17]. In this thesis a monitoring scheme based on an supervised pattern recognition problem is considered for guided wave fields affected by stressed conditions.

According to Konishi and Kitagawa [62], there are three usages for a statistical model:

- Predictions
- Extraction of information
- Description of stochastic structures

In this work, a statistical model PCA-based is obtained to represent the nominal structural condition in the monitored cylindrical structure. This is acquired based on the extraction of statistically significant information from the propagation of low frequency ultrasound signals along the structure. Once the model is obtained, different structural conditions can be tracked by comparing the current state with the obtained from the statistical model. Although the statistical methods are relatively straightforward to implement, their main drawback is that they do not provide any well-defined description of the associated damage mechanism or any change in the mechanical parameters of the structure under investigation.

The statistical indices PCA-Based (T^2 and Q), used in this work as stress features, are typically the so-called non-parametric statistical condition indices. These are not related with the absolute structural parameters since they measure the deviation from the baseline signature or condition. Therefore, it is assumed that the greater the abnormal condition, the greater the resulting condition index.

On the other hand, in many situations, incipient damage and high order damage may lead to statistical indices values of the same order of magnitude than the caused by external disturbance such as temperature or changes in the bonding layer. Consequently, the particular "threshold value" demanding an alarm could vary between structures. Therefore, it is needed robust statistical indices to avoid positive falses [101].

2.3 Guided Waves and Bulk Waves

The ultrasonic waves are part of the Non Destructive Techniques (NDT) and it involves the use of bulk waves and guided waves. Ultrasonic bulk wave propagation refers to waves that encounter no boundaries, like waves traveling in infinite media, as shown in Figure 2.1a. Thus, bulk waves propagate by shearing and longitudinal stresses in the bulk of the material and correspond to a type of non dispersive waves, where their velocity is constant with the frequency. On the other hand, guided waves are a special type of ultrasonic waves working at the low part of the ultrasonic frequency range. They propagate either at the boundaries (Surface waves) or between the boundaries of the waveguide, see Figure 2.1b. A waveguide is the physical structure over which mechanical waves are confined in their propagation.

Guided waves and bulk waves are measured using traducers in two possible configurations: pulse-echo when the emitter is used also to receive the ultrasonic signal and pitch-catch when the receiver and the emitter are two different units. Ultrasonic waves, bulk and guided waves are affected by discontinuities in the propagation medium, changes in the acoustic impedance and internal variations of the medium, which produces changes in the wave´s

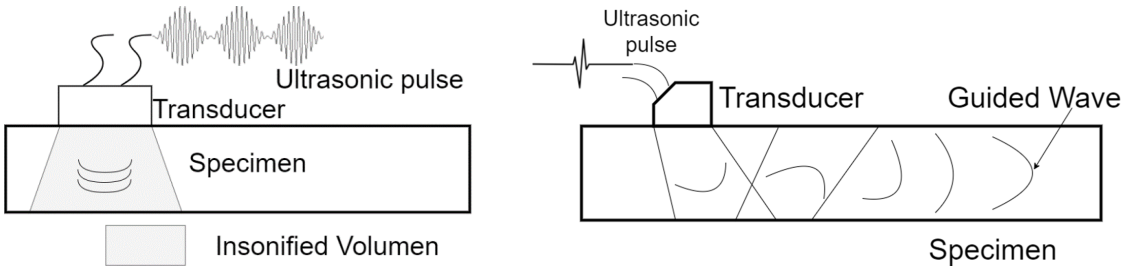

a) Traditional bulk waves with normal beam b) Guided waves generated by an angle beam wedge

Fig. 2.1 Comparison between bulk wave and guided wave

pattern expressed by mode changes, velocity changes, attenuation, etc. These variations can be considered as symptoms associated with changes in the waveguide.

Although bulk wave techniques are spread out and used extensively, the guided waves have some advantages such as [95]:

- Inspection over long distances since the suitable guided wave presents low attenuation and can propagate even in the kilometers range.
- Although the actuator is located in a single probe position, the guided waves provide an image of the entire cross-section area of the waveguide under investigation.
- The suitable guided wave can provide greater sensitivity to discontinuities than standard localized normal beam ultrasonic inspection.
- The ultrasonic guided wave analysis techniques allow inspection of hidden, submarine, coated, subterranean and encapsulated structures.
- Guided wave propagation and inspection are cost-effective because the inspection is simple and rapid. The inspection can be performed without removing of insulation or coating along of a pipe or device, except where the transducer is located.

Bulk and guided waves behave differently but they are actually governed by the same wave equations. The difference in the mathematical solution of the two types of waves is due to the boundary conditions. For the bulk waves, the solution does not depends on the boundaries because they travel without any border interaction. On the other hand, guided waves propagate as a result of the interaction between the bulk waves and the boundaries of the waveguide producing reflection, refraction and mode conversion.

There are two fundamental characteristics of guided waves propagation. The first one is the presence of different propagating modes for a certain frequency. The type and quantity of propagation modes are determined by the shape and size of the waveguide cross section, the material properties and the boundary conditions of the waveguide. The second is the existence of dispersion, which is the nonlinear relationship between wavenumber and frequency. As a consequence, signals with a significant bandwidth are distorted, because their spectral components propagate at different phase speeds, as they travel along the waveguide. Thus, the composition of guided waves varies with distance and time or with wave velocity and frequency. The dispersion is expressed in wave velocity dispersion curves such as the phase velocity versus frequency and the group velocity versus frequency.

Based on the geometry and material properties of the medium, the analytical model used to determine the dispersion curves provides the resonance´s modes that satisfy the boundary conditions of the wave propagation. Each resonant mode determines how the guided waves propagate. As a result the guided waves are dependent of the wavelength and frequency, the propagation is only possible for certain combinations of frequency and wavenumber.

There are a number of methods to obtain the dispersion curves for guided waves. The methods can be roughly classified in the following approaches: numerical, experimental, analytical and a combination of numerical and analytical. Numerical methods are based on Finite Elements (FE) analysis in time domain. Experimental approach uses time-frequency representations techniques such as Two-Dimensional Fourier Transforms (2DFFT), for the case of the phase velocity dispersion curve and Short Time FFT (STFFT) and Wavelet Transform for the case of group velocity dispersion curve. The analytical approach are supported by the wave equations. Finally, Semi-Analytical Finite Elements (SAFE) gather numerical and analytical approaches. All of them are computational expensive and time consuming.

An analytical study of the guided waves propagation is very complex and it results in an estimation of the actual behavior of the wave in terms of velocity of propagation, activated modes, profile of propagation, attenuation, etc. For the case of hollow cylindrical waveguide dispersion curves, they are usually generated under a non-stress, isotropic considerations, which are farther of the real monitoring conditions.

The presence of external mechanical stresses in a material causes modification of its structural morphology and its mechanical and acoustic behavior. Then, the propagation of guided waves are modified in terms of velocity and attenuation. Under stress, these two quantities depend on the direction and polarization of the waves as well as on the direction of the applied stress [14]

2.4 Dispersion in guided waves

The dispersion phenomenon in the propagation of waves is due to frequency-dependent velocity variations. Experimentally and analytically, under some conditions, it can be observed a difference between the velocity of a group of waves (Group velocity) and the velocity of the individual waves (Phase velocity). The group velocity, V_{gr}, is the velocity at which a guided wave packet travels at a given frequency while the phase velocity, V_p, is the velocity at which the individual peaks within that packet travel. Phase and group velocities are related to each other through the following equation:

$$V_{gr} = V_p + \xi \frac{dV_p}{d\xi}, \tag{2.1}$$

where ξ is the wavenumber ($\xi = \omega/V$) or relationship between angular frequency, ω, and the propagation velocity V. The physical effect of dispersion is the space distortion in time of the excited modes by a signal of finite duration as they propagate from the source. Even though pulse shape changes can be observed, the basic premise of wave propagation in lossless media in a waveguide is that the energy is conserved [95].

The relation between frequency and velocities of phase and group is determined by the dispersion curves. In other words, these curves are a plot of the wavenumber-frequency relations.The dispersion curves are the solutions (roots) of an eigenvalue equation that represents the stress-free condition in the boundaries of the waveguide. The roots which satisfy this condition are a couple of pair of (ω, ξ) values that can be re-expressed as a coordinate in the $V_p - f$ or $V_{gr} - f$ dispersion curves.

Now, when an ultrasonic pulse is launched in a specimen, a spectral content (bandwidth) is carried by the excitation pulse. This range of frequencies may involve several phase or group velocities. As a example of the dispersion effect, in Figure 2.2, it can be seen, a V_p-f curve, where only one propagation mode and the excitation pulse bandwidth are represented . As shown, the bandwidth frequency content produce different phase velocities. Thus, inside of the excitation pulse, several phase velocities develop a deformed wavepacket as the guided wave is propagating as shown in Figure 2.3.

Figure 2.3 shows, in time domain, the effect of the dispersion in a 3 cycle toneburst with a centre frequency of 150 kHz monitored after $(0.3m, 0.5m, 0.7m$ and $1m)$ of propagation in plate of Alum-6061 of 2 mm of thickness)

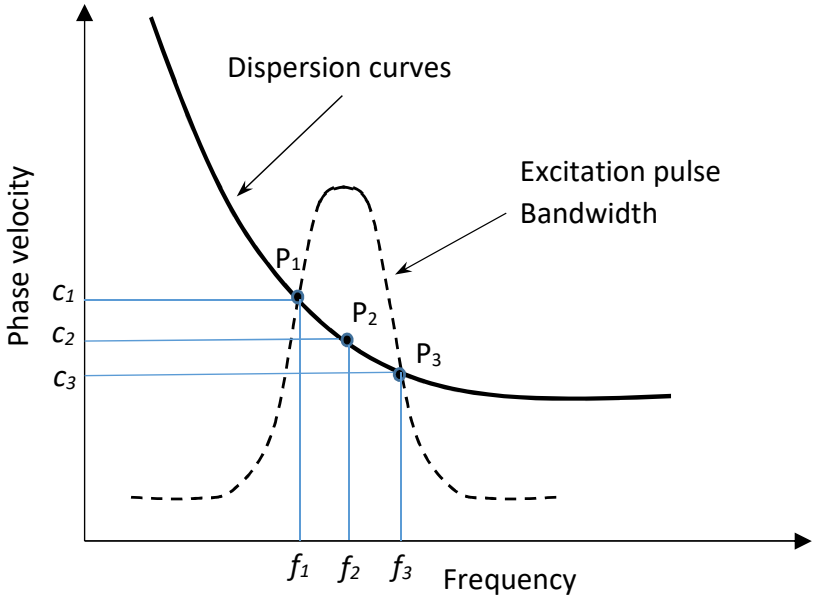

Fig. 2.2 Graphical representation of dispersion curve and excitation bandwidth

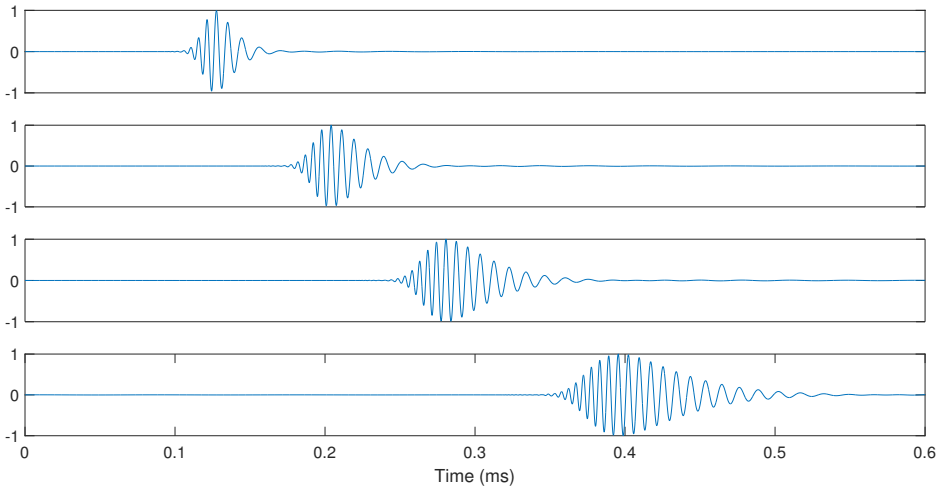

Fig. 2.3 Dispersive wave sequence for propagation distances 0.3 m through 1 m

2.5 Guided waves in a hollow cylinder

The use of ultrasonic guided waves in the exploration of cylindrical specimens such as pipes and tubing is receiving much attention recently. GWs provides the possibility of examining a large volume of material from a single position in specimens with complex configurations such as underground, coated, or under insulation, concrete, etc.

Guided waves in cylindrical waveguides may propagate in circumferential or axial directions. The guided wave field can be described by solving the governing wave equations based on the boundary conditions, dimensions and material properties of the specimen under investigation.

The study of guided waves in hollow cylinders started back in the nineteenth century. Pochammer in 1876 and Chree in 1889 first investigated the propagation of the guided waves in a free bar. A more extend and complete study of harmonic waves in a hollow circular of finite extent is performed in the mid of the twenty century by [39].

The simplest model of the guided waves in cylindrical waveguides is derived restricting the wave propagation to a homogeneous and isotropic medium. Based on Newton´s second law and the conservation of the mass for a volume in an elastic solid it is possible to derive the Euler´s equation of motion as follows,

$$\rho\left(\frac{\partial^2 u}{\partial t^2}\right) = \nabla \cdot \sigma, \tag{2.2}$$

where $u = u_{(r,\theta,z)}$ is the displacement field in cylindrical coordinates, ρ is the material density and σ is the stress tensor; which can be expressed in terms of the strain tensor ε using the Howke´s Law, as:

$$\sigma = C\varepsilon, \tag{2.3}$$

where C is the stiffness tensor. For an isotropic, homogeneous, linearly elastic material, the theory of elasticity demonstrates that it is possible to reduce the 21 components of the C tensor to two constants (λ, μ) which are the Lamé constants [6]. The density ρ and Lame constants λ and μ determine the bulk wave velocities in the material. If the strain tensor is expressed in terms of displacement, Hookes law simplifies to the following equation:

$$\sigma = \lambda I \nabla \cdot u + \mu\left(\nabla u + u\nabla^T\right). \tag{2.4}$$

Combining Equation (2.3) and Equation (2.4) yields Naviers´s linear differential equation of motion for isotropic elastic medium (Wave equation)

$$\mu\nabla^2 u + (\lambda+\mu)\nabla\nabla\cdot u = \rho\left(\frac{\partial^2 u}{\partial t^2}\right). \tag{2.5}$$

Because the cylinder considered here is isotropic, Helmholtz decomposition can be utilized to simplify the problem: The displacement field u can be split into the rotational component $\nabla\times H$ and an irrotational component $\nabla\Phi$ in this way:

$$u = \nabla\Phi + \nabla\times H, \tag{2.6}$$

where Φ is a scalar potential and H is an equivoluminal vector potential. In general $\nabla H = g(r,t)$ where g is a function of the coordinate vector, $r=(r,\theta,z)$ and the time t [109]. The function g can be chosen arbitrarily due to the gauge invariance of the field transformations. This means that the potentials are not unique, but it can always select them so $\nabla H = 0$. Making the equivoluminal vector potential a zero-divergence vector implies that the field is solenoidal (i.e. there are no sources or sinks of energy within the region) and provides the necessary additional condition to uniquely determine the three components of u (u_r,u_θ,u_z) from the four components,(Φ,H_r,H_θ,H_z), of the two Helmholtz potentials (Φ,H) [39]. By using Helmholtz potentials, the Navier's equation of motion, Equation (2.5) yields:

$$\nabla\left[(\lambda+2\mu)\nabla^2\Phi - \rho\left(\frac{\partial^2\Phi}{\partial t^2}\right)\right] + \nabla\times\left[\mu\nabla^2 H - \rho\left(\frac{\partial^2 H}{\partial t^2}\right)\right] = 0. \tag{2.7}$$

A sufficient condition for this equation to holds is that both terms vanish, which leads to the standard scalar and vector decoupled wave equations:

$$C_L\nabla^2\Phi = \frac{\partial^2\Phi}{\partial t^2}, \tag{2.8}$$

$$C_T\nabla^2 H = \frac{\partial^2 H}{\partial t^2}, \tag{2.9}$$

where C_L and C_T are the velocity of the longitudinal and shear waves respectively, which can be expressed in terms of Lame´s constants (λ,μ) as follows:

$$C_L = \sqrt{\frac{\lambda+2\mu}{\rho}} \tag{2.10}$$

$$C_T = \sqrt{\frac{\mu}{\rho}} \tag{2.11}$$

The potentials H and Φ have the following formats in cylindrical coordinates:

$$\nabla^2\Phi = \frac{\partial^2\Phi}{\partial r^2} + \frac{1}{r}\frac{\partial\Phi}{\partial r^2} + \frac{1}{r^2}\frac{\partial^2\Phi}{\partial\theta^2} + \frac{\partial^2\Phi}{\partial z^2} \tag{2.12}$$

$$\vec{H} = H_r\overrightarrow{e_r} + H_\theta\overrightarrow{e_\theta} + H_z\overrightarrow{e_z} \tag{2.13}$$

$$\nabla^2\vec{H} = \left(\nabla^2 H_z - \frac{1}{r^2}H_r - 2\frac{1}{r^2}\frac{\partial H_\theta}{\partial\theta}\right)\overrightarrow{e_r} + \left(\nabla^2 H_\theta - \frac{1}{r^2}H_\theta - 2\frac{1}{r^2}\frac{\partial H_r}{\partial\theta}\right)\overrightarrow{e_\theta} + \nabla^2 H_z\overrightarrow{e_z} \tag{2.14}$$

Assuming a harmonically oscillating source, the solutions for the Equation (2.7) is:

$$\Phi, H = \Gamma_1(r)\,\Gamma_2(\theta)\,\Gamma_3(z)\,e^{-i(\xi r-\omega t)}, \tag{2.15}$$

where ξ is the wavenumber (vector), and $\Gamma_1(r)$, $\Gamma_1(\theta)$ and $\Gamma_1(z)$ describe the field variation in each spatial coordinate. Assuming that the wave does not propagate in the radial direction (r) and that the displacement field varies harmonically in the axial (z) and circumferential (θ) directions, Equation (2.15) can be written as:

$$\Phi, H = \Gamma_1(r)\,e^{-i(m\theta+\xi r-\omega t)}, \tag{2.16}$$

where m is the circumferential order or angular wavenumber. If $m = 0$ the mode is axisymmetric, i.e. without dependence on the θ-direction. The axisymmetric modes are divided into torsional n modes $T(0,n)$, which only involve the θ component, and longitudinal n modes $L(0,n)$, with both radial and axial components. $L(m,n)$ are named flexural modes and they require the three coordinates to describe its field.

Using Equation (2.16) in Equation (2.7); it is possible to derive a system of Bessel differential equations to describe the displacement field. The canonical solution of this set of differential equations are Bessel functions (B_n) which their argument determine the order of the function.

The Bessel functions order basically describes the evolution of the function as its argument is increasing. Now, the order of the Bessel functions are determined by the relation between the bulk wave wavenumber k and the corresponding propagating guided wave wavenumber ξ. Bessel's ordinary functions $J_n(x)$ and $Y_n(x)$ are employed for real arguments, and the modified Bessel functions $I_n(x)$ and $K_n(x)$ for purely imaginary arguments.

The displacement field u which is function of (B_n, r, k, ξ, m) is the base to formulate the uncoupled stress fields (σ_{rr}, $\sigma_{r\theta}$, σ_{rz}) via strain tensor, the resulting stress expressions depend on $(\delta B_n, r, \xi, k, m)$. Now, the set of stress equations is expressed as a linear weighted

Bessel's equations. In general, the set of stress equations can be simplified written in a matrix shape as follows:

$$[\sigma_i] = [C]\,[A_i]\,, \tag{2.17}$$

where σ_i is comprised by $(\sigma_{rr},\ \sigma_{r\theta},\ \sigma_{rz})$, C is a function of $(\delta B_n, k, m, \omega, \xi)$ and A_i is a weighted vector.

In the case of an isotropic single layer pipeline. The boundary conditions specify that the traction part of the stress tensor is null in both surfaces of the tube ($\sigma_{rr} = \sigma_{r\theta} = \sigma_{rz} = 0$) and two gauge invariance condition equations at $r = r_{int}$ and $r = r_{ext}$, which leads to the following matrix eigenvalue equation, as follows:

$$\begin{bmatrix} C_{11} & C_{12} & \cdots & C_{18} \\ C_{21} & C_{22} & \cdots & C_{28} \\ \vdots & \vdots & \ddots & \vdots \\ C_{81} & C_{81} & \cdots & C_{88} \end{bmatrix} \begin{bmatrix} A \\ B \\ \vdots \\ B_3 \end{bmatrix} = \begin{bmatrix} 0 \\ 0 \\ \vdots \\ 0 \end{bmatrix} \tag{2.18}$$

Equation (2.18) is named the frequency or characteristic equation of the waveguide, and its roots (ω, ξ), eigenvalues, determine the propagated modes. Among all of the eigenvalues, there are real eigenvalues for propagating guided wave modes and complex eigenvalues including pure imaginary eigenvalues for the evanescent modes. The eigenvalues lead to dispersion curves and the eigenvectors to the wave profile in the waveguide cross-section.

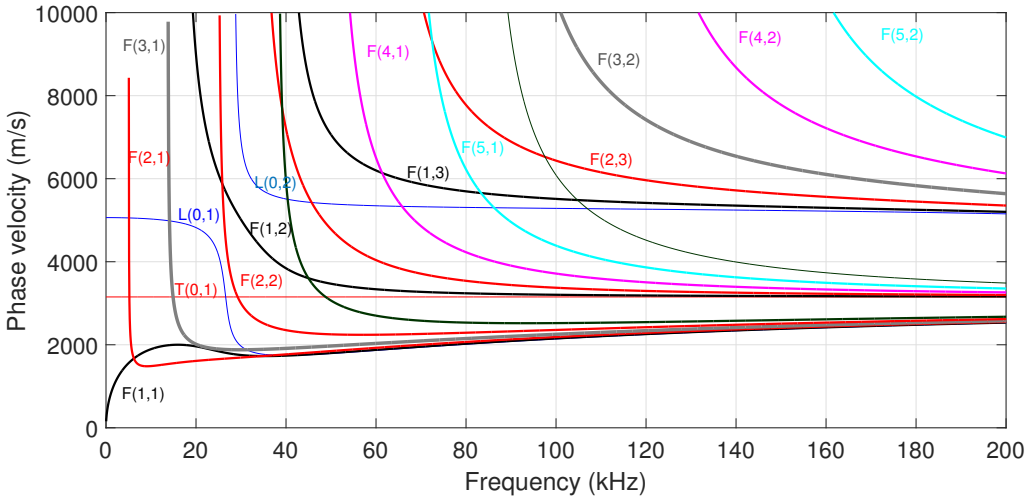

Fig. 2.4 Sample dispersion curves of one-inch schedule 40 steel pipe including all of the longitudinal and torsional modes, including axisymmetric modes $L(0,n)$,$T(0,n)(n = 1,2,3,\ldots)$ and non-axisymmetric modes $L(m,n)(m = 1,2,3,\ldots,n = 1,2,3,\ldots)$

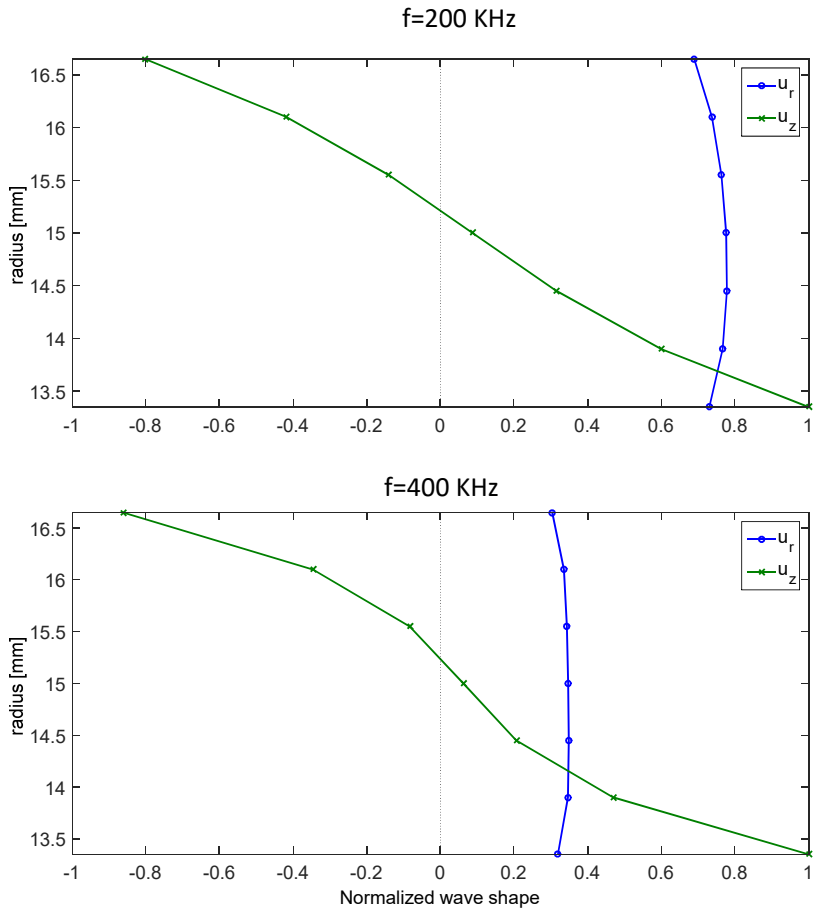

Fig. 2.5 Sample wave structures of the L(0,1) at the frequency = 200 kHz and 400 kHz in a one-inch schedule 40 steel pipe

Figure 2.4 illustrates an example of phase velocity dispersion curves for a cylindrical specimen. In this figure, it can be noted the presence of longitudinal, flexural and torsional modes. As is presented in the Figure 2.4, for any excitation frequency exists a possible set of modes that can be activated and produce a multimode propagation. Thus, a single mode activation is a challenge in cylindrical specimens.

The real parts of the eigenvectors lead to displacement distributions for every eigenvalue. The energy distributions in the $r-direction$ are wave profiles and the energy distributions in the $\theta-direction$ are called angular profiles, as showed in Figure 2.5 and Figure 2.6.

Neither the cylindrical waveguides properties nor the group number or mode n affects the angular profiles of a single mode. Figure 2.5 shows that the same mode n at different frequency have similar wave profile. Figure 2.6 illustrates the angular profiles of the wave modes with 2^{th}-4^{th} circumferential orders. However, the real propagating angular profiles of a wave group highly depend on the properties of the hollow cylinder and the excitation conditions.

In Figure 2.6 it can be concluded that while the angular profile of 2^{nd} circumferential order provides high ultrasonic energy concentrations around of 0º,90º, 180º and 270º, the remainder areas are blind to the ultrasonic investigation, e.g. in the range between 120º and 150º. Therefore a complete scan of the cross-section of a cylindrical specimen requires the launching of several guided waves with different circumferential orders.

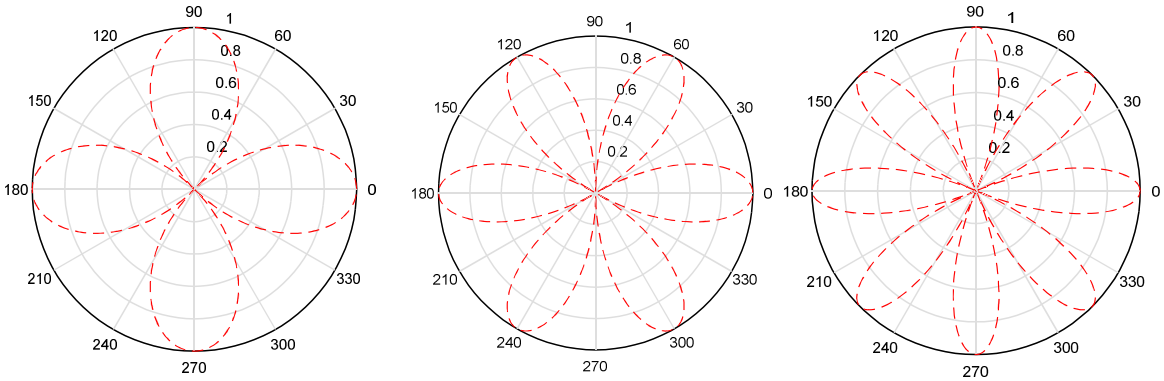

Fig. 2.6 Angular profiles of the (a) 2^{nd} (known as axisymmetric modes), (b) 3^{rd}, and (c) 4^{th} modes in a mode group n (n=1,2,3, . . .).

2.6 Acoustoelasticity Effect

2.6.1 Acoustoelasticity in bulk waves

The first efforts to explain the propagation of stressed waves were back in 1937 with the Murnaghan work [84]. He published "Finite Deformations of an Elastic Solid". In this work, Murnaghan presented a model of the linear elastic theory, including finite deformation in elastic isotropic materials, describing the variation of the bulk velocities whilst the waveguide is subjected to an initial static stress field. The Acoustoelastic Effect is a non-linear effect of the constitutive relation between mechanical stress and finite strain in a material of continuous mass which yields bulk velocities dependent of the stress state of the material. This new model includes the Third-Order Elastic Constants (TOEC) or the acoustoelastic constants. Hughes and Kelly [57] determined that in addition to the Lamé constants (λ and μ), three additional constants, in the case of Murnaghan constants, l,m,n are required to describe the wave propagation in isotropic materials subject to uniaxial stress. Once the values of l,m,n of a particular material specimen are determined, any experimental measure of one of the bulk velocities reveals the stress at which the specimen is subjected to.

TOEC highly depend on the material internal structure i.e. by the material processing. Therefore, degree, depth, and location of any possible residual stresses produced by the processing influence the acoustoelastic properties. Three major difficulties are impeding the advancement of the use of the acoustoelasticity for stress monitoring by using bulk waves [102]. First, the Acoustoelastic Effect is small, typically about of 0.001% per MPa of applied stress, for metals. These small variations impose high precision in experimentation. Second, the inherent or induced preferred orientation of crystalline grains (anisotropy) affects acoustoelasticity. The third major problem is the unknown influence of localized plastic deformation or residual stresses.

TOEC are determined experimentally by measuring acoustic phase velocities and then analytically solving a system composed by a set of equations. Each equation describes a particular bulk velocity in a predefined direction and polarization as a stress function. Hughes and Kelly [57] experimentally determined the TOEC of polystyrene, iron, and Pyrex glass. For isotropic media subject to uni-axial stress in direction 1, σ_{11} (2 and 3 are the other two perpendicular directions), the velocities of elastic waves are derived using the following equations [68]:

$$\rho c_{11}^2 = \lambda + 2\mu + \frac{\sigma_{11}}{3K}\left[2l + \lambda + \frac{\lambda+\mu}{\mu}(4m + 4\lambda + 10\mu)\right] \tag{2.19}$$

$$\rho c_{12}^2 = \rho_0 c_{13}^2 = \mu + \frac{\sigma_{11}}{3K}\left[m + \frac{\lambda n}{4\mu} + 4\lambda + 4\mu\right] \tag{2.20}$$

$$\rho c_{22}^2 = \lambda + 2\mu + \frac{\sigma_{11}}{3K}\left[2l - \frac{2\lambda}{\mu}(m + \lambda + 2\mu)\right] \tag{2.21}$$

$$\rho c_{21}^2 = \mu + \frac{\sigma_{11}}{3K}\left[m + \frac{\lambda n}{4\mu} + \lambda + 2\mu\right] \tag{2.22}$$

$$\rho c_{23}^2 = \mu + \frac{\sigma_{11}}{3K}\left[m - \frac{\lambda + \mu}{2\mu}n - 2\lambda\right], \tag{2.23}$$

where ρ is the mass density, c_{ij} is the velocity of the wave propagating in direction i (x, y, z) and polarized in direction j, σ_{11} is the normal stress in direction 1, (λ, μ) are the Lamé´s coefficients, (m, n, l) are the Murnaghan´s coefficients and $K = \lambda + \frac{2\mu}{3}$ is the compressibility modulus in terms of Lamé´s coefficients [59]. For the case of a homogeneous and isotropic infinite solid subjected to a uniaxial stress (σ), the bulk velocities of longitudinal C_L and shear waves C_T, propagating in the same direction as the applied stress, can be written in the first-order approximation of Equations (2.24) and (2.25), respectively, as [13]:

$$C_L^\sigma = \sqrt{\frac{\lambda + 2\mu}{\rho}}\left\{1 + \frac{\sigma}{2(\lambda + 2\mu)(2\lambda + 2\mu)}\left(\frac{\lambda + \mu}{\mu}(4\lambda + 10\mu + 4m) + \lambda + 2l\right)\right\} \tag{2.24}$$

$$C_T^\sigma = \sqrt{\frac{\lambda}{\rho}\left\{1 + \frac{\sigma}{2\mu(3\lambda + 2\mu)}\left(4\lambda + 4\mu + m + \frac{\lambda n}{4\mu}\right)\right\}} \tag{2.25}$$

Expressions inside curlic brackets represent the effect of the stress on the bulk velocity (acuostoelastic effect). Now, if $\sigma = 0$ in Equations (2.19....2.23 or 2.24 and 2.25), the resulting equations are the stress-free equations for C_L and C_T respectively, Equations (2.10 and 2.11). Therefore, the term which contains σ in the RHS in Equations (2.19..2.23 or 2.24 and 2.25) constitute the variation of the bulk velocity due to the stress. So, the previous equations can be expressed as a general linear equation as:

$$c_{ij}^\sigma = c_{ij}^0\left(1 + A_{ij}\sigma_{11}\right), \tag{2.26}$$

Where c_{ij}^σ is the velocity of wave propagating in direction i and polarized in direction j in a medium under uni-axial stress σ_{11}, c_{ij}^0 is the wave velocity in the stress free medium or bulk velocity and A_{ij} are the acoustoelastic constants term which depend on Lamé´s

coefficients and Murnaghan´s coefficients. The initial velocities c_{ij}^0 obtained using, Equations (2.10 and 2.11).

As can be noted, in Equations (2.10 and 2.11) the bulk velocities in the stress-free case depend on material density ρ and the Lame´s constants which are function of the material elastic constants: Young's Modulus (E) and Poisson ratio (ν) as follows:

$$\rho C_L^2 = \kappa_L = \lambda + 2\mu = \frac{E(1-\nu)}{(1+\nu)(1-2\nu)}, \tag{2.27}$$

$$\rho C_T^2 = \kappa_T = \mu = \frac{E}{2(1+\nu)}, \tag{2.28}$$

The subscripts L and T in Equations (2.27 and 2.28) represent longitudinal and transversal or shear waves, respectively. As presented by [102], Equations (2.10 and 2.11) can be used to explore the effect in the velocity of elasticity or density when they are no longer treating as constants (non linearity effect) by expanding for small finite perturbations at a fixed static stress, producing the following equation:

$$\frac{\Delta c}{c} = \frac{1}{2}\left[\frac{\Delta \kappa_{L,T}}{\kappa_{L,T}} - \frac{\Delta \rho}{\rho}\right], \tag{2.29}$$

where

$$\frac{\Delta \kappa_{L,T}}{\kappa_{L,T}} = \left[\frac{\Delta E}{E}\right]_{\nu=cte} \tag{2.30}$$

and,

$$\frac{\Delta \rho}{\rho} = \left[\frac{\Delta V}{V}\right]_{M=cte} = \left(\frac{\varepsilon_y}{\nu} - 2\varepsilon_y\right) \tag{2.31}$$

where ΔV is the volumen variation, ε_y is the strain in $y-direction$ and ν is the Poisson´s ratio. Equation (2.29) represents the normalized propagation velocity changes in a bulk wave when Young´s modulus and material density are no longer considered constants. In the case of uniaxial stress in $x-direction$ (the selection of x is arbitrary) within the elastic range, a change in density is expected by the stress-strain behavior. So, as it can be inferred, a change in density produce a slight different value of acoustic bulk velocity (*density effect*). The density effect is represented by the second term in the RHS in Equation (2.29) while the first term estimates the effect of the Young´s modulus change by the stress, *elasticity effect*.

In summary, variations in the ultrasonic bulk velocities, C_L and C_T in presence of stress depends on the stress effect over the Young's modulus, the Poisson ratio and the strain perpendicular to the applied stress (*density effect*). Now, the influence of environmental

conditions such as temperature in the Young's' modulus also suggests variations in the bulk velocities. The sum of these effects produce also variations in the generated guided waves due to bulk waves are the foundation of them.

In [102] a static stress of 350 MPa was applied to a plate of 7075-T651 Aluminum, for waves with particle motion normal to the tensile stress, it was found that the *density effect* accounts around 25% of the velocity increase. Therefore, the major effect to the change of the bulk velocities can be attributed to the variation of the elastic term, first term in the RHS in Equation (2.29). The *density effect* and the *elasticity effect* have little influence for waves with particle motion parallel to the applied stress.

2.6.2 Acoustoelasticity in guided waves

Although the Acoustoelasticity effect only predicts the change of ultrasonic bulk velocities, C_L and C_T, as shown in Equations (2.24) and (2.25). These velocities are used to compute the guided wave phase and group velocities. Therefore, it can be inferred the stress influence in the guided waves.

Some recent works have shown how mechanical stress in the waveguide influences the wave field of the GWs. Thus, a new subject of research has been gaining the attention, the study of the stressed guided waves. Under this condition, the velocity is no longer only frequency dependent but also stress dependent. Some recent works have been studying the velocity variations of GWs when they propagate in specimens subjects to stress, such as [14, 13], where the longitudinal mode $L(0,1)$ is used to track the variations of the phase velocity in a rod subject to stress. In [19], a finite element technique for modeling the dispersion characteristics of guided waves in a waveguide of arbitrary cross section subjected to axial load is presented. Here, it is analytically demonstrated that the change in velocity is proportional to the strain and decreases as the frequency increases. The dispersion curves for a plate are determined in [35] by assuming that the specimen under uniaxial stress becomes unstressed anisotropic and the fourth order tensor is used in the resulting wave equation.

Few works in the literature are reported using the acoustoelasticity of the guided waves for stress monitoring [36, 97, 85, 83, 13]. Most of them have used a linear analytical expression of acoustoelasticity, it which the variation of the guided wave velocity is expressed as a linear function of the applied stress, defining the parameters via experimentation. This approach, although is practical, is highly time consuming, demand much experimentation and its main drawback is the specificity of the model obtained, that is, is only strictly valid for the studied specimen at the test conditions.

As mentioned early, the relation between phase and group velocities and frequency are typically depicted in the dispersion curves. Such curves are computed for unstressed

samples based on the eigenvalues obtained of the stress equations assuming zero stress at the boundaries. The presence of stress in the propagation path yields variation in the velocity of the guided waves as it was demonstrated in some works [18, 71, 70, 69, 35]. So, it can be concluded that it must exists a specific dispersion curve for each applied stress.

2.7 Review of Ultrasonic Stress Monitoring Techniques

Guided waves have been used as a tool for stress estimation based on the velocity change of the propagated pulse. Most of the works reported in literature are focused on measuring the Time Of Flight (TOF) or phase shift to determine phase and group velocities and comparing them with a knowledge base. Di Scalea and Rizzo [23] present a method based on guided waves for stress monitoring in seven-wire steel strands. In this research, a substantial increase in stress measurement sensitivity is accomplished by adding the effect of strand elongation. Chaki et al., in [14, 13] report the use of the relative phase velocity change of the longitudinal mode $L(0,1)$ for estimating the stress levels in a prestressed steel strands by means of an analytic model and an acoustoelastic calibration curve. The analytical model depends on the material properties, waveguide diameter and probing frequency. In [110], the stress in bolted connections is investigated by comparing several methods based on the acoustoelasticity effect (TOF, velocity ratio and mechanical resonance frequency shift). They found small velocity changes in presence of stress variation, which demands a high sampling rate and consequently an increased cost. In [97] the homogeneous biaxial stresses are assessed for an aluminum plate by measuring phase velocity changes on multiple propagation directions using a single mode at a specific frequency. Experimental results indicate that phase velocity changes can be closely approximated by a sinusoidal function with respect to propagation angle, where every sinusoidal coefficient can be estimated with a single uniaxial loading experiment. However, this approach is not practical since a great experimental effort is required to define the sinusoidal function and it is highly sensitive to the material microstructure. Finally, in [71], the SAFE method is used to analyze the influence of axial load on the wave propagation in a rail. Although it is possible to measure the phase shift caused by axial load changes, the sensitivity to changes in elastic modulus due to temperature changes is of a larger magnitude. They concluded the necessity of compensating or eliminating external effects, mainly propagation changes due to temperature variations, in order to achieve a robust estimation of the stress.

2.8 Finite element method for analyzing guided waves

The finite element method (FEM) is a widely used numerical approach for solving dynamics problems such as wave propagation and vibration. FEM avoids the analytical solution of complex differential or integral equations providing accurate and computationally efficient solutions. To achieve a correct FEM simulation, a very well understanding of the physical problem is required, i.e. limitations, constrains, assumptions, etc. So, once a solution is found, a verification stage must be conducted to check correct selection of the model and the solution process. FEM may be combined with analytical analysis or other numerical methods to achieve optimum solutions such as SAFE method (Semi-analytical Finite Element Method) discuss in a chapter ahead.

The information required to solve a field problem such as the guided wave propagation are specimen geometry, materials and its properties, external loads (excitation) and boundaries conditions. FEM approach is based on the division of the entire waveguide into small and discrete elements with simple loading and boundary conditions reducing the whole problem to a simple element problem. After that, an information coupling scheme is used to propagate the element solutions until covering the total specimen.

A FEM simulation requires the following stages [95]:

1. Physical phenomena analysis
2. Mathematical Modeling: determining mathematical models, geometries, governing equations, and appropriate FEM solving approaches (Explicit and implicit)
3. Discretization: dividing the studied geometry into a mesh of finite elements
4. Preliminary analysis: having some analytical results, experience, or experimental results for comparison.
5. Finite element analysis:
   (a) Preprocessing: inputting data of geometry, material properties, boundary conditions, etc.
   (b) Numerical calculation: deciding interpolation functions, obtaining a matrix to describe the behavior of each element, assembling these matrices into a global matrix equation, and solving this equation to determine the results.
   (c) Postprocessing: listing or graphically displaying the solutions.
6. Validation of results: verification of the simulation contrasting the FEM solution with preliminary analysis or experimental results.

In the case at hand, the simulation of the propagation of GWs, FEM represents a numerical calculation approach based on the principle of virtual work as follows:

$$\int \delta\varepsilon^T \sigma dv = \delta u^T \mathbf{P}\mathrm{dV} + \delta \mathrm{u}^{\mathrm{T}} \Phi \mathrm{dV}, \tag{2.32}$$

where,

ε = strain tensor;

σ = stress tensor;

u=displacement vector;

δu= first variation of displacement u

V= Total volume of the body

P= Body force in V

S= Total surface of the body

Φ= Surface traction vector on S.

Once the waveguide is discretized by a mesh of finite elements, all of the loading functions are applied to the nodes of each element instead of on the surface or in the volume. In guided wave propagation, the external load represents the source of excitation. Therefore, an interpolation function is needed to determine values of all of the variables inside the elements. The interpolation function is named shape function.

Wave propagation is a dynamic problem. The governing equation of FEM for an undamped dynamic problem is:

$$\mathbf{M}\ddot{u} + \mathbf{K}u = \mathbf{F}, \tag{2.33}$$

which can be considered as generalized Newton's second law. Here **M** is the mass matrix, **K** is the stiffness matrix, **F** is the equivalent element force load vector, $\ddot{u}$ is the acceleration vector and u is the displacement vector.

For the case of a harmonic solution with circular frequency ω and without external force the governing equation, Equation (2.33), can be simplified as:

$$(\mathbf{K} - \omega^2 \mathbf{M}) = 0, \tag{2.34}$$

where both **M** and **K** are positive definite. In this thesis, the FE method has been used mainly for wave propagation simulation using a time marching explicit scheme. In the time marching scheme, the solution process takes place over a small time step Δt. The solution of the dynamic equations will give displacement, velocity and acceleration histories. The solution process is repeated for N time steps until the total time $T = N\Delta t$ is reached. The

solution time is directly proportional to the number of degrees of freedom in the model, which is usually very high for wave propagation problems [45].

Explicit schemes solve the Equation (2.34) only at the beginning of the increment Δt . In this scheme the mass matrix is diagonalized, thus the accelerations at time zero are calculated quite simply by using the net mass and force acting on each element [22]. This scheme does not require any large matrix inversion. The accelerations are integrated twice to obtain the displacement after a time step Δt. To produce accurate results, the time increments must be quite small so that the accelerations are nearly constant during the increments [22].This technique minimizes memory usage and generally reduces the overall processing time [90].

In order to adequately model a wave propagation, it is necessary the appropriate spatial and temporal discretization of the finite element model in order to guarantee the convergence to the correct solution.

2.8.1 Spatial discretization

In order to assure guided wave dynamics capture, an appropriate element length, l_e is required. In [79] is recommend 20 nodes per wavelength (λ). Thus, this recommendation can be expressed as:

$$l_e = \frac{\lambda_{\min}}{20}, \tag{2.35}$$

where λ_{min} is the shortest wavelength of interest, because the proportionality between velocity and wavelength ($\lambda = V/f$), the C_T, which is the lowest velocity, provides λ_{min}. So, the final criterion can be expressed as [32]:

$$l_e = \frac{C_T}{20f} \tag{2.36}$$

2.8.2 Time resolution

The integration time step, Δt, is the step size for which Equation (2.34) is solved (time resolution). An adequate integration time step, Δt, is very important for the accuracy of the solution. In general, the accuracy of the model can be increased with increasingly smaller integration time steps. With long time steps, the high-frequency components may not be resolved accurately enough. On the other hand, too small time steps imply high computational cost. Therefore, a compromise in the Δt selection must be found. A common criterion is using at least 20 points per cycle of the highest frequency results[99].This rule is expressed as:

$$\Delta t = \frac{1}{20 f_{max}} \tag{2.37}$$

2.8.3 General procedure for FEM simulation of guided waves

In this section a brief step by step procedure is presented to model guided waves in isotropic hollow cylinders using a commercial FEM package.

1. To create a part (type: deformable with its respective sections)
2. To define isotropic elastic material properties: mass density, Young's modulus, Poisson's ratio
3. To define and assign section properties
4. To assemble the model
5. To create node sets (Actuator,Sensor)
6. To configure the analysis
    - Create the step with type of procedure: $Dynamic - Explicit$
    - Introduce the time period (usually in μs)
    - Define the incrementation (Time step) according to Section (2.8.2)
7. To setup the output database (Field Output Request): displacement, velocity, stress fields for set "Sensor"
8. To product the guided wave excitation do the following:
    - Create a tabular amplitude (time versus amplitude) data for the modulated pulse at the excitation frequency
    - Create a mechanical load (Concentrated force or distributive) applied in the appropiate direction with the magnitude defined in the previous item.
    - It is also possible to generate guided waves using displacement of the boundary conditions instead of the load
9. To mesh the part or instance
    - Apply the element type to the part or instance according to the specimen dimensions (2D or 3D)

- Seed the mesh by size using the criterion mentioned in Section (2.8.1)

10. To create and submit the job

11. To check results setting the Visualization mode

Chapter 3

Guided waves generation

3.1 Introduction

This chapter deals with some of the suitable transducers for the guided waves generation in cylindrical waveguides. There are several different methods for exciting ultrasonic waves, including piezoelectricity, electrostriction, magnetostriction, electromagnetic (EMAT), laser generation, etc. Among them, the piezoelectric effect is by far the most widely used [16]. Thus, at first, the chapter is devoted to give a general overview of the PZT subject and introduce the important parameters when piezoelectric materials are used to generate ultrasonic transducers. Next, the influence of the adhesive layer (couplant) in the transmission of the ultrasonic energy from/to the PZT is investigated experimentally and in the Section 3.2.2 it is formulated an analytical simplified PZT model to determine the relationship between the quasi-static mechanical strain in the PZT (external stress) and the generated electric signal when the transducer acts as a sensor.

PZT transducers are used in the early stages of this research for their convenient low cost, easy excitation, and low weight. Besides, as it will be demonstrated ahead in this chapter, for their capability to generate a rich signal in wavepackets, which will be helpful for providing data as inputs to statistical tools. As it was proven with the Normal Mode Expansion Method, the single excitation of a PZT attached to the pipe yields the activation of several longitudinal and flexural modes, generating a characteristic signal, appropriate to track slight wave field changes in the PCA-based monitoring scheme.

On the other hand, while longitudinal modes are commonly used in pipelines monitoring, torsional modes are preferred because they offer less wave attenuation than other family modes due to leakage energy is small. When the waveguide is in mechanical contact with fluids, part of the ultrasonic energy may be transmitted to the fluid via normal and shear stresses. For this reason, next in this research, the torsional guided waves are explored in the

search of a robust stress monitoring scheme adequate for industrial applications. Nowadays, several setup are available to generate torsional guided waves, however the ones based on the magnetostriction offer advantages for its low cost, no couplant layer required , and easy implementation. For these reasons, a magnetostrictive transducer is implemented in last part of this research.

3.2 Piezoelectrics

Piezoelectrics (PZTs) are very common transducers for SHM applications. They can be roughly divided in two categories: embedded or surface-bonded, as shown in Figure 3.1. In general, PZTs are inexpensive, light and available in very fine thicknesses (microns order) making them an option for integration into structures when the weight and space are issues. In addition, for its low cost is an attractive alternative for SHM applications such as permanent pipelines monitoring in-situ.

Fig. 3.1 Surface bounded PZT

PZTs operate on the piezoelectric and inverse piezoelectric principles that couple the electrical and mechanical behavior of the material. An electric charge is yielded on the surface of the piezoelectric material when it is strained. The contrary effect also occurs, i.e. mechanical strain in the PZT in response to an applied electric field (polarization). Therefore, they can be utilized as both actuators and sensors. The most commonly available materials are lead zirconium titanate ceramics (known as PZT) and polyvinylidene fluoride (PVDF), which is a polymer film [94]. Piezoelectric ceramics transform mechanical energy into electrical energy and vice-versa in a number of modes as shown in Figure 3.2.

- thickness and length

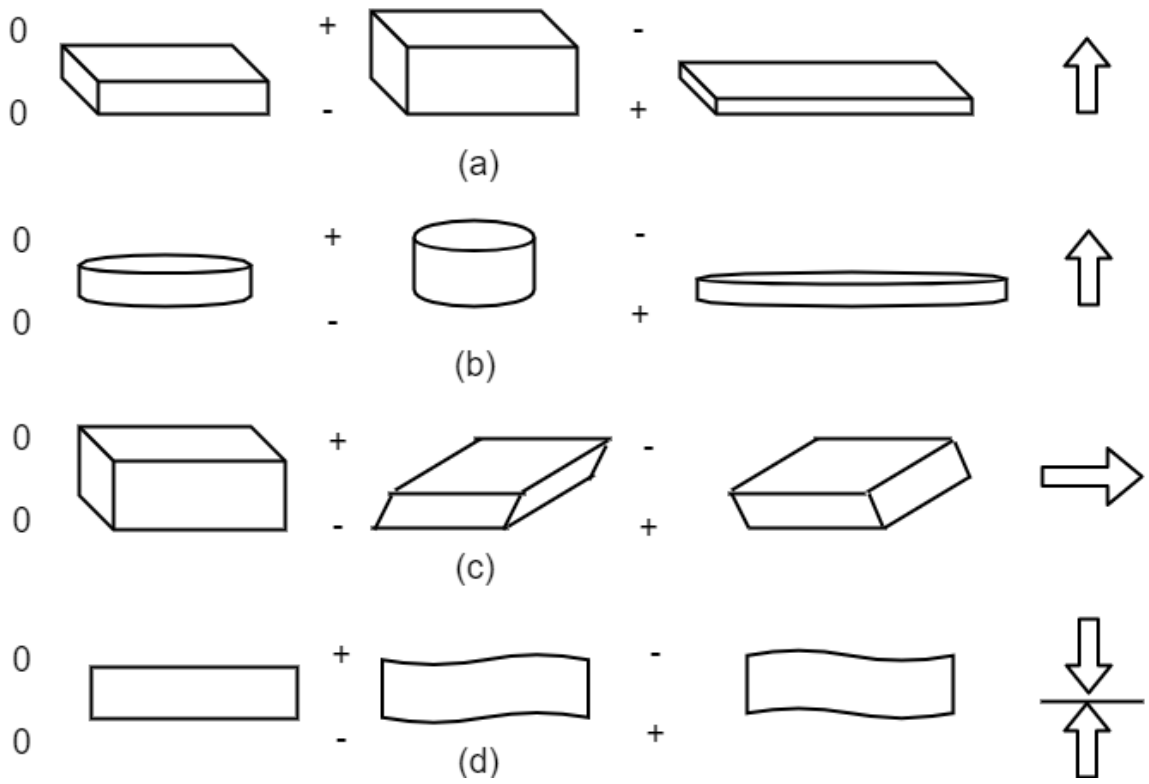

Fig. 3.2 Basic piezoelectric transduction in (A) thickness and length, (B) radial, (C) thickness shear, and (D) bending modes. The arrows represent the direction of polarization and the (+) and (-) are the applied field

- radial
- thickness shear
- bending modes

Configurations are normally selected to produce the desired actuation or sensing vibrational mode. Typically, the controlling dimension is chosen to a specific resonance frequency of interest. Other dimensions are chosen to minimize other vibrational modes near the frequency of interest, to a specific aperture size, or to accommodate the desired actuation or sensing area. In the case of thin disc PZTs (usually the diameter is at least 10 times thickness) exist two modes of vibration: radial and thickness modes, both poled through thickness, as presented in Figure 3.3. The vibration mode is controlled mainly by the relation between diameter and thickness and the excitation frequency.

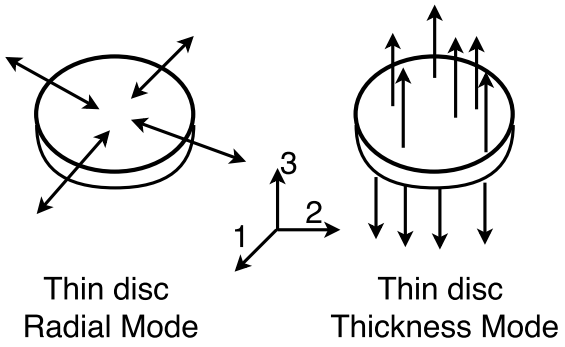

Fig. 3.3 Modes of vibration of PZT poled through 3-direction

PZTs can operate in pitch-catch, pulse-echo or could be positioned into the structure as sensor networks or arrays, which would be permanently wired and interrogated at will. Spatially distributed arrays of piezoelectric can be used to generate or receive specific wave fields (modes). Arrays of sensors can be excited with a slight phase difference producing an ultrasonic beam formed through the constructive interference of the wave fields generated by the actuators. The beam angle could be adjusted by changing the relative phase of the elementary signals [44].

3.2.1 Influence of the coupling layer on guided wave propagation

To transmit ultrasonic energy, the transducers should be attached to the structure under exploration with a substance named couplant. The couplant layer has aimed to avoid air cavities and improve the acoustic impedance, enabling an efficient ultrasonic transmission.

The propagated wavefield strongly depends on some properties of the coupling layer i.e. viscosity, Young modulus, adhesive curing time and thickness. Variations in the coupling layer yields different wave patterns due to variations in the propagation modes and the transmitted energy.

In [91], it is stated the effect of adhesive thickness and its modulus on the performance of adhesively bonded piezoelectric elements. Experimental results showed the dependence of the electromechanical impedance and the resonant frequency with the thickness as well as the amplitude of the sensor signal. In the case of the adhesive modulus a more sensitive affectation of the impedance and amplitude is found at high frequency. Besides, results found by [27] showed a better repeatability of the wave pattern for a less viscosity of the couplant in spite of a lesser transmitted energy. The repeatability is evaluated using the average standard deviation of a set of signals for each studied couplant. On the other hand, [20] compared several couplants in a concrete arrangement used in a monitoring scheme. They proposed the plasticine as alternative due to its feasibility to remove it from the material. Although, superglue (cyanocrylate) always provided the best quality signals, when the practical factors were considered, plasticine was found to be the better performing couplant material overall.

In this thesis, several couplants (hair gel, glycerin, honey, vaseline, and cyanoacrylate) typically used in ultrasonic tests [91, 27, 20], are evaluated in a pipe test bench to study transferred ultrasonic energy and their frequency content. Thus, In order to prepare the specimen for testing some previous tasks have to be performed at the surface where the PZT will be installed:

- The surface should be sanding with sandpaper number 400 and 200 to avoid discontinuities due to rough surfaces and impurities in the specimen.
- the specimen should be degreasing by using acetone

For the case of the cyanoacrylate, the PZT is attached to the pipe just by putting a constant pressure on the exterior surface of the PZT during the cyanoacrylate curing process. Meanwhile, the rest of the couplants are attached to the pipe with a constant external force during the process of emitting and capturing the signals. In our case, it was used a permanent magnet to exert pressure on the top face of the PZT

The complete system (PZTs, couplants and cylindrical waveguide) frequency response was carried out using a sinusoidal signal sweeping in the range of frequency between 20 KHz and 200 kHz to determine the bandwidth. A picoscope 2208A is used as function generator to supply an electric pulse signal to the piezoelectric to produce the guided wave. The frequency response for each studied couplant is shown in Figure 3.4. In this figure is showed that cyanocrylate presents the greater amplitude with a PZT resonant frequency

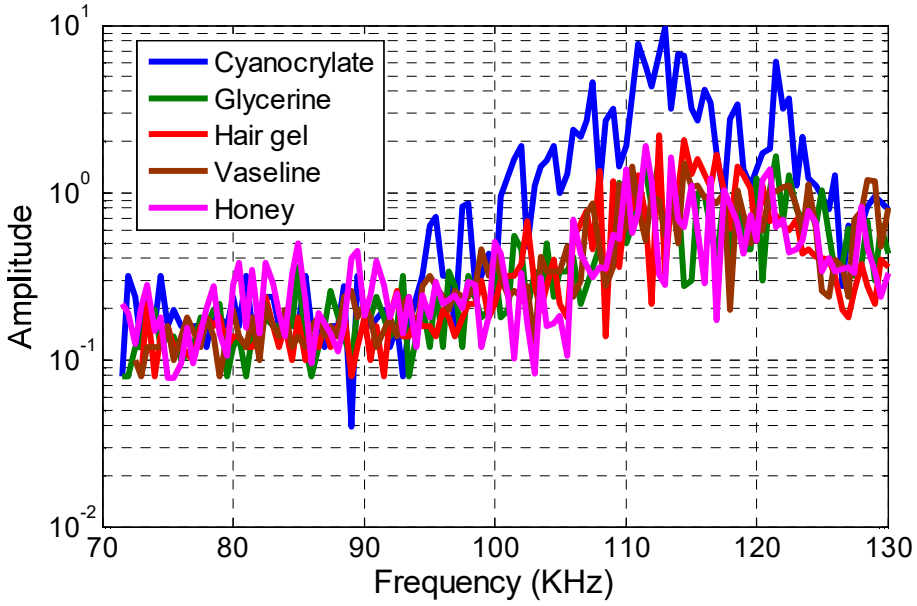

Fig. 3.4 Frequency response for the studied couplants

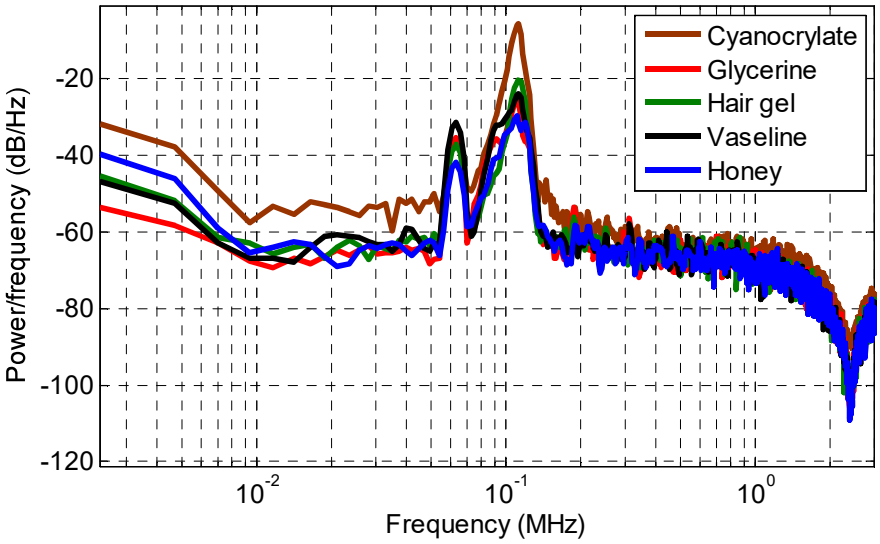

Fig. 3.5 Power Spectral density of the captured signals for the tested couplants

around of 113 KHz. The transmitted signal by the emitter is a modulated Hann window sine of 5 peaks as shown in Eq. 3.1. In addition, the power spectral density (PSD) of the couplants are presented in Figure 3.5

$$A = \frac{1}{2}\sin 2\pi ft\left[1-\cos\left(\frac{2\pi ft}{5}\right)\right], \tag{3.1}$$

where, f is the frequency of the wave carrier. A comparison of the captured signals in samples domain for every couplant is shown in Figure 3.6. The captured signals has been amplified 70 times and filtered out before the acquisition by the picoscope.

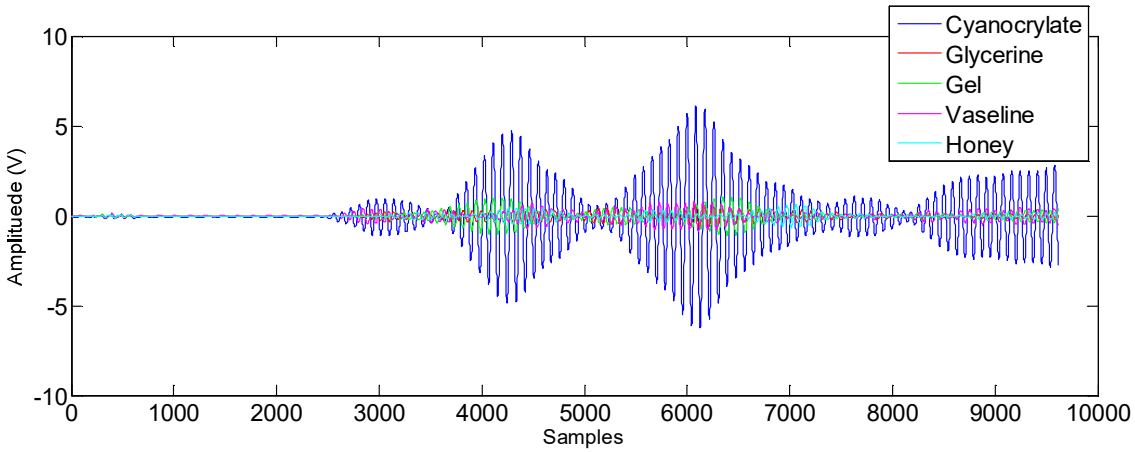

Fig. 3.6 Guided wave propagation using different couplants in the same waveguide

Figure 3.6 compares the guided waves amplitude generated by PZTs by using a different couplant layer with the same thickness. Based on the experimental results it can be concluded that among the studied couplant materials, cyanoacrylate offers high transmissibility compared with others for the studied test conditions.

3.2.2 The PZT effect in the captured guided wave under stress

This section presents an analytical study on the effect of the applied external stress to the pipe, and consequently to the attached PZT, in the sensor electric signal. Because piezoelectric materials can work as dynamic strain sensors, the effect of the stress in such transducers must be considered. The constitutive relations for piezoelectric materials, under small field conditions are [16] :

$$\mathbf{S} = \mathbf{s}^{\mathbf{E}}\mathbf{T} + \mathbf{d}^{T}\mathbf{E}, \tag{3.2}$$

and

$$\mathbf{D} = \mathbf{d}^{\mathbf{E}}\mathbf{T} + \varepsilon^{\mathbf{T}}\mathbf{E}, \tag{3.3}$$

where $\mathbf{S}$ is the strain, $\mathbf{s}^{\mathbf{E}}$ is the fourth order elastic compliance tensor at electric field constant or $\left(\frac{\partial S}{\partial T}\right)_E$, $\mathbf{T}$ is the stress, $\mathbf{d}^T$ is the piezoelectric strain coefficients for direct effect, $\left(\frac{\partial S}{\partial E}\right)_T$, $\mathbf{d}^{\mathbf{E}}$ is the piezoelectric strain coefficients for converse effect, $\left(\frac{\partial D}{\partial T}\right)_E$, $\mathbf{E}$ the applied external electric field, $\mathbf{D}$ the electric displacement or charge density and $\varepsilon^{\mathbf{T}}$ the dielectric permittivity under constant stress.

3.2.3 Numerical subscript notation

Since now, the following subscription notation is utilized. Three orthogonal axes are represented by subscript values 1 – 3. By convention, axis 3 is the direction of polarization of the PZT. A reduced subscript notation is used in which subscripts 4 – 6 indicate stress or strain in shear form about axes 1 – 3, respectively. This is illustrated in Figure 3.7.

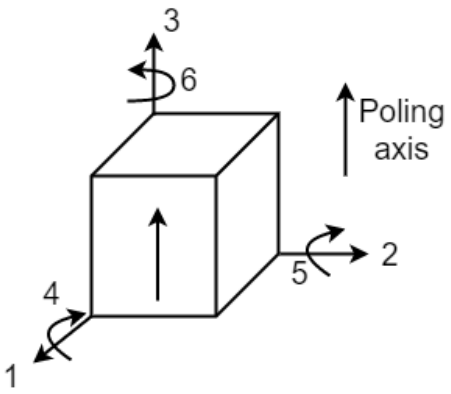

Fig. 3.7 Axis notation for polarized piezoelectric ceramics

In reduced subscript notation, electromechanical quantities can have two numerical indices. The first indicates the electrical direction and the second indicates the mechanical direction.

3.2.4 A simplified PZT electro-mechanical model

In this thesis, it is utilized thin and light PZTs to produce longitudinal and flexural guided waves in pipes. In order to simplify PZT study and based on the symmetry, the analysis were performed in the plane 1-3 as shown in Figure 3.8. Radial mode is considered as actuation mode so the disc expands and contracts dynamically in the plane $1-2$, under a uniform alternating electric field E_3, which is applied in direction "3". The disc is bounded to the

pipe in a line aligned in direction 1, so no effect in direction “2” is considered. For sake of simplicity, vibration is adopted to be infinitesimally small with no damping. Additionally, the disc is assumed to has zero displacement in the midpoint. Under these assumptions and using the previously described subscripts, Equations (3.2 - 3.3) can be expressed as Equations (3.4 - 3.5) [101]

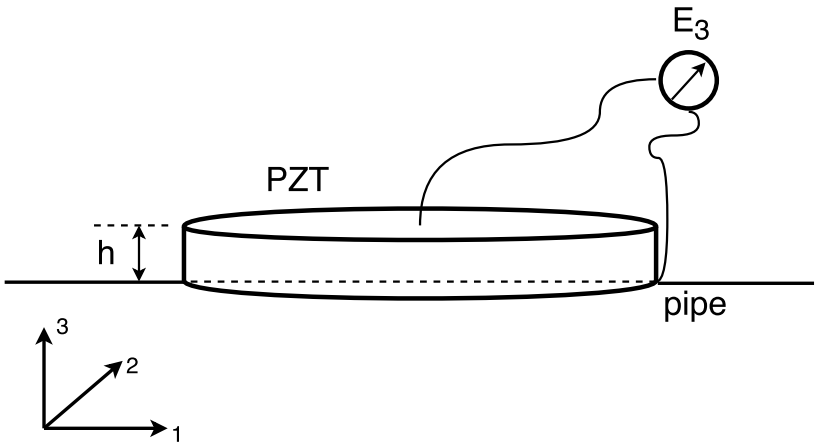

Fig. 3.8 Interaction model of PZT and the pipe

$$D_3 = \varepsilon_{33}^T E_3 + d_{31} T_1 \tag{3.4}$$

$$S_1 = d_{31} E_3 + \frac{T_1}{\bar{Y}_E}, \tag{3.5}$$

where S_1 is the strain in direction 1, d_{31} is the piezoelectric strain coefficient, T_1 the axial stress in direction 1 and Y_E is the Young´s modulus of elasticity at constant electric field, ε_{33}^T is the electric permittivity in “3” direction of the PZT under a constant stress. If the PZT is used as sensor $E_3 = 0$, then Equation (3.4) is reduced as follows:

$$D_3 = d_{31} T_1, \tag{3.6}$$

where T_1 can be substituted by $Y_E\ S_1$ using the Hooke´s Law. Now, using a capacitor parallel model, the charge density can be expressed as:

$$D_3 = \frac{\varepsilon_{33}^T V}{h}, \tag{3.7}$$

where V is the voltage across the PZT terminals and h is the PZT thickness. So, combining Equation (3.6) and Equation (3.7), the voltage of the PZT can be expressed in terms of the strain as:

$$V = \frac{S_1 d_{31} h Y_E}{\varepsilon_{33}^T}, \tag{3.8}$$

or:

$$V = S_1 k, \tag{3.9}$$

where

$$k = \frac{d_{31} h Y_E}{\varepsilon_{33}^T}. \tag{3.10}$$

Therefore, the voltage across the PZT terminals due to a dynamic strain varies linearly in a proportion of k, where k depends on geometric, electric and material factors. Hence, variations in the voltage signal in an isothermal condition are exclusively attributed to the strain.

Thus, in a stress monitoring scheme based on PZT in a pitch-catch configuration, the magnitude changes of the induced voltage across the PZT terminals are yielded by the sum of two strains: the finite deformation due to homogeneous stress in the elastic area $S_{1,static}$. and the dynamic perturbation superimposed on the stress state, wave propagation, $S_{2,dynamic}$. Both of them affect the amplitude of the sensed signal, see Equation (3.11). The different sources of guided wave energy variation mentioned above are difficult to isolate and quantify. The magnitude of the induced voltage V in the PZT terminals is modified if the static strain, $S_{1,static}$ is for compression or tension loads. For the case of tension in the material, the strain is positive and the voltage will be positive if d_{31} is positive, for the case of compression, the sign is opposite and for the induced small strain when the guided wave is propagating.

$$V = \left(S_{1,static} + S_{2,dynamic}\right) k \tag{3.11}$$

As a conclusion, the external loads in the waveguide will be transmitted to the PZT via mechanical coupling with the consequent strain generation in the PZT. This strain is added to the dynamic strain generated in the waveguide by the guided wave propagation influencing the generated voltage in the PZT sensor.

3.3 Magnetostrictive Transducers

3.3.1 Magnetostriction principle

Magnetostriction is a coupling phenomenon which yields the change in shape of materials under the influence of an external magnetic field, as a result of the small magnetic domains rotation. This re-orientation causes internal strains ($S = \Delta L/L$) in the material. The strains can produce elongation in the direction of the magnetic field, positive, or shortening in the opposite case. Magnetostriction is a reversible material feature. In the absence of the magnetic field, the material shape returns to its original dimensions. This effect is proportional to the magnitude of the magnetic field and after all the magnetic domains have become aligned with the magnetic field the saturation point is reached.

The size-changing effect is called the Joule effect, this effect is mainly used in magnetostrictive actuators. On the other hand, the Villari effect refers to the reverse phenomenon i.e. any change in dimensions of a ferromagnetic material induces a magnetic field. This effect is produced when a mechanical stress is imposed on a specimen yielding a change in the magnetic flux density which flows through the sample as a result of the creation of a magnetic field. The change in flux density can be detected by a pickup coil and is proportional to the level of the applied stress. The Villari effect is reversible and is used in sensor applications.

Finally, when a ferromagnetic material is subject to a perpendicular static magnetic field to a dynamic field, a shearing deformation is developed in the material; this phenomenon is called the Wiedemann effect. The developed shearing deformation created by the Wiedemann effect results in a torsional wave in the cylindrical waveguide.

Magnetostrictive transducers operate in accordance with the magnetostrictive principle. They have been used to produce and measure ultrasonic waves at frequencies ranging between roughly 20 kHz and 1–2 MHz for nondestructive testing (NDT) of waveguides such as pipes and plates [61]. In general, exists a number of transducers and experimental settings that use magnetostrictive phenomena to generate and measure elastic waves in waveguides. For the sake of brevity, it will only refers to transducers that use thin magnetostrictive patches or strips which are bonded with waveguides. In this case, the magnetostrictive effect mainly occurs in the patch. Elastic waves can, therefore, be excited and measured in both ferromagnetic and non-ferromagnetic waveguides if magnetostrictive patch transducers are employed, See Figure 3.9.

To derive a linearized magnetostrictive constitutive relations, the magnetic field vector **H**, the magnetic-flux-density vector **B**, the mechanical strain tensor **S**, and the stress tensor **T** have to be considered. Since a energy perspective and considering an adiabatic process the

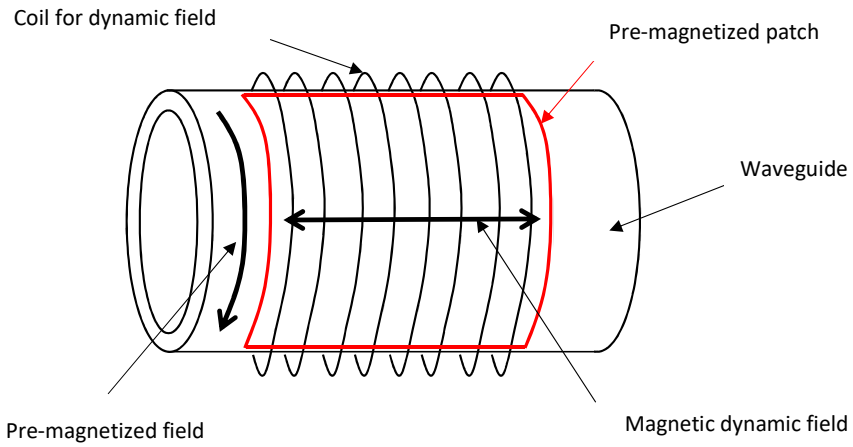

Fig. 3.9 Configuration of magnetostrictive patch transducer

infinitesimal tensor of the Gibbs free energy produces the following relation between strain and magnetic field and also between magnetic flux density and stress [61]:

$$\frac{\partial S_{ij}}{\partial H_k} = \frac{\partial B_k}{\partial T_{ij}} = \mathbf{d_{ijk}} \qquad (i,j,k = 1,2,3), \tag{3.12}$$

where **d** is called the piezomagnetic coefficient. When a material exhibits magnetostrictive behavior, Equation (3.12) states that there is always coupling between mechanical and magnetic fields. Therefore, **S** and **B** are functions of both **T** and **H**. Using Equation (3.12) and the definitions of compliance **s** (inverse of the elasticity tensor) and permeability μ, the magnetostrictive constitutive linear equations for small or infinitesimal changes in the field variables (**S,T,H,B**) can be expressed as:

$$d\mathbf{S} = \mathbf{s}d\mathbf{T} + \mathbf{d}^T d\mathbf{H}, \tag{3.13}$$

$$d\mathbf{B} = \mathbf{d}d\mathbf{T} + \mu d\mathbf{H}, \tag{3.14}$$

when the magnitude of the applied dynamic field is small compared with a static bias field, the following linearized constitutive relations Equation (3.15) and Equation (3.16), which result from Equation Equation (3.13) and Equation (3.14), can be used:

$$\mathbf{B}_D = \mathbf{d}\mathbf{T}_D + \mu \mathbf{H}_D, \tag{3.15}$$

where the subscribed quantities with D are related to the applied dynamic magnetic field. The villari effect is modeled by Equation (3.15), where $\mathbf{B}_D$ is the dynamic magnetic induction, **d** the magnetostrictive constant, $\mathbf{T}_D$ symbolizes the stress change, μ is the permeability at

constant mechanical stress σ and $\mathbf{H}_D$ is the dynamic magnetic field. Meanwhile the Joule effect can be represented by following equation

$$\mathbf{S}_D = \mathbf{s}\mathbf{T}_D + \mathbf{d}^T\mathbf{H}_D \tag{3.16}$$

where $\mathbf{S}_D$ is the dynamic mechanical strain, $\mathbf{s}$ the compliance coefficient at constant field strength $\mathbf{H}$, $\mathbf{T}_D$ is the stress change, $\mathbf{H}_D$ is the dynamic magnetic field and $\mathbf{d}^T$ is the magnetostrictive constant at constant stress. The magnetic field strength, H, could be calculated by using Equation

$$H = IN, \tag{3.17}$$

where I is the current and N is the number of coil turns. Due to the fact that the axis of a typical cylindrical waveguide is usually in line with the direction of magnetization, only the axial component needs to be considered. Therefore, d, μ and s can be treated as scalar quantities for simplification.

In the transducer application, magnetic energy is converted into mechanical energy. The efficiency of the energy converting process is governed by the magneto-mechanical coupling factor. The value of this factor usually varies between 0.5 and 0.7. In applications where only the longitudinal elongation is of interest (for standard actuator applications) the only material properties of interest are all relate to the longitudinal axis. This mode is called 33-mode and the magneto-mechanical coupling factor is called k_{33}. The magneto-mechanical coupling factor is given by equation [86]:

$$k_{33}^2 = \frac{d_{33}^2}{\mu_{33}^T} \cdot E^H. \tag{3.18}$$

In this equation, E^H is the Youngs modulus at constant value of magnetic field, the magnetostrictive coefficient d_{33} is the slope of the strain versus magnetic field in the characteristic curve $(S-H)$:

$$d_{33} = \frac{dS}{dH}. \tag{3.19}$$

Under quasi-static condition (continuous excitation under a sinusoidal alternating current), assuming zero pre-stress and assuming a linear relationship between the strain and the magnetic field, the strain is given by:

$$S_{33} = d_{33}H_3. \tag{3.20}$$

Equation (3.20) can be used to estimate the dynamic strain produced by an oscillating magnetic field H as it is required in the experimental stage of this work

3.3.2 Generation of torsional modes by Magnetostrictive principle

In this work, the fundamental torsional mode is generated and captured by using the magnetostriction principle. One advantage of this cost-effective method of transduction is the fact that coupland is no required between the specimen and the transducer [58]. On the other hand, magnetostriction principle provides a better performance to varying temperature environments compared to the piezoelectricity-based transducer, mainly for the absence of couplant. In the literature, it is reported that the temperature influence in the propagation of guided waves for a range (from 20 ºC to 200 ºC) generates a drop in amplitude (9 db) [107]. The basic configuration of the transducer is illustrated in Figure 3.10 and the real one used in the experimentation is depicted in Figure 3.11 . The set is comprised of two parts. The first one is a solenoid coil which provides a dynamic magnetic field to the pipe or measures the induced magnetic field through the propagation of the torsional guided wave in the waveguide. The second one, is a magnetostrictive strip which supplies a residual circumferential bias static field. The residual magnetization of the strip is obtained rubbing it with a magnet in the circumferential direction. Thus, the most critical component of a magnetostrictive system is the magnetostrictive material (ferromagnetic strip) used to transform electrical energy into mechanical and vice versa. Its transduction efficiency in both acquisition and transmission mode depends mainly on its physical properties. As a consequence, these physical parameters must be considered to select the right ferromagnetic material to be used in magnetostrictive transducers. For this reason, a magnetostrictive probe was acquired from *Guided Wave Analysis LLC* company. The MsS probe consists of amorphous cobalt–iron alloy strips (0.15 mm thick), which have lower eddy current loss and larger magnetostriction [58]. The solenoid coil was constructed of enameled wire of 0.32 mm of diameter (28 aws) copper wound around the strip with 50 turns along its width, a system with an Arbitrary Wave Generator (AWG) and amplifiers was used to excite the coil with the modulated pulse. In general, to create a torsional stress, a helical magnetization is induced in the ferromagnetic strip through the following procedure:

1. A bias magnetization (H_0), static magnetic field, in the strip is induced in circumferential direction through the passage of a permanent magnet as shown in Figure 3.12.

2. A second alternate magnetic field H_D of lower magnitude than H_0 is created in axial direction by the current flowing into a coil that surrounds the pipe circumference at the strip position as seen in Figure 3.13.

3. Finally, the combined magnetic fields generate an applied alternate helical field that according to the Villari effect will create torsional vibrations via shear stress.

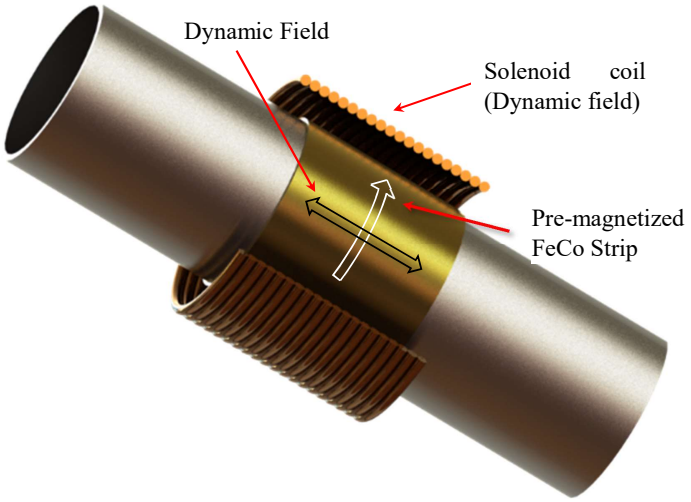

Fig. 3.10 Schematic representation of the magnetostrictive transducer

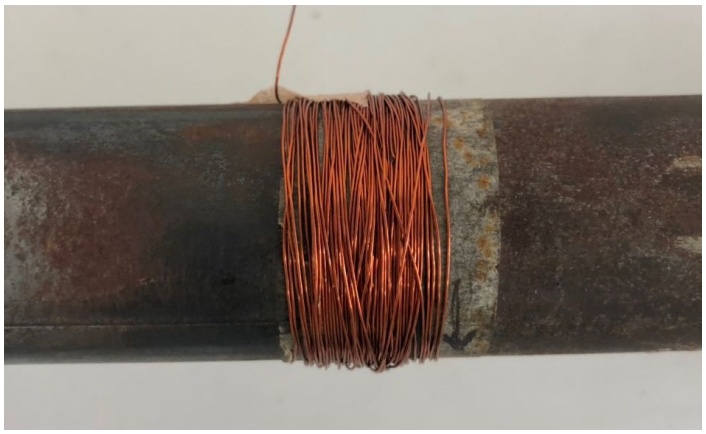

Fig. 3.11 Magnetostrictive transducer used in the experimentation

3.3.3 Single mode generation of T(0,1)

A key element of the inspection system is the selection and exploitation of a single mode. In general, an excitation source can excite all of the modes which exist within its frequency

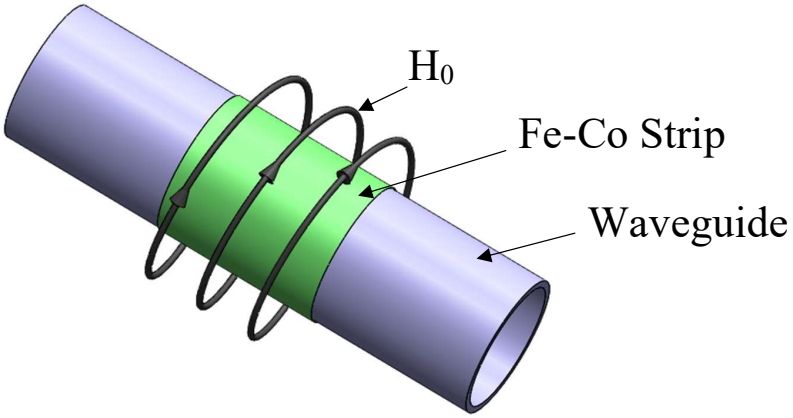

Fig. 3.12 Induced static magnetic field "H_0" in the FeCo strip

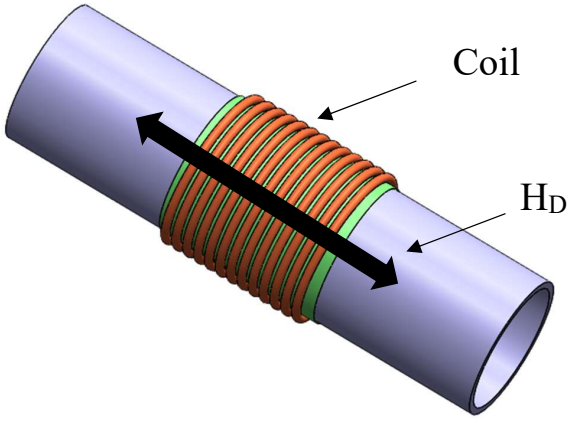

Fig. 3.13 Dynamic magnetic field "H_D" in the specimen

bandwidth. Therefore, although troublesome to achieve, it is essential to design the transducers and the signal to excite only the chosen mode. In some experiments covers by this thesis, the chosen mode for excitation in the inspection system is $T(0,1)$. This mode is very attractive because is non-dispersive over a wide bandwidth, so the signal shape and amplitude are retained as it travels.

The $T(0,1)$ mode consists of an axisymmetric torsion of the pipe and it can only be produced by shearing stresses (circumferential motion). In order to only excite this mode, some aspects must be considered.

- At low excitation frequency, the possibility to generate longitudinal and flexural modes is reduced.
- As the flexural modes are not axisymmetric, they can be avoided when the transducer elements are arranged axisymmetrically.
- Excitation frequency must be chosen below or equal to 50 kHz because the cutoff frequencies of the lowest longitudinal and flexural modes in the dispersion phase velocity curve are above.
- Due to that the dynamic magnetic field imposed over the pipe is smaller than the bias magnetic field, it is not expected a meaningful magnitude of longitudinal modes.
- In the group velocity dispersion curve, Figure 3.14, it can be noted the presence of two curved branches, $L(0,1)$ and $L(0,2)$ longitudinal modes. According to [116], The $L(0,1)$ mode has a "low-pass" type cutoff behavior with cutoff occurring at a frequency given as $f_{lowpass}$, and the $L(0,2)$ modes has a “high-pass” type cutoff behavior with cutoff occurring at a $f_{highpass}$, as expressed in Equation (3.21) and Equation (3.22).

$$f_{lowpass} = \frac{\sqrt{E/\rho}}{2\pi R_{mean}} \tag{3.21}$$

$$f_{highpass} = \frac{1}{(2\pi R_{mean})}\sqrt{1+\frac{d^2\,(2+\mu)\,E}{6R_{mean}^2\,(1-\mu)\,(1-\mu^2)\,\rho}}, \tag{3.22}$$

where d and μ are the half-thickness of the pipe wall and the Poisson ratio respectively, R_{mean} is the mean radius of the pipe, and the relation $\sqrt{E/\rho}$ is the rod velocity, where E and ρ are elastic modulus and density of the material respectively.

There is a frequency range between $f_{lowpass}$ and $f_{highpass}$ where $L(0,1)$ and $L(0,2)$ cannot propagate, which is called "Dead zone". Reemplazing the values (E=210 GPa,

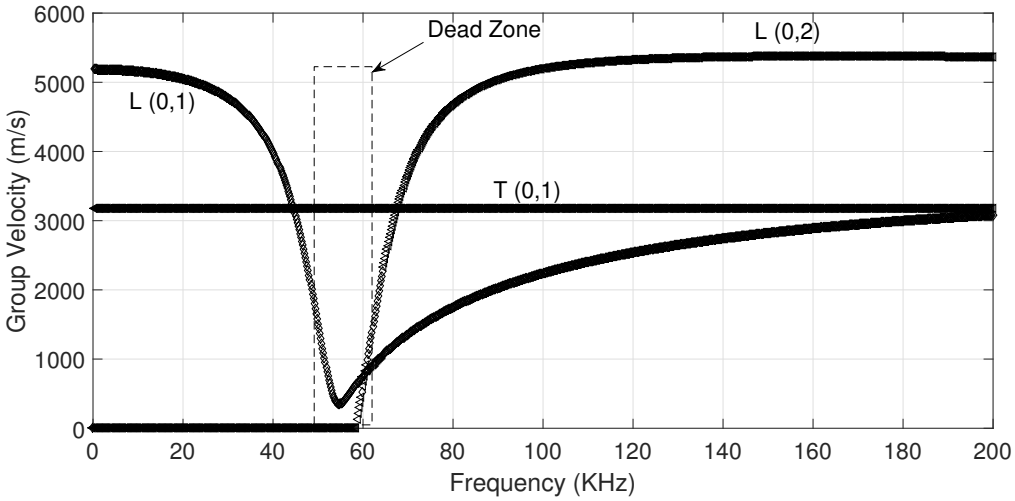

Fig. 3.14 Dispersion curve for A-106, 1" schedule 40

$\rho = 7800$, kg/m^3, $\mu = 0.33$ and $R_{mean} = 15.86$) in Equations (3.21 and 3.22) a range frequency between 55-60 KHz is determined. The same range can be graphically identified in Figure 3.14.

- The width coil should be small or equal to half the wavelength of the target wave mode at an excitation frequency; otherwise, the vibration caused by the wire at the end of the coil will offset each other, reducing the vibration intensity of the expected guided wave mode [56].

Based on the previous considerations and the recommendations of the magnetostrictive transducer provider, a excitation frequency of 50 kHz was chosen. For this frequency a wavelength of 6.5 cm is calculated. Thus, according to the provider the strip has to be smaller than a 1/3 of the wavelength at the excitation frequency. Therefore, a strip and coil of 2 cm of width are used for $T(0,1)$ generation.

3.4 Effect of the source conditions in the wave field in hollow cylinders

Guided waves propagating in the axial direction in a hollow cylinder may involve longitudinal and torsional waves. It has been demonstrated from an analytical point of view, the existence of a doubly infinite number of modes i.e. infinite torsional modes, infinite longitudinal modes and doubly infinite number of flexural modes[39]. The doubly infinite propagation modes have proven orthogonal to each other, therefore they are called normal modes [95]. In

hollows cylinders, flexural modes are non-axisymmetric modes. The longitudinal waves have dominant particle motions in either radial and/or axial directions and the torsional waves have dominant particle motions in the θ direction, as shown in Figure 3.15. The generation of different modes depends on the waveguide and the source loadings conditions. Among the different modes, axisymmetric modes (L or T) are preferred because of their uniform circumferential energy distribution. On the other hand, the acoustic field of non-axisymmetric modes are complex and the volumetric energy distribution is non-uniform.

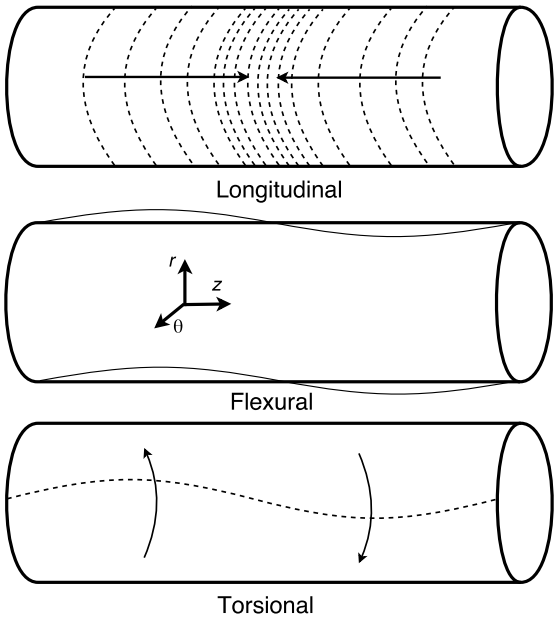

Fig. 3.15 Cylindrical guided waves modes

Now, the excitation of axisymmetric or non-axisymmetric modes is controlled by source loading. For an axisymmetric source loading is expected axisymmetric modes such as longitudinal and torsional. Contrary, if the source is non-axisymmetric only non-axisymmetric modes are excited such as the flexural. The generated guided wave is the result of the superposition of a multiple number of guided waves modes. Non-axisymmetric source loading is preferred in certain circumstances e.g.

- When only a specific portion of the pipe is accessible
- When existing a limited number of actuators
- When it exists economical limitations

Several reasons have motivated the experimental and analytical study of the propagation of non-axisymmetric guided waves, in [98], it has listed the main motivations: The presence

of non-axisymmetric reflections due to irregular acoustic discontinuities, mode conversions, difficulties in generating only axisymmetric modes, etc.

When non-axisymmetric guided waves are propagating, it is need to know in advance the acoustic field and the energy distribution to evaluate the guided waves capabilities to explore the volume under monitoring. Therefore, some considerations must be considered in issues such as:

- Excitation central frequency
- Number and type of actuators
- Actuators dimensions
- Gap between actuators

All the previous items are indispensable to determine the wave field to assure an energy wide coverage of the specimen under test.

The appropriate selection of the guided wave modes is one of the main tasks in the setup of the monitoring scheme based on guided waves. In a cylindrical waveguide with guided waves propagating in the axial direction, the ultrasonic field of a normal mode can be represented by two indices n and m, where m is circumferential order and n is the index of mode group. As mentioned above, three families of modes can be configured in the tubing, longitudinal, flexural and torsional. When $m = 0$, the acoustic field of the modes are axisymmetric along the cylinder circumference i.e. Longitudinal modes $L(0,n)$, and torsional modes $T(0,n)$. Otherwise, the modes are non-axisymmetric, flexural modes $F(M,n)$.

When the loading force is applied in the axial or radial directions of the waveguide, only longitudinal and flexural modes can be generated. On the other hand, torsional modes are excited by applying shear stresses ($\theta - direction$) by using Electromagnetic Acoustic Transducers (EMATs) and contact shear wave transducers.

The different modes present in a cylindrical waveguide can be observed in the dispersion curves. In Figure 3.16 and Figure 3.17, are shown the group and phase velocity dispersion curves for a 1" A.106, Sch 40 pipe. In these figures, for convenience not all the modes have been showed and labeled. Some general observations can be done from these figures:

- For a specific frequency exists multiple numbers of guided wave modes, all of them with different velocities.
- As frequency increases, the number of modes is also increasing and the group-phase velocity difference between the flexural modes and the longitudinal mode of the same family n becomes smaller

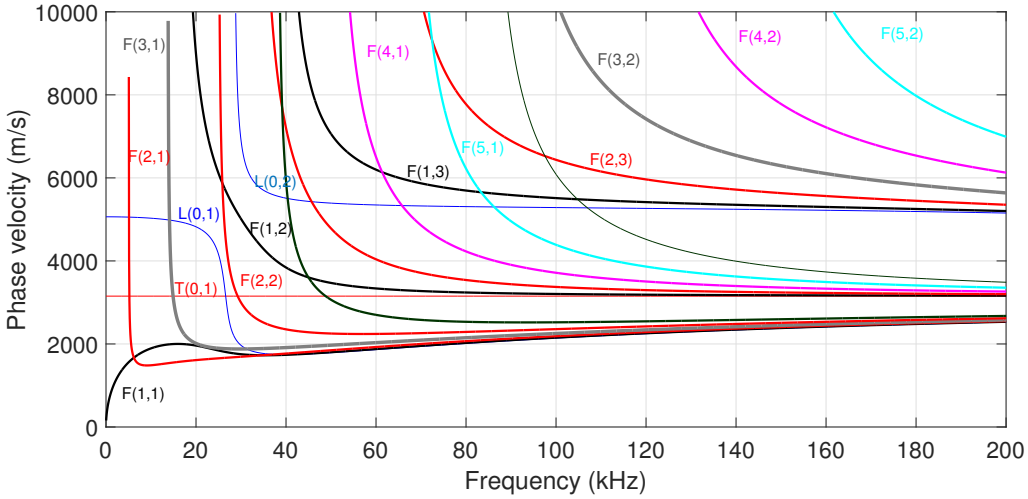

Fig. 3.16 Phase Velocity dispersion curve for 1", A-106, Sch 40. pipe

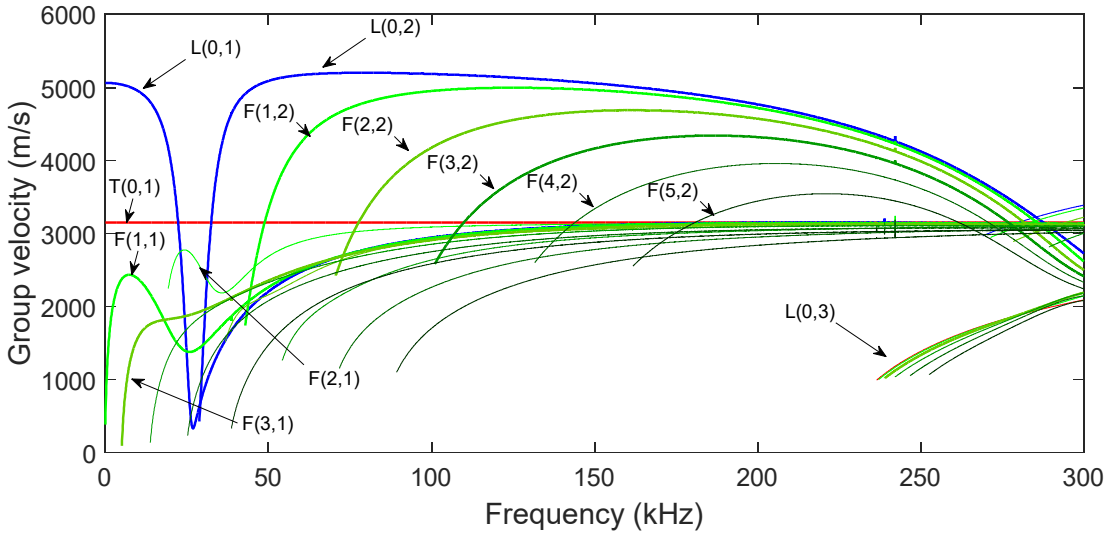

Fig. 3.17 Group Velocity dispersion curve for 1", A-106, Sch 40. pipe

- The phase velocities of the flexural modes are always larger than of longitudinal modes

3.4.1 Superposition principle applied to guided waves propagation

Guided waves propagating in finite structures is a kind of linear problem bearing two important properties: different propagation modes are orthogonal to each other and they behave in a linear fashion. Since the modes are orthogonal, the combination of modes that produces a given displacement field is unique. Likewise, a combination of modes can be converted into a unique displacement field. The linear behavior of the guided wave modes allows each mode to be studied separately and then later combined using the superposition principle [90].

Isolation of a particular mode o group of modes is one of the challenges in the implementation of a monitoring scheme based on guided waves. Axisymmetric loading in a specific bandwidth can produce a well-defined guided wave in time domain. This type of propagation can facilitate the localization of acoustic discontinuities in the explored volume. In the case of non-axisymmetric propagation, the superposition principle is used to determine the set of propagation modes in the guided wave. Amplitudes of each individual mode can be calculated by using the Normal Mode Expansion method (NME) [98, 67, 66, 24].

When the loading force is applied in the axial or radial directions of the cylindrical specimen, the field generated can be represented by the superposition of axisymmetric longitudinal modes $L(0,n)$ and non-axisymmetric flexural modes $F(m,n)$, all of them with different amplitudes and velocities. If cylindrical coordinates are used in the representation of the different wave fields i.e. displacement, stress and strain (u,ε,σ) and the propagation is axial in the $Z-direction$, the longitudinal modes are only functions of the radial coordinate and the flexural modes are a function of both radial and angular coordinates. Stress, displacement and velocity fields can be expressed in a general form as follows:

$$V_f = \sum {R_f}_n^m(r)\, e^{i(m\theta+\omega t-\xi^n z)}, \tag{3.23}$$

where V_f represents the total displacement, stress or velocity (u, σ or v) fields in cylindrical coordinates f, which are independent of the cylinder axial direction z and time t, the function ${R_f}_n^m(r)$ denotes the amplitude of each arbitrary $L(m,n)$ propagation mode, i.e. n mode of the m circumferential order, ω is the angular frequency and ξ^n is the wavenumber of the n mode. Therefore, all wave fields (u, v or θ) can be described as the weighted sum of the contributions of the different activated modes $L(m,n)$, e.g. $\sigma_r = A_3^2(r)\, e^{i\left(2\theta+\omega t-\xi^3 z\right)} + A_1^4(r)\, e^{i\left(4\theta+\omega t-\xi^1 z\right)}$, where σ_r is the resulting sum of the radial stress of the $L(2,3)$ and the $L(4,1)$ modes.

3.4.2 The Normal Mode Expansion Method

The Normal Mode Expansion (NME) method can be used to analyze the multimode propagation of guided waves since this method provides the amplitude of any generated waveguide due to the application of prescribed (time-harmonic) surface tractions or stress. Based on the NME method, the amplitude coefficients for all of the generated harmonic modes are obtained. Due to the difference of phase velocities for different modes, the superimposed total wavefield varies with propagating distances and hence develop specific particular particle displacement distribution patterns (angular profile). This profile will change with the propagation distance. This varying non-axisymmetric angular profile of guided waves represents a non-uniform energy distribution around the hollow cylinder cross-section and thus has an impact on the inspection capability of guided waves [67]. To apply this technique in acoustic, it is needed to develop a procedure for expanding arbitrary acoustic waveguide field distribution as superposition of orthogonal waveguide modes.

The amplitude factor of the generated guided wave harmonics a_n^m can be estimated via NME method. To use this method an orthogonality relation between the waveguide modes should be verified and the complex reciprocity relation must be considered. In [24] and [6] demonstrated the perpendicular character of modal fields of different circumferential orders for u ,σ and v propagating along a circumferential waveguide, e.g. $\sigma_1^1 * \sigma_3^2$ are orthogonal over the cross section of the cylinder; where σ_1^1 is the stress field of the first mode of the first circumferential order and σ_3^2 is the stress field of the third mode of the second circumferential order. In addition, [6] established the proof of orthogonality of guided wave modes in lossless waveguide using the complex reciprocity relation in piezoelectric media, as follows:

$$\nabla \cdot [-v_2^* \cdot \sigma_1 - \sigma_2^* \cdot v_1] = 0 \tag{3.24}$$

Thus, the orthogonality relation between two modes $M(m,n)$ and $M(l,s)$ (M represents either longitudinal mode L or torsional mode T) can be verified via power estimation as follows:

$$P_{m\ln s} = -\frac{1}{4}\iint_D (\overline{v}_{mn}^* \cdot \widehat{T}_{ls} + \overline{v}_{ls}^* \cdot \widehat{T}_{mn}) \cdot \overrightarrow{e_z}\, dV = 0 \quad m \neq l \text{ or } \xi_n^m \neq \xi_s^l \tag{3.25}$$

where D indicates the cross-sectional area of the cylinder and $\overline{v}^*$ and $\widehat{T}$ are the velocity and stress fields of the mode. The asterisk denotes complex conjugation.

Once the orthogonality proof is done, it can proceed with the NME technique. The aim is estimate the a_n^M of each of the modes generated in the cylinder due to a specific external excitation on the boundaries of the waveguide.

For the guided wave generator element shown in Figure 3.18, the loading condition is as follows:

$$\tau_\theta = \begin{cases} P_1(\theta)P_2(z)e^{i\xi_n^m z}\hat{e}_\theta & |z| \le L, \quad |\theta| \le \alpha \quad r = b \\ 0, & |z| > L, \quad \text{or} \quad |\theta| > \alpha, \quad r = b \end{cases} \tag{3.26}$$

where b is the outer radius, $P_1(\theta)$ describes the angular variation and $P_2(z)e^{i\xi_n^m z}$ describes the axial variation of the guided wave mode n of circumferential family m with the applied shear loading. The shear transducer loading is assumed to only produce shear stresses in the θ direction. Such a partial loading can generate a group of torsional modes $T(m,n)$ resulting from the match between the loading condition and modal wave structures. The amplitude factor of each generated mode propagating in the $+z$-direction, a_n^m can be calculated using a normal mode expansion (NME) method as described in [24] using the following expression:

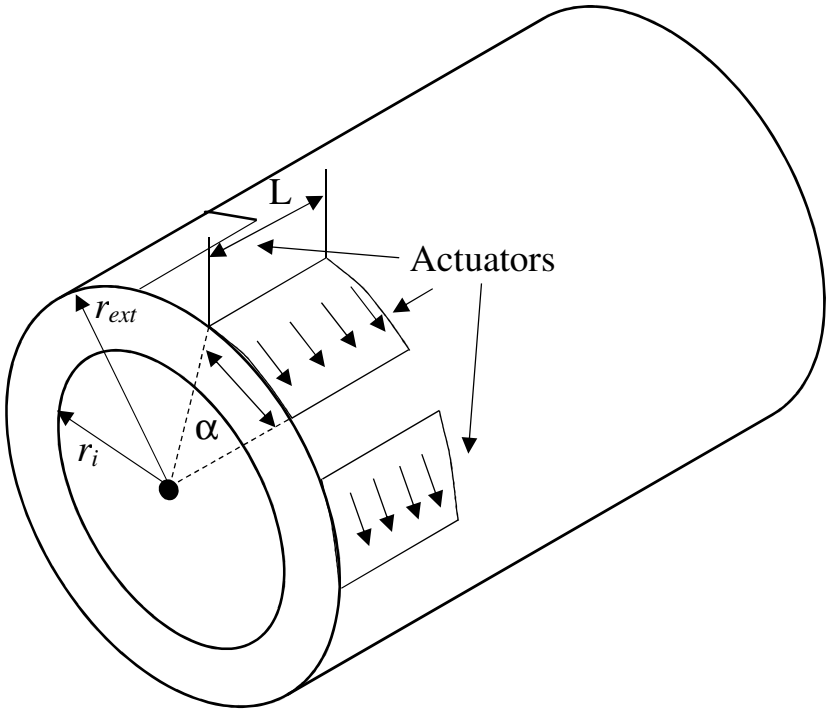

Fig. 3.18 An ultrasonic wave generator is loaded on a hollow cylinder with inner radius r_i and outer radius $r_{ext} = b$. The axial length of the loading is L and the circumferential length is α.

$$a_n^m = -\frac{R_{nr}^{m^*}(b)\, e^{-i\xi_n^m z}}{4P_{nn}^{mm}} \int_{-\alpha}^{-\alpha+2\pi} \Theta_z^n(n\theta)\, p_1(\theta)\, d\theta \int_{-\alpha}^{\alpha} p_2(z)\, e^{-i\xi_n^m z} dz, \tag{3.27}$$

where the superscript * denotes a complex conjugate, R_{nr}^m denotes the amplitude velocity of the n propagated mode with m circumferential order or the radial component value of the wave structure of mode $L(n,m)$ at the outer surface of the cylinder $r = b$. The term P_{nn}^{MM} is the power flow carried by the mode $L(n,m)$ across the cross section D of the cylinder defined by:

$$P_{nn}^{mm} = -\frac{1}{4} \iint_D (v_n^m * \cdot T_n^m + v_n^m \cdot T_n^m *) \cdot \hat{e}_z \, d\sigma \tag{3.28}$$

where v_n^m and T_n^m are the particle velocity vector and stress tensor of mode $L(n,M)$, respectively. It can be clearly seen from Equation (3.27) that the amplitude factor of a generated guided wave mode is determined by three parts [95]:

1. $\frac{R_{nr}^{m^*}(b) e^{-i\xi_n^m z}}{4P_{nn}^{mm}}$
2. $\int_{-\alpha}^{-\alpha+2\pi} \Theta_z^n(n\theta)\, p_1(\theta)\, d\theta$
3. $\int_{-\alpha}^{\alpha} p_2(z)\, e^{-i\xi_n^m z} dz$

The first term is the ratio between the outer surface wave structure value and the power flow of mode $L(n,m)$. This relation describes the excitability of mode $L(n,m)$ for source loading in radial direction. This form arose when it is assumed pressure loading conditions.

The second term describes the effect of the circumferential loading distribution in the excitation of circumferential orders. This term is the inner product of the circumferential distribution of mode $L(n,m)$ and the loading, which represents the likelihood of the loading and mode $L(n,m)$ in the circumferential direction.The better these two distributions match each other, the greater the potential that the mode $L(n,m)$ will be accurately generated. Notice that for axisymmetric source loading the inner product in the circumferential direction vanishes except for $n = 0$ producing only axisymmetric modes.

Likewise, the third term describes how similar the traction distribution in the z-direction is compared to that of mode $L(n,m)$. The more similar they are to each other, the greater chance that the mode will be accurately generated.

To summarize, Equation (3.27) describes the similarity between distributions of the source and the mode $L(n,m)$. The better they match each other, the greater chance that the mode will be generated. Now, for the case at hand, experimentation was realized using an

axial loading by a nonaxisymmetric transducer distribution (only one PZT adhered to the pipe external surface, covering around of 2° of the pipe perimeter) and a circumferential loading for the case of the magnetostrictive transducer (surrounding whole pipe perimeter). At it was predicted by the second term of Equation (3.27), magnetostrictive actuator generated the axisymmetric fundamental torsional mode $T(0,1)$. Contrary, non-axisymmetric loading PZT actuator produced a wavefield rich in overlapped wavepacket. Thus, next, a study of the effect of partial loading in the generation of m circumferential orders is provided.

Now, in the case of the PZT, only the second term provides valuable information because the loading array distribution only contribute to the excitability of circumferential orders. In order to study to estimate the amplitude of the generated modes due to the application of prescribed (time harmonic) surface tractions, the NME is implemented in a Matlab script. Now, the effect of the actuators configuration in the wave field is reduced to the contribution of the second term of Equation (3.29), which is explicitly expressed as [24]:

$$< \theta_r^m, p_1 >= \frac{4ap_0 Sin\left(\frac{m\alpha}{2}\right)}{m} \sum_{\eta=0}^{\frac{I}{2}-1} Cos\left(\frac{m(2\eta+1)\pi}{I}\right) \tag{3.29}$$

Where θ_r^m is the angular characteristic function for m circumferential family modes, p_1 is the applied surface loading condition, α the angular extent of the actuators, a is the inner radios, m the circumferential order, I is the number of PZTs equally spaced elements.

For the studied case here, which involves a finite-sized transducers array which produces shear traction on the outer surface of the cylinder i.e., tangential to the surface, and vanishes outside of the given region, see Figure 3.18 and Equation (3.26), the use of the NME provides some results presented in Figures 3.19-3.20.

As shown in Figures 3.19-3.20 smaller partial loading and small number of traducer equally spaced will make the higher order modes (circumferential orders) have larger amplitudes and also a wave field rich in wavepackets. While undesirable whether the main target is to estimate the time of flight of the propagated wave it may result very appropriate if statistical tools are implemented.

The results presented in Figures 3.19-3.20 can be extended to the experimental tests performed in this thesis with only one PZT attached to the pipe, providing a tangential loading in z direction. Although the analysis is derived for a tangential loading in θ direction, a similar conclusion can be inferred in the case of longitudinal and flexural modes.

Finally, in the case of the magnetostrictive transducer, used in the second part of this thesis, which is adhered around the whole perimeter of the pipe, the second term of Equation (3.29) is reduced to

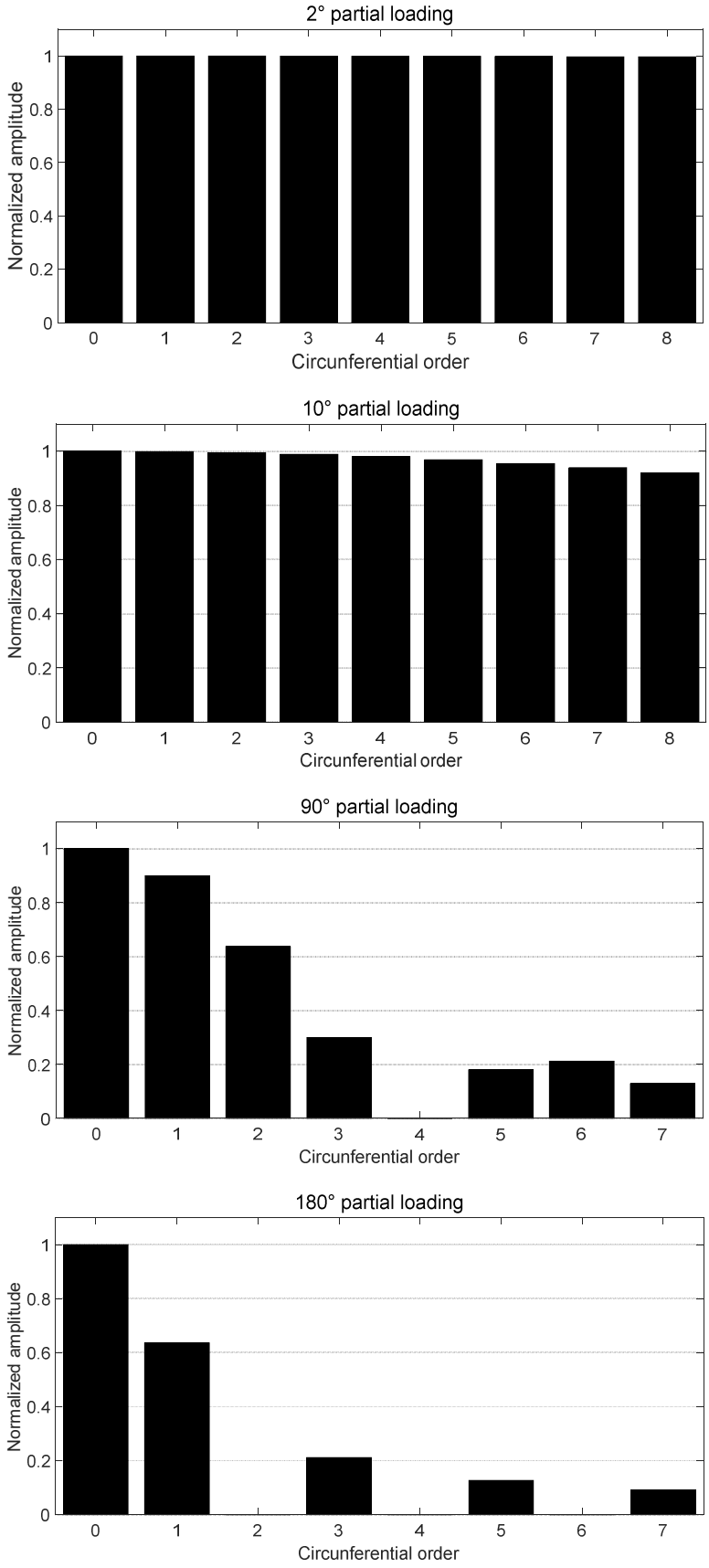

Fig. 3.19 Amplitude factors of axisymmetric and non-axisymmetric modes for torsional family at 100 kHz excited in a 1" Sch 40 pipe by applying in one traducer at 2°,10°,90° and 180° partial loading.

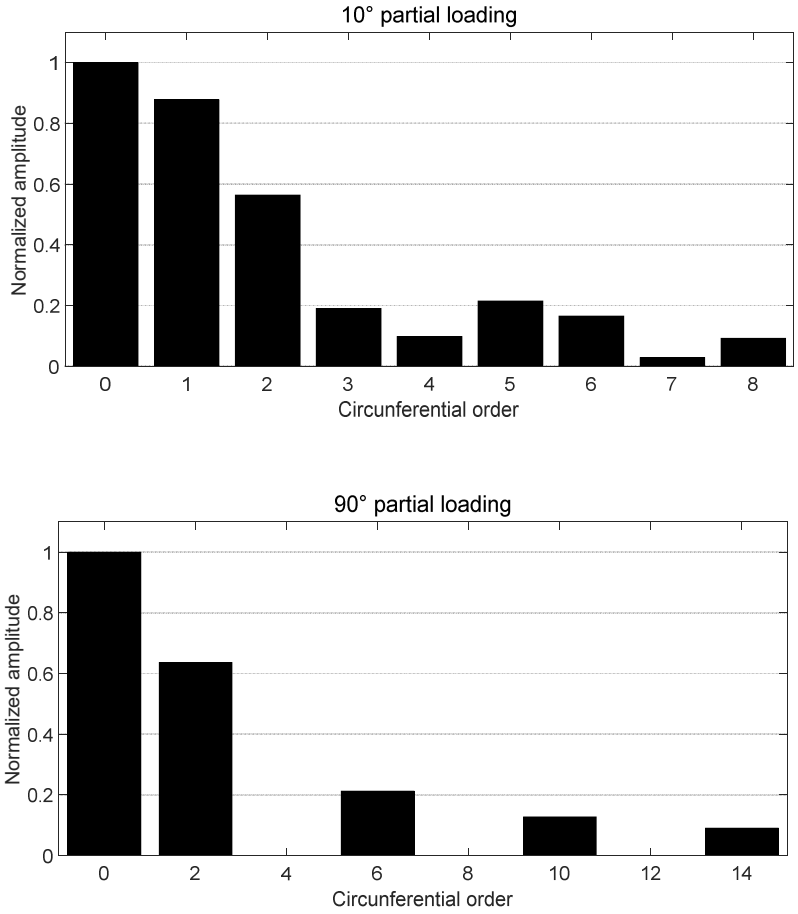

Fig. 3.20 Amplitude factors of axisymmetric and non-axisymmetric modes for torsional family at 100 kHz excited in a 1" Sch 40 pipe by applying in 10 traducers at 10° partial loading and two transducer at 90° partial.

$$< \theta_r^0, p_1 >= p_0(4\alpha a), \tag{3.30}$$

where only axisymmetric torsional modes are generated i.e. $T(0,1)$

Chapter 4

Stress monitoring using PZTs in cylindrical structures

4.1 Introduction

As mentioned in the introduction chapter many structures are exposed to load changes caused by environmental and operation conditions (i.e. temperature and external force variations) which may produce stress variations. This condition can affect the system integrity and a catastrophic condition could be present. So, for some cases, it is imperative to continuously trace variations of the stress condition, where the most widely used transducer is the strain gage. Strain gages presents some limitations such as:

1. High influence of the adhesive layer on its performance.
2. Its focus on stress measurement is limited to the coupling point.
3. Pre-stresses are not exposed once the sensor is attached to the specimen

On the other hand, ultrasonic guided waves, unlike bulk waves and other available NDT methods, have the ability of propagating along relative long distances over the waveguide, preserving its sensitivity to structural condition changes. Thus, guided waves are used for damage detection, damage localization and material characterization.

As mentioned in the Chapter 3, among the suitable transducers to generate guided waves, PZTs are gaining the attention by their light weight and low price. In this research, experimental tests were performed with thin disk PZTs attached to the pipe and excited by a modulated pulse, where a complex wave pattern rich in wavepackets (longitudinals and flexurals) is produced due to the combination of dispersion, multimode propagation and wavefront overlapping.

As above mentioned, analytical studies and experimental tests have shown that Acoustoelasticity effect also have influence in the guided wave velocity producing slight wave pattern changes. However, this method is slightly sensitive to the microstructure effects like grain size [88], texture and structure [1], [102] and operational conditions such as temperature variations [77] and sensor coupling [64].

When guided waves are compared for different stress states at the same temperature, phase shifts are mainly attributed to traveling distance changes of the guided wave (actuator-sensor) and to velocity changes due to the acoustoelasticity effect. Based on the previous phenomena, estimation of stress in a waveguide could be achieved by measuring the Time Of Flight (TOF) of the guided wave among piezoelectric transducers. However, this is a complex task for the following reasons:

1. TOF changes are small in the stressed specimen or waveguide. For example, for metals, TOF variation is less than 0.001 per MPA of applied stress [80], which demands high precision in the experimentation

2. The presence of dispersion, multimode and, wavefront overlapping, due to the waveguide shape, difficulty the estimation of TOF.

Thus, when the structure is subjected to stress, the stress effect in the propagated signal is difficult to perceive because small changes in the total wave pattern are not readily detected. Therefore, in the case of guided waves generated by PZTs in cylindrical waveguides, stress monitoring tasks adopting only the wave observation, without any signal processing tool, would be impractical. Basically, the main reason is because the propagated signal are strongly overlapping making it impossible to specifically observe wave changes (velocity variations) in the individual wavepackets. Additionally, it is also found variations in the amplitude of the captured signal due to an induced voltage in the PZT by an additional strain exerted by the applied stress

The main goal of this chapter is to monitor stress changes in cylindrical waveguides by using ultrasonic guided waves (Longitudinals and Flexurals) generated by PZT's transducers. Firstly, a time domain approach to detect stress changes in hollow cylinders using guided waves is investigated. The proposed scheme makes uses of the subtract method for stress level estimation. Residuals are generated by signal subtraction of the reference signal, at nominal condition, from the current signal.

Secondly, since tracking the variations of wave velocities due to stress are very sensitive to external factors such as temperature, a statistical approach PCA-based initially at room temperature is proposed, attending on the experience of the research group where this thesis

is involved. PCA provides a nominal statistical model of the structure from which any condition deviated from the nominal model can be detected via statistical indices.

Finally, while results of each stress scenario demonstrated the feasibility and potential of using these formulations in the evaluation of the bending stress in hollow cylinders at room temperature, the temperature varying conditions inclusion meaningfully reduce the performance of these schemes. For this reason in the last part of this chapter, a modified scheme is proposed based on an extended statistical PCA-model, in which is contained the underlying temperature influence.

4.2 Experimental Setup

In order to cover a wide range of stress distributions acting in cylindrical waveguides, experimental tests were conducted on two different steel specimens (solid and hollow cylinder); each one is subjected to different stress profiles over the cross-section of the waveguide. For the case of the rod (solid cylinder), the axial stress is applied perpendicular to the cross-section producing an uniform stress distribution. In the case of the pipe (hollow cylinder), the generated normal stress distribution produced by the pipe bending will vary linearly with the radius, yielding compression and tension stresses in the same cross-section.

4.2.1 Steel Rod

A 12.7 mm (1/2") diameter, 0.4m length, AISI 1020 steel rod ($E = 200$ GPa and $\mu = 0.29$) is instrumented with two PZT's, separated by 0.4 m, in a pitch-catch configuration, (see Figure 4.1a). The specimen is subjected to stress by a servohydraulic, MTS universal machine mod 810 (see Figure 4.1b). The stress nominal condition is determined by the unload condition while stressed scenarios are setup with tension and compression axial loads increasing in magnitude from 5 to 10 kN in steps of 1 kN, where each step belongs to a different stress scenario, named S1, S2, and so on consecutively until S6 (25% of the yield stress). The studied stresses in the specimen are in the lower part of the stress-strain diagram, which usually is the expected work zone for an element in a structure.

4.2.2 Hollow Cylinder

A 25.4 mm (1") diameter, 6m length, schedule 40, A-106 ($E = 210$ GPa and $\mu = 0.33$), hollow cylinder is supported at the free ends by fixed supports. In this case, it is decided to applied flexion loads to the specimen. The different stress conditions are produced by changing the magnitude of the load in the middle length of the cylinder, $\frac{L}{2}$, as shown in the

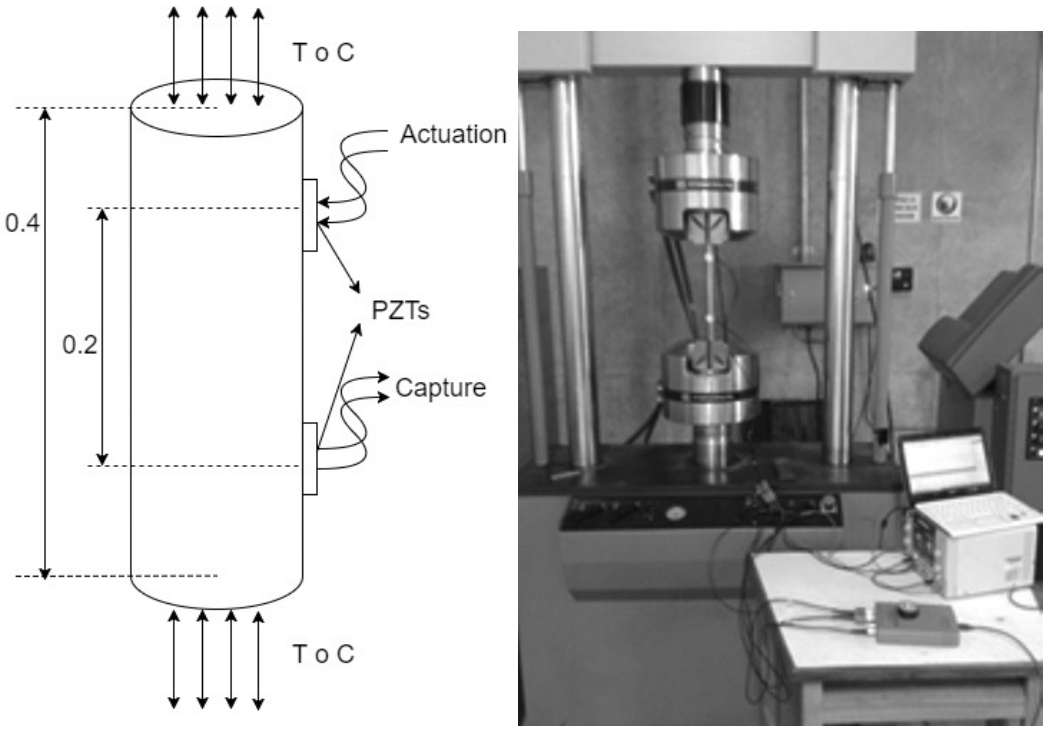

(a) Schematic representation of the rod (b) Experimental mock up of the rod

Fig. 4.1 Rod test bench.

Figure 4.2a. The nominal condition is determined by considering the absence of deflection in the middle length $\frac{L}{2}$ of the cylinder. Under this condition the cylinder is experimenting a negative bending moment and develops an internal stress of 5.96% of the yield strength. Now, the magnitude of the load is changing while the pipeline deflection is increasing in steps of 0.01 m up or down of the original axis position (baseline). Every 0.01 m of deflection constitutes a different stress scenario, in total seven scenarios are studied: five concave upwards deflections and two concave downwards. Concave up deflections are denominated D_1 for 0.01 m, D_2 for 0.02 m and so on consecutively until D_5 for 0.05 m (21.5% of the yield strength), concave down deflections are denominated D_6 for 0.01 m and D_7 for 0.02m up of the baseline. Changes in the load magnitude at the $\frac{L}{2}$ position in the cylinder produce axial stresses. So, a simplified but sufficient analytical model is used to track variations in the normal stress because of force variations. Under this scenario the cylinder can be treated as a beam with constant cross-sectional area in which loads, weights and reactions, are applied perpendicular to its axis. It is assumed that the loads and the reactions are in a simple plane (x,y plane). Given the applied loadings, beams develop an internal shear force V and bending moment M that, in general, vary from point to point along the axis of the beam (cylinder). An expression, invoking the Bernoulli-Euler model for beams, in which the cross section plane initially perpendicular to the axis of the cylinder remains plane and perpendicular to the neutral axis during bending, can be derived (see Equation (4.1)). This expression provides an estimation of the axial stress along the cylinder length $x-$coordinate for all different scenarios considered in the experimental part of this study. At this point, it is noted that the maximum bending stress for a specific longitudinal distance is in the outer distance (exterior radius).

$$\frac{\partial^2}{\partial x^2}\left(\frac{\sigma_{max}}{C}\int_A y^2 dA\right)+q=0 \tag{4.1}$$

where the integral represent the moment of inertia of the cross sectional area about the neutral axis, σ_{max} is the maximum stress, C is the exterior radius and q is the distributed force. Based on the Equation (4.1), an estimation of the maximum stress, in MPa, along the hollow cylinder can be determined as follows: ($Nominal = 12.5$; $D_1 = 9.33$; $D_2 = 17.95$; $D_3 = 26.8$; $D_4 = 36.2$; $D_5 = 45.6$; $D_6 = 24.4$; $D_7 = 36.3$ MPa).

4.2.3 Influence of the Transducer Configuration on the Guided Wave Propagation

Guided waves in this study are generated by thin disks of ceramic material (PZTs) configured in radial mode. PZTs are attached to the testing specimens through an adhesive layer of

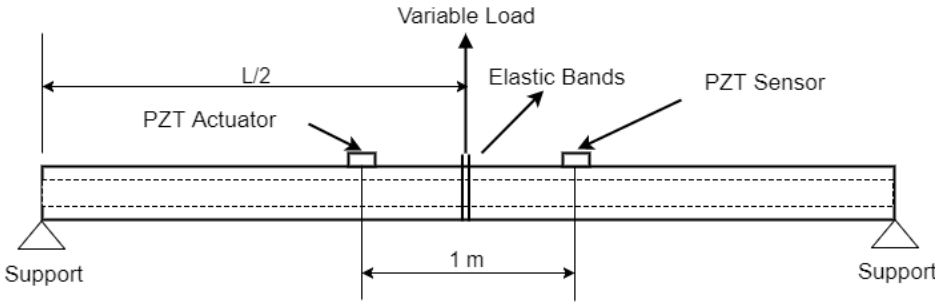

(a) Schematic representation of the pipe

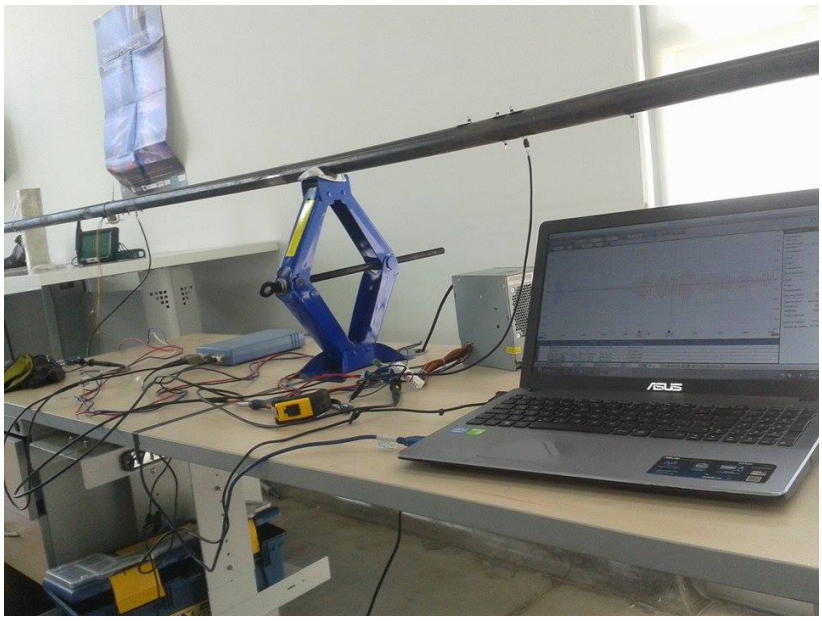

(b) Experimental mock up of the pipe

Fig. 4.2 Pipe test bench.

cyanoacrylate, after a preparation of the surfaces and a settling time of the couplant layer. Among the suitable couplant materials cyanoacrylate has showed high repeatability with low ultrasonic impedance [93]. For the two studied specimens, the excitation pulse of the partially loading PZT attached to the specimen is a 100 KHz, five cycles Gaussian-modulated sinusoidal (See actuated signal in Figure 4.3). The excitation frequency is chosen to match the resonant frequency of the available PZT transducer. The contact area between PZT and the surface is around of two degrees. In consequence, the distribution of the acoustic field generated by the PZT in cylindrical waveguides diverges circumferentially, besides guided waves propagation depends on factors as mode, frequency, cylinder size, propagation and distance [66]. In addition, in the case of the studied waveguides due to a high ratio of wall thickness respect to internal radius, the cylinder contour dominates at very low frequency (wall thickness is far less than the wavelength) yielding a characteristic wave pattern, with a lot dispersion, as a result of the superposition of several guided waves, see the sensed signal shown in Figure 4.3.

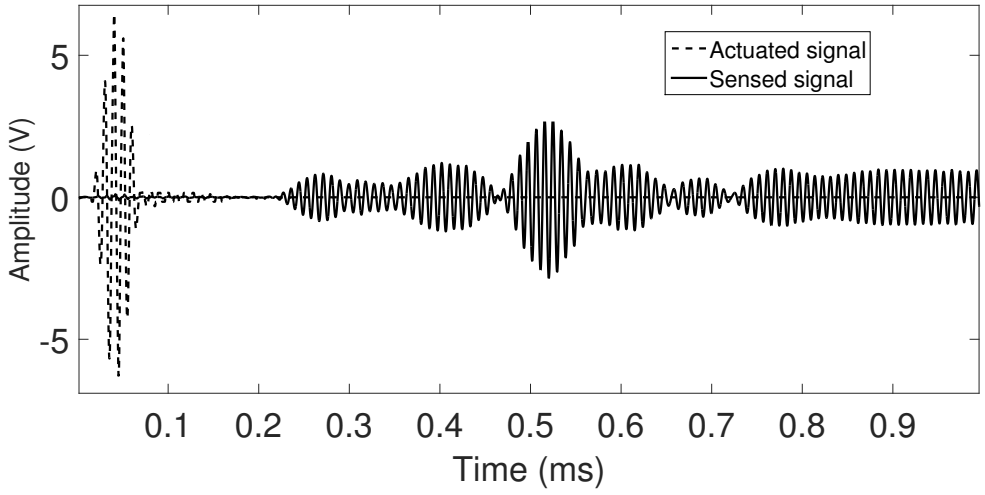

Fig. 4.3 Example of actuated and captured signals in a steel pipe ϕ = 25.4 mm.

According to the normal mode expansion method [98], longitudinal and flexural modes ($L(0,1), F(1,1), F(1,2), F(2,1)$) should be generated by non-axisymmetric surface loading as shown in the dispersion curves depicted in Figures 4.4 and 4.5 [9]. On the other hand, the contour effect generates a lot of wavepackets. Therefore, the wave pattern is rich in modes and wavepackets. Although this type of wave pattern is undesirable for TOF estimation and consequently for localization, it provides the opportunity to implement statistical tools, e.g., PCA. On the other hand, observing an example of the sensed signal for the pipe experiment, as shown in Figure 4.6, slight variations in the phase shift are nonlinear and almost unnoticeable

changes in the amplitude of the waves for different stress scenarios (UND = 12.5, D_1 = 9.3, D_2 = 17.9, D_3 = 26.8, D_4 = 36.2 MPa). Thus, a simple conventional velocity measurement is a complex task because different velocity variations for the same stress are expected for each propagation mode, as shown in Figure 4.6b. This complexity and nonlinear behavior encourages the use of a statistical tool as PCA to detect any slight changes in the wave produced by different conditions of propagation.

Non-axisymmetric source loading is preferred in certain circumstances, for example when only a specific portion of the pipe is accessible, when there exists a limited number of actuators and for economic reasons. The PCA-based algorithm is programmed in Matlab, and a picoscope 2208 is used as DAQ system. A total of 100 experiments were performed and recorded for each stress scenario. The baseline model is obtained by using only 70 experiments, while 30 remaining are used for model validation. The principal components were determined by means of the baseline model, where 60 were retained for a 99.8% of data variability.

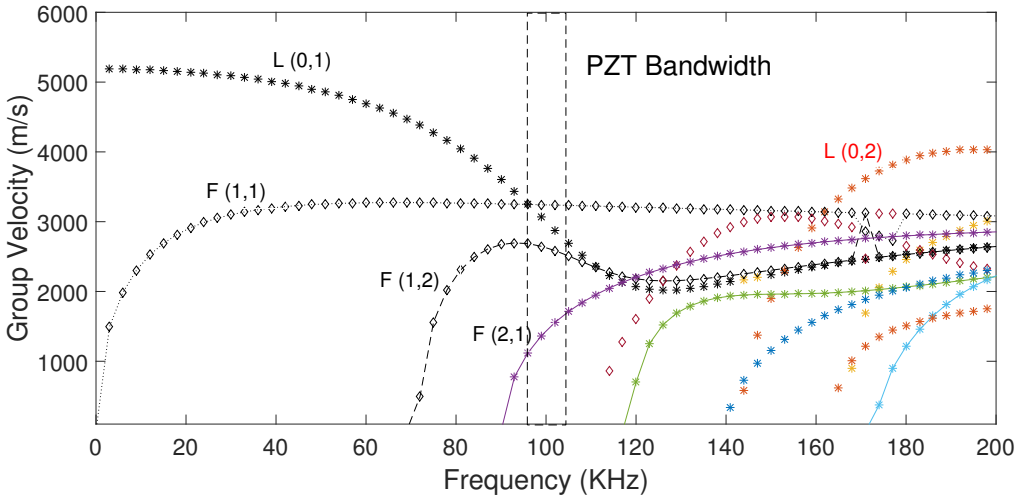

Fig. 4.4 Group velocity dispersion curve for the rod.

4.3 Signal-based stress monitoring approach

4.3.1 Introduction

In SHM schemes, a symptom represents a specific characteristic expressed by a signal resulting from a certain condition in the system. Symptoms of abnormal conditions are

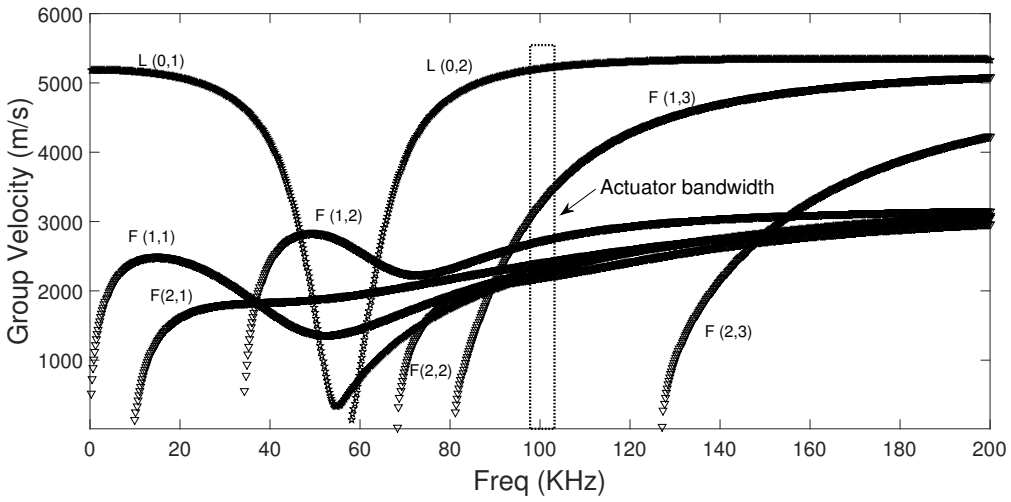

Fig. 4.5 Group velocity dispersion curve for the pipe.

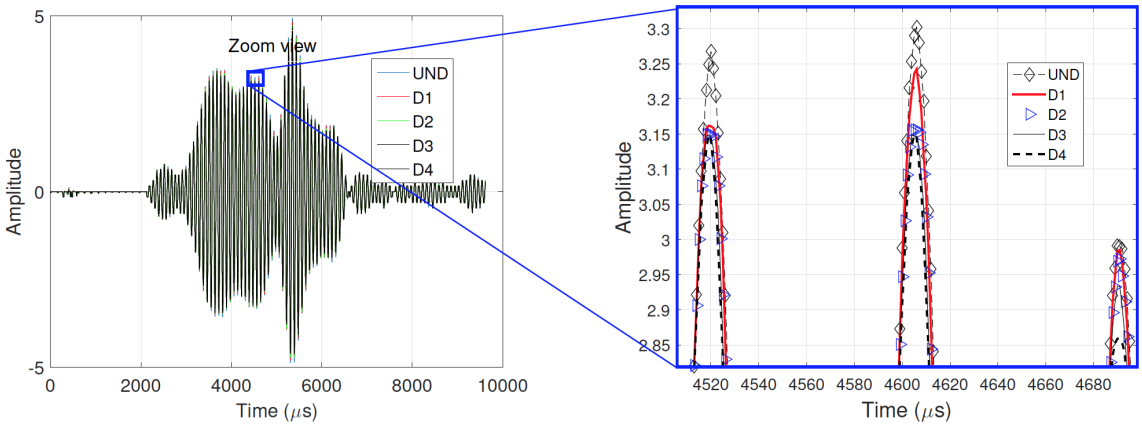

(a) Sensed signals for stressed scenarios (b) Zoom View

Fig. 4.6 Nonuniform variations of phase shift and amplitude for different scenarios.

manifested as deviations of a nominal value evaluated by subtracting the current state to the baseline obtained in the structure nominal condition.

In our case, signal subtraction approach relies on the possibility of estimating the structure condition based on gathered information from the variation observed in the captured ultrasonic signals over time. The assessment of the specimen condition is permanently governed by the residual signal left after subtraction. Residuals are obtained by the simple subtraction of a baseline signal obtained from the structure in a pre-established nominal condition from a signal captured from the structure in operating conditions.

The subtraction approach also relies on the hypothesis that the recorded signal is stable if damage or abnormal condition is not present. If the perfect subtraction between the current signal and the baseline signal were possible to achieve, the presence of an abnormal condition could be deduced from the observation of changes in the residual of the subtraction. In a real inspection problem, where perfect subtraction is not achievable, the occurrence of a new condition can be detected only when the residual of the new condition is sufficiently higher than the residual after subtraction in the nominal condition. Besides abnormal conditions, many other factors may also exert influence on residuals [105].e.g.

- Changes in temperature
- Loading conditions in the waveguide
- Instrumentation drift
- Boundary conditions
- Structural changes
- Other environmental conditions

These influences are undesirable because they may result in a misjudgment of the condition of the system (false alarm). The scope of this work, it is limited to study residuals produced by the presence of loading conditions in the waveguide. Other external factors are beyond of this work and it is left to a future work.

The subtraction approach for the problem at hand is considered because the propagated signal presents a complex wave pattern as a consequence of dispersion, multimode propagation and wavefront overlapping, see Figure 4.7. Basically, the propagated signal is strongly overlapping making it difficult to perceive wave changes (velocity variations) in the individual wavepackets. Therefore, adopting only time domain wave observation without signal processing tools would be impractical.

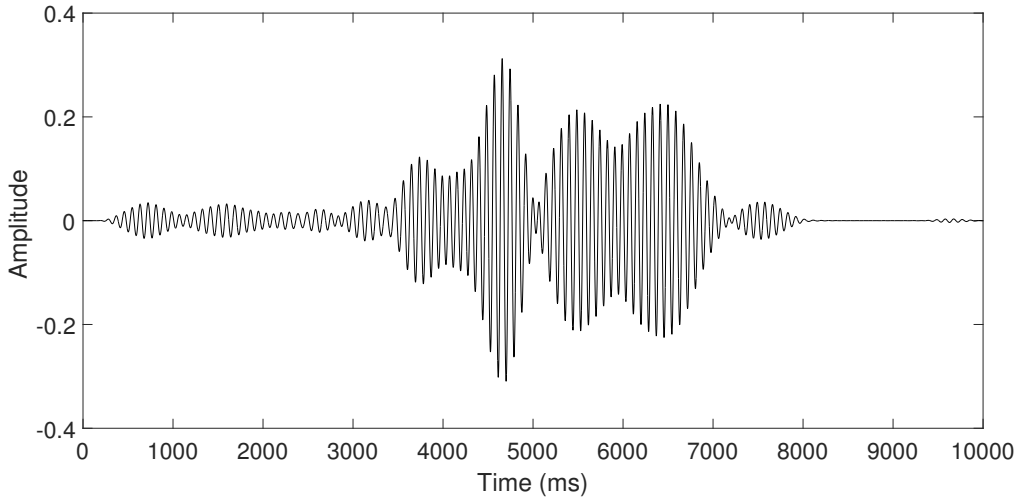

Fig. 4.7 Propagated signal in the pipe

4.3.2 Basic principle

In order to gain a better insight on how guided wave signals are influenced by stress variation, it is followed the analytical approach proposed in [21]. Partial differentiation of time t with respect to σ at constant temperature T in the expression $t = d/v$, where d is the distance between actuator and sensor and v is the propagation velocity, yields .

$$\left[\frac{\partial t}{\partial \sigma}\right]_T = \frac{1}{v}\frac{\partial d}{\partial \sigma} - \frac{d}{v^2}\frac{\partial v}{\partial \sigma}. \tag{4.2}$$

Using the constitutive relation (Hooke´s law) $\sigma = E\varepsilon$,where E is the Young´s modulus and ε is the strain, the following relation is obtained:

$$\frac{\partial d}{\partial \sigma} = \frac{d}{E}, \tag{4.3}$$

and,

$$\frac{\partial v}{\partial \sigma} = k, \tag{4.4}$$

where k is the coefficient of change in phase velocity with stress, the relation given by Equation (4.2) can be written as:

$$\left[\frac{\partial t}{\partial \sigma}\right]_T = \frac{d}{v}\left[\frac{1}{E} + \frac{k}{v}\right]. \tag{4.5}$$

Since k/v is generally significantly greater than $1/E$, in Equation (4.5), it can be concluded that the main contribution to the time shift due to stress variations is given by the

change in the wave velocity with the stress i.e. Acoustoelasticity effect. Furthermore, the time shift is directly proportional to the propagation distance d and since the propagation velocity v appears in the denominator of Equation 4.5, faster modes would be less affected than the slower ones.

Now, when two harmonic signals are subtracted, a new signal emerges with a new amplitude and peak value. Because it is expected changes in velocity by the acoustoelasticity effect and thus time shifts, simulations of shifted time signals are performed to analyze the obtained residual signal.

As it can be inferred, a variation of velocity between the subtracted signals will produce peak positions different to the peak position of the reference signal. In addition, the obtained residual peak magnitude is also influenced by the time shift between the two signals.

In order to grasp a better understanding of the velocity change effect in the subtraction approach. Let us consider three modulated pulses $S_0(t)$, $S_1(t)$ and $S_2(t)$ that have propagated at three different stresses (σ_0, σ_1 and σ_2) for a distance d with velocities $v_{0@\sigma_0}$, $v_{1@\sigma_1}$ and $v_{2@\sigma_2}$ respectively, where ($v_{1@\sigma_1} > v_{0@\sigma_0} > v_{2@\sigma_2}$) all of them slightly different from each other due to the acoustoelasticity effect.

Signal $S_0(t)$ can be considered as the baseline and $S_1(t)$ and $S_2(t)$ as current signals at different stressed scenarios. Due to the presence of different stresses, the arrival times of S_1 and S_2 signals will differ by δt and $-\delta t$. Our aim is to relate the difference in the pulse arrival time to the change in stress of the structure and the residuals behavior. For the sake of simplicity, only stress and deformation in axial-direction are considered. In addition, [105] proposed an expression to estimate the residuals magnitude of 2 shifted pulses by δt with equal magnitude (u_0) and frequency (f), generated by a Hanning window, as follows:

$$R_{Max} = |S_1(t) - S_0(t)| = 2\pi f u_0 \delta t. \tag{4.6}$$

Simulations showed that Equation (4.6) is only strictly valid for $\delta t < 0.5T$, where T represents the period of the signal. Besides, for the same time interval, they reveal residual peak values located ahead in time with respect to the S_0 peak value for $V_{S_1} > V_{S_0} > V_{S_2}$, as presented in Figure 4.8.

As a conclusion, when $\delta t < 0.5T$ and the magnitude of each of the subtracted pulses is the same, the residual peak location does not provide accurate information about the velocity relationship between the current pulse and the reference pulse, i.e. if velocity is increasing or decreasing with respect to the reference signal. Additionally, in Equation (4.6), the residual magnitude is proportional to the δt in both directions, no matter if the signal is delayed or advanced.

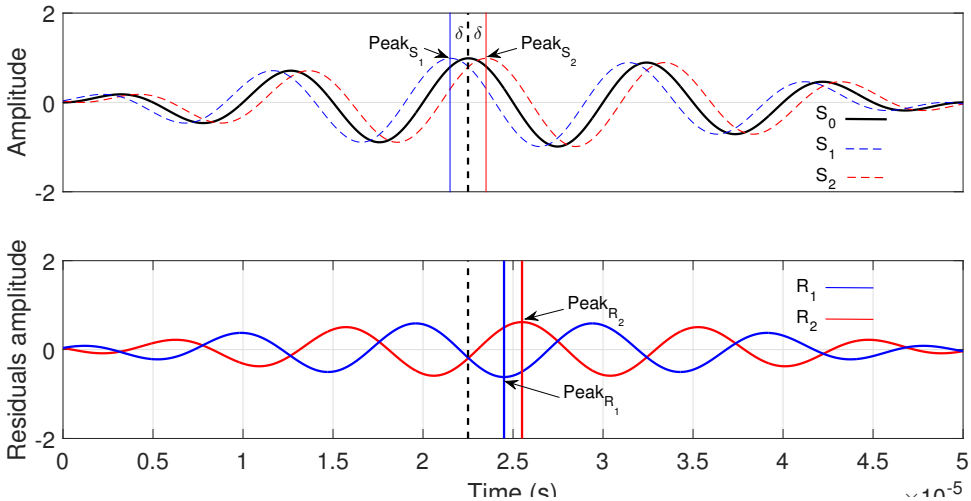

Fig. 4.8 Schematic of the $\delta t = 0.1T$ and residuals signals for a 5 cycle Hanning pulse signals

Now, when $\delta t = 0.5T$, the residual peak value of the subtraction between S_2 and S_0 coincides in time with the S_0 peak value, The acquired residual signal by the subtraction between S_1 and S_0 produces a residual peak location forward of the reference peak value, as shown in Figure 4.9.

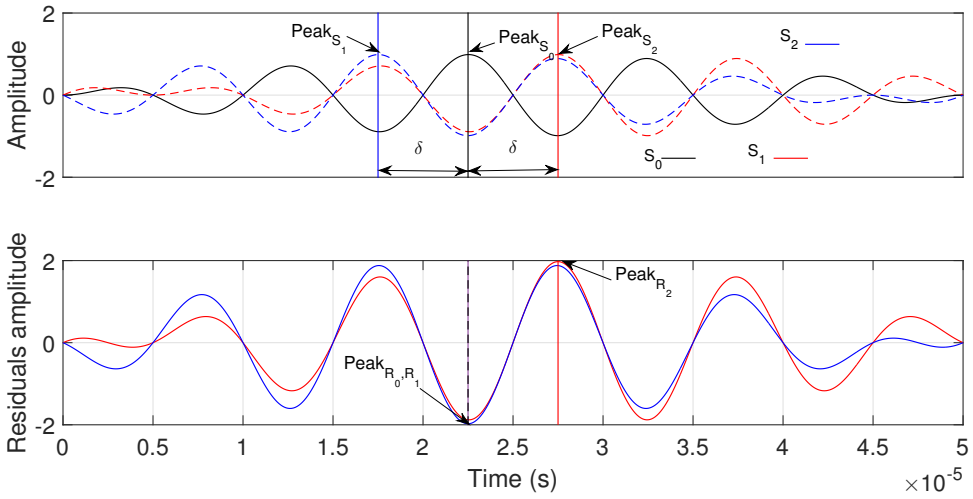

Fig. 4.9 Schematic of the $\delta t = 0.5T$ and residuals signals for a 5 cycle Hanning pulse signals

Last, when $\delta t > 0.5T$, the residual peak value of the subtraction between S_1 and S_0, R_1 signal, is located to the left of the S_0 peak value and the residual peak value of R_2 is ahead of the S_0 peak value, as noted in Figure 4.10.

As a general conclusion, from simulations of pulse velocity variations between waves with the same magnitude in the three studied cases i.e. ($\delta t < 0.5T$, $\delta t = 0.5T$ and $\delta t > 0.5T$),

residual time location and its magnitude do not provide enough information to estimate magnitude and direction of the velocity change when a unique pulse without dispersion is analyzed. Now, as mentioned above, Acoustoelasticity effect produce slight variations of velocity, so it is expected small time shift much lesser than $0.5T$. However, experimental tests at different room temperatures revealed values of δt greater than $0.5T$. For this reason, subtraction approach is not robust for detecting the different levels of stress in a varying temperature environment.

Furthermore, for studied experimental cases in this thesis, where the propagated signal is complex comprised by different wavepackets (multimodal propagation) with the combined effects of dispersion, material elongation and wavefront overlapping, the subtraction approach must be complemented with some signal processing techniques. In our case, based on the experience of previous works of CODALAB, correlation is proposed as the suitable preprocessing step to improve discrimination tasks. In addition, extra signal features (residuals RMS and the current position of the peak value with respect to the nominal position) showed suitable capabilities for discerning among the different stressed scenarios at room temperature.

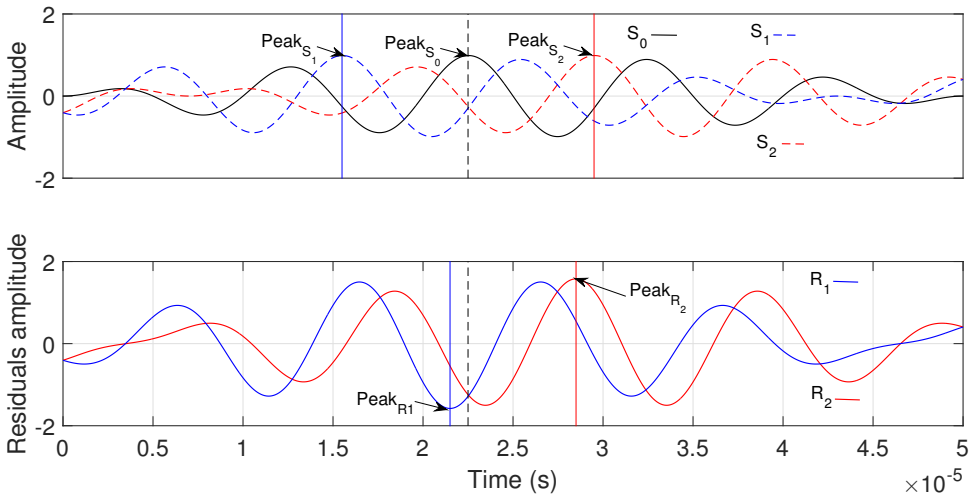

Fig. 4.10 Schematic of the $\delta t = 0.7T$ and residuals signals for a 5 cycle Hanning pulse signals

4.3.3 Subtraction-based stress monitoring approach

This section presents the proposed stress monitoring scheme applied to a pipe subject to bending stress, based on a subtraction approach at room temperature. The guided wave propagation in a specimen under stress compared with the wave in the nominal condition

experiences changes in amplitude and shift. An initial reference time trace, $S_0(t)$, containing guided wave signals is captured from the hollow cylinder. For the purposes of this analysis, it is assumed that this time trace contains just one signal resulting from the nominal condition. In the reference time trace, the signal from the structural feature corresponds to wave propagation over a distance d at velocity v in the time window (t). Later, the presence of stress in the structure has changed and another time trace, $S_1(t)$, is recorded at the same (t) with a different acoustoelastic velocity $v(\sigma)$ and an elongated distance $d_e(\sigma)$. The purpose of this analysis is to estimate the residual signal when $S_0(t)$ is subtracted from $S_1(t)$ at the same room temperature. In this proposal, to improve the residual sensibility a normalized auto correlation of the current signal, r_{xx}, and a cross correlation between the current sensed signal $S_1(t)$ and the nominal sensed signals $S_0(t)$, r_{xy}, are used instead of the raw signals. Examples of these signals are presented in Figures 4.11,4.12 and 4.13. Autocorrelation and cross correlation are calculated as follows:

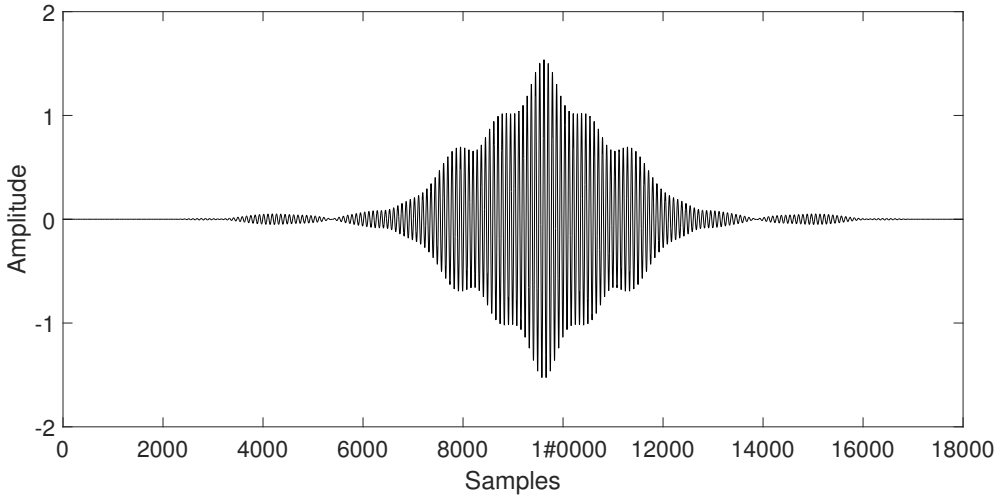

Fig. 4.11 Autocorrelation.

$$r_{xx}(n) = \frac{1}{N}\sum_{n=0}^{N} S_0(n)S_0(n-t), \tag{4.7}$$

$$r_{xy}(n) = \frac{1}{N}\sum_{n=0}^{N} S_0(n)S_i(n-t), \tag{4.8}$$

where N is the number of signal samples, t is defined in the interval $(-N*T_s,(N-1)*T_s)$. Then, residuals R_i, as presented in Equation 4.9, are the difference between the nominal auto correlation, Equation (6.14), and the different stressed cross correlation scenarios, Equation (6.15).

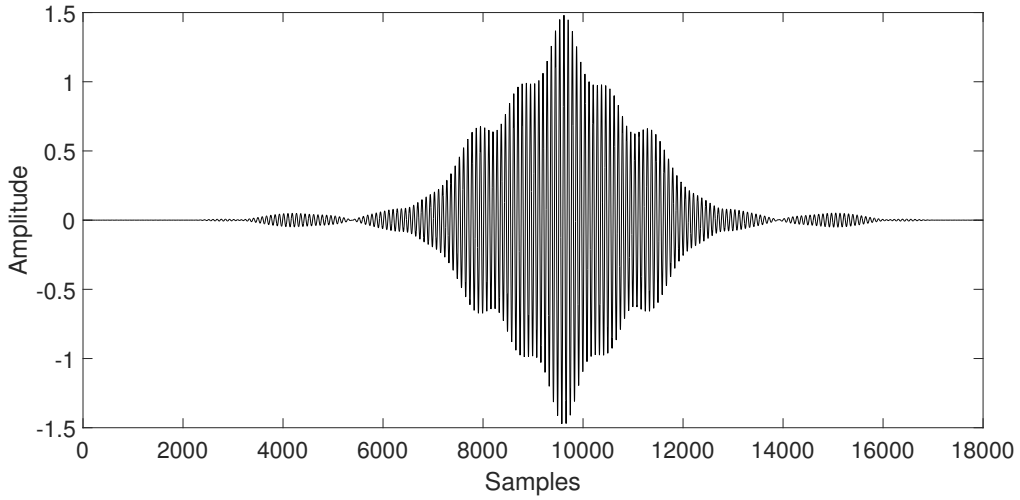

Fig. 4.12 crosscorrelation

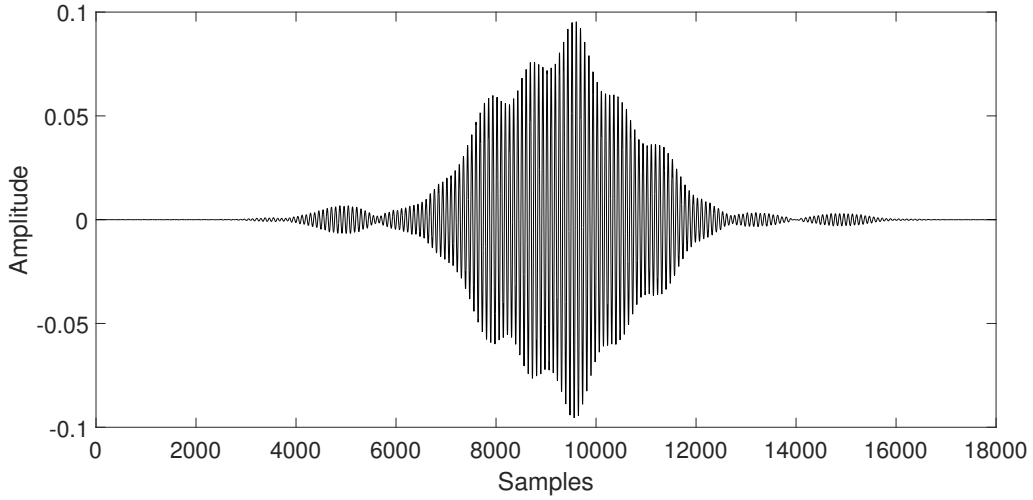

Fig. 4.13 Subtraction.

$$R_i(n) = r_{xx}(n) - r_{xy}(n), \tag{4.9}$$

where i denotes the stressed scenarios. Based on the residual signal, two features for stress monitoring are defined, the RMS value of R_i, Equation (4.10), and the current position of the peak value with respect to the nominal position, named Reference Time (RT), Equation (4.12). The latter feature allows to discriminate between concave upwards and concave downwards cylinder deflection.

$$V_{RMS} = \sqrt{\frac{1}{2N-1}\sum_{t=-N}^{N-1}|R_i(t)|^2}, \tag{4.10}$$

$$(A_i, p_i) = max[R_i(t)], \tag{4.11}$$

$$RT = p_i - p_0, \tag{4.12}$$

where $A_{(i)}$ is the maximum residual value of signal R_i and p_i is the time position of this value and p_0 occurs in the peak of the auto-correlation R_0. The average correlation for each studied scenarios is calculated using 100 experiments. The studied experiments correspond to four concave upwards deflections emulating a loss of supports rigidity and two concave downwards scenarios. Each scenario is obtained changing the deflection of the middle part of the pipe in the test bench, as was mentioned in Section (4.2.2). Figure (4.14) presents the studied scenarios in the plane $RMS - Rt$ at room temperature (22ºC). Every scenario studied correspond to a different level of bending stress in the pipe, which is labeled with the absolute value of the maximum normal stress which can be located in a cross-section along of the distance covered by the guided wave.

4.3.4 Discussion

While the stress estimation and its resolution is not as accurate as the obtained ones using, e.g. dedicated strain gauges, the proposed supervised scheme to estimate bending stress has the benefit of not requiring extra sensors; if guided wave transducers are already in place as part of a structural health monitoring system or in the case of lack of them it is required only a couple of PZTs. Therefore, this method is of particular interest for estimating bending stresses by using the same instrumentation and captured signals that the utilized ones for in situ imaging of damage.

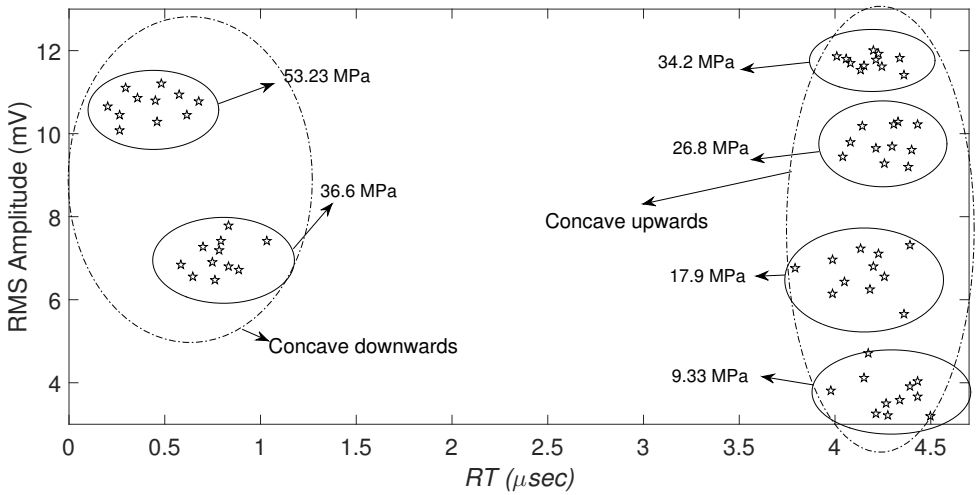

Fig. 4.14 Residual *RMS* and *RT* for the stressed scenarios.

As shown in Figure 4.14, the scatter plot $RMS - RT$ is able to discriminate not only the different stresses but also the hollow cylinder bending shape at low room temperature variation. The *RMS* value tends to growth with the increase of the absolute stress magnitude for both shapes of bending i.e. concave upwards and concave downwards, but the *RMS* value rise is in different proportion for each bending shape. It should be noted that the measurement of absolute stress levels requires reference data taken in the unloaded case before implementing this approach in the field. On the other hand, the *RT* value is close to zero for the bending concave downwards. Thus, not a meaningful time shifting is expected of the correlated signal for this type of bending.

One limitation of this approach is the assumption that there are no other contributions to time shifts than stress variations. Though this assumption may be reasonable in the laboratory, it may not hold in a realistic operating environment where temperature changes can be expected simultaneously with stress variations. Therefore, in the next section, a new robust scheme PCA based is proposed which it will incorporate room temperature changes.

4.4 PCA-based stress for non-varying temperature conditions.

4.4.1 Introduction

The next two sections deal about stress monitoring schemes founded on black box modeling using statistical tools: The first is devoted to present a stress monitoring PCA-based scheme

at slight variations of the room temperature. Next, as a result of analytical studies and experimental tests, it is realized the high influence of temperature in the proposed scheme performance. Thus, stress estimation under varying temperature conditions is tackled using a system extended base of knowledge, as a reference or nominal data, to derive the nominal structure model based on PCA.

The multivariable nature of the stress influence in the wave pattern is experimentally evident comparing signals with respect to a different stress state. It is found varied time shifts for the different wave packets that component the propagated wave captured as a result of different changes in velocity for each propagating mode. Thus, a multivariable statistical tool such as Principal Component Analysis (PCA) can be used as a data-driven modeling approach offering a suitable alternative to track changes in the guided wave produced by the stress. PCA has been previously applied for extracting structural damage features [115]; detection of nonlinearity effects in structural integrity monitoring of offshore jacket-type structures [78], and a simplified solar array system [54]; dimensionality reduction of multiple sensor arrays in structure damage classification [17]; evaluating progressive cracks in a steel sheet and turbine blade of an aircraft [81]; evaluating the tensile stress in a rod [92]; and distinguishing abnormal condition [55].

4.4.2 Theoretical Framework

4.4.2.1 Principal Components Analysis (PCA)

PCA is used in this approach as a data driven modeling technique in order to represent the wave pattern at different structural stress conditions in a new reduced space. This statistical tool has been extensively applied for extracting structural damage features and to discriminate features from damaged and undamaged structures [41, 55, 81].

The main objective of PCA is to distinguish between the most relevant dynamics changes of the system, the redundant information and signal noise. This objective is essentially accomplished by defining a new coordinate space where the variance is maximized and correlation between variables is minimized. In other words, the objective is to find a linear transformation orthogonal matrix $\mathbf{P} \in \mathscr{M}_{I\times K}(\mathbb{R})$ for transforming the original data matrix $\mathbf{X}$ into the form:

$$\mathbf{T} = \mathbf{XP} \in \mathscr{M}_{I\times K}(\mathbb{R}). \tag{4.13}$$

where the matrix $\mathbf{P}$ contains the principal components of the data set or loading matrix and the matrix $\mathbf{T}$ is the transformed or projected matrix onto the principal component space, also called scores matrix. The columns of $\mathbf{P}$ are the eigenvectors of the covariance matrix $\mathbf{C_X}$

organized in descending order of its associated eigenvalue. In this way,

$$\mathbf{C_X P} = \mathbf{P}\Lambda, \tag{4.14}$$

where

$$\mathbf{C_X} = \frac{1}{K-1}\mathbf{X}^T\mathbf{X} \in \mathscr{M}_{I\times K}(\mathbb{R}), \tag{4.15}$$

and Λ is a diagonal matrix that contains the eigenvalues $\lambda_i,\ i = 1,2,\ldots,K$.

The eigenvector with the highest eigenvalue is the most representative component for the data with the largest quantity of information. Geometrically, the j^{th}-column vector (t_j) of the transformed data matrix $\mathbf{T}$ is the projection of the original data over the direction of vector p_j (j^{th} principal component). The projected data in the new space are uncorrelated and have maximal variance, thus it can be potentially the best representation of the process features. Since eigenvectors are ordered according to variance, it is possible to reduce the dimensionality of the data set $\mathbf{X}$ by choosing only a reduced number, $\rho < K$, of eigenvectors related to the ρ highest eigenvalues. In this way, given the reduced matrix $\widehat{\mathbf{P}} \in \mathscr{M}_{K\times\rho}(\mathbb{R})$, the score matrix is defined as

$$\widehat{\mathbf{T}} = \mathbf{X}\widehat{\mathbf{P}} \in \mathscr{M}_{I\times\rho}(\mathbb{R}). \tag{4.16}$$

$\widehat{\mathbf{T}}$ can be projected back onto the original K-dimensional space to obtain a reconstructed data matrix as follows:

$$\widehat{\mathbf{X}} = \widehat{\mathbf{T}}\widehat{\mathbf{P}}^T \in \mathscr{M}_{I\times\cdot K}(\mathbb{R}). \tag{4.17}$$

The difference between the original matrix $\mathbf{X}$ and the reconstructed one $\widehat{\mathbf{X}}$ describes the unrepresented variability in the projections and it is defined as the residual error matrix $\mathbf{E}$ as follows:

$$\begin{aligned}\mathbf{E} &= \mathbf{X} - \widehat{\mathbf{X}} \\ &= \mathbf{X} - \widehat{\mathbf{T}}\widehat{\mathbf{P}}^T \\ &= \mathbf{X} - \mathbf{X}\widehat{\mathbf{P}}\widehat{\mathbf{P}}^T,\end{aligned}$$

so

$$\mathbf{E} = \mathbf{X}\left(\mathbf{I} - \widehat{\mathbf{P}}\widehat{\mathbf{P}}^T\right) \in \mathscr{M}_{I\times K}(\mathbb{R}) \tag{4.18}$$

For simplicity, the caret is removed from the reduced matrices ($\widehat{\mathbf{T}}$ and $\widehat{\mathbf{P}}$) in the rest of the thesis. If Equations (4.16) and (4.18) are analyzed in terms of experimental trials, it can be

obtained that:

$$t_i^T = x_i^T \mathbf{P} \in \mathbb{R}^\rho,\ i = 1,\ldots,I \tag{4.19}$$

and

$$e_i^T = x_i^T \left(\mathbf{I} - \mathbf{P}\mathbf{P}^T\right) \in \mathbb{R}^K,\ i = 1,\ldots,I \tag{4.20}$$

where, $x_i^T \in \mathbb{R}^K$ denotes the vector of the ith experimental trial (ith row of the original matrix $\mathbf{X}$), vector t_i^T is the projection of x_i onto the first ρ principal components (ith row of the score matrix $\mathbf{T}$) and e_i^T is the residual error of the ith experimental trial (ith row of matrix $\mathbf{E}$).

4.4.2.2 PCA Based indices

One well-known PCA statistical index used to distinguish abnormal behavior in a process is the Q-statistic or Square Prediction Error (SPE)-statistic.This index uses the residual error matrix $\mathbf{E}$ to represent the variability of the data projected on the residual subspace. The Q-statistic is based on the assumption that the underlying process follows approximately a multivariate normal distribution, where the first moment vector is zero. Therefore, this index denotes that events are unexplained by the reduced model. In other words, it is a measurement of the difference, or residual, between a sample and its retrieved version by using the reduced model. The Q-statistic of the ith experimental trial is defined as the sum of the squared residuals of each variable as follows:

$$Q_i = \|e_i\|^2 = e_i^T e_i = \sum_{\ell=1}^{K} e_{i,\ell}^2 \tag{4.21}$$

$$= x_i^T \left(\mathbf{I} - \mathbf{P}\mathbf{P}^T\right)\left(\mathbf{I} - \mathbf{P}\mathbf{P}^T\right)^T x_i \tag{4.22}$$

$$= x_i^T \left(\mathbf{I} - \mathbf{P}\mathbf{P}^T - \mathbf{P}\mathbf{P}^T + \mathbf{P}\mathbf{P}^T\right) x_i \tag{4.23}$$

$$= x_i^T \left(\mathbf{I} - \mathbf{P}\mathbf{P}^T\right) x_i \tag{4.24}$$

where $e_{i,\ell} \in \mathbb{R}$ denotes the ℓth element of the vector e_i, $\ell = 1,\ldots,K$.

PCA studies also include *Hotelling's T^2-statistic* index. This statistical index is a generalization of *Student's t-statistic* that is used in multivariate hypothesis testing. It denotes the inner change of principal component model. T^2-statistic of the ith experimental trial is defined by the averaged sum of its projection into the new space as follows:

$$T_i^2 = \sum_{r=1}^{\rho} \frac{t_{i,r}^2}{\lambda_r} = t_i^T \Lambda^{-1} t_i \tag{4.25}$$

$$= x_i^T \left(\mathbf{P}\Lambda^{-1}\mathbf{P}^T\right) x_i \in \mathbb{R},$$

where $t_{i,r} \in \mathbb{R}$ denotes the rth element of the vector t_i –the projection onto the rth principal component or rth score of the i experimental trial–; and $\lambda_r \in \mathbb{R}$ is the rth eigenvalue. T^2-statistic only detects variations in the plane of the first ρ principal components which are greater than what can be explained by the common-cause variations. In other words, the T^2-*statistic* is a measure of the variation in each sample within the PCA model. Normally, Q-*statistic* is much more sensitive than T^2-*statistic*. This is because Q is very small and therefore any minor change in the system characteristics will be observable. T^2 has great variance and therefore requires a great change in the system characteristic to be detectable.

4.4.3 Methodology

This section presents the contribution of this work in the field of stress monitoring in cylindrical structures, experimentally validated in a stressed and piezo-actuated steel rod and tube. The proposed methodology for stress monitoring based on PCA consists of two stages: (i) modeling and (ii) stress monitoring (see Figure 4.15).

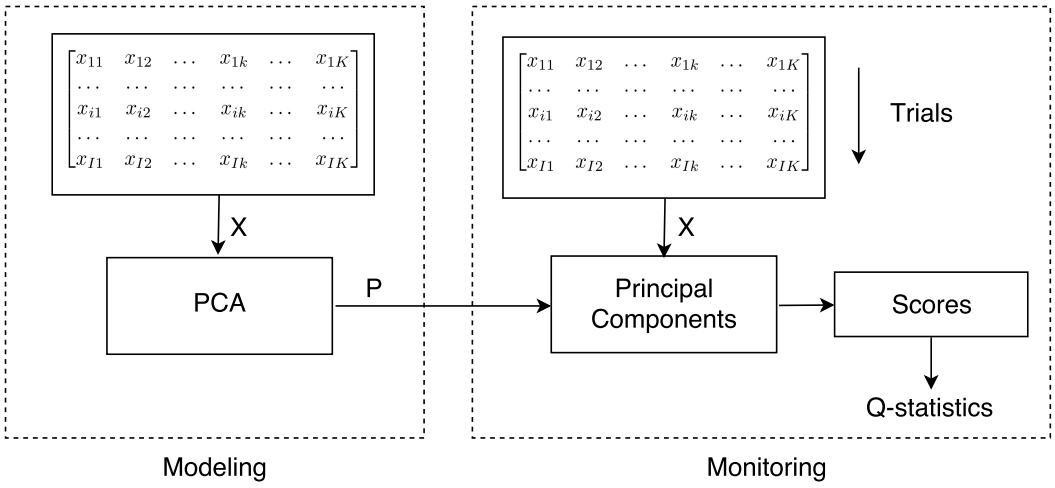

Fig. 4.15 General scheme of the proposed PCA based stress monitoring.

4.4.3.1 Modeling

In this stage, a statistical data driven model for the nominal condition of the piezo-actuated specimen is constructed by using PCA. The next steps are followed:

1. A set of I experiments are conducted on the specimen at nominal condition (residual or initial stress). The experiment consists of exciting the specimen by a PZT, via a modulated pulse at a single probe position and capturing the guided wave by a PZT,

at a point distant from the excitation, such that the interest zone is covered. This measurement is repeated several times (experimental trials). The collected data are arranged as follows:

$$X = \begin{bmatrix} x_{11} & x_{12} & \dots & x_{1k} & \dots & x_{1K} \\ \dots & \dots & \dots & \dots & \dots & \dots \\ x_{i1} & x_{i2} & \dots & x_{ik} & \dots & x_{iK} \\ \dots & \dots & \dots & \dots & \dots & \dots \\ x_{I1} & x_{I2} & \dots & x_{Ik} & \dots & x_{IK} \end{bmatrix} = \begin{bmatrix} x_1 \\ \dots \\ x_i \\ \dots \\ x_I \end{bmatrix} = (v_1|v_2|\dots|v_k|\dots|v_k) \tag{4.26}$$

This $\mathbf{X} \in \mathscr{M}_{I\times K}(\mathbb{R})$ is the vector space of $I \times K$ matrices over $\mathbb{R}$, which contains information from K discretization instant times and I experimental trials. Each row vector (x_i) represents measurements from the sensor at a specific i^{th} trial. In the same way, each column vector (v_k) represents measurements at the specific k^{th} discretization instant time in the whole set of experiments trials.

2. Cross correlation analysis is applied between the acting and sensing signals of the I experiments to eliminate noisy data trends.

3. The correlated signals are arranged in the matrix $\tilde{X}$ for I experiments of *2K-1* samples, conducted on the same scenario in order to consider noise and variance due to the stochastic nature of the technique.

4. The matrix $\tilde{X}$ is normalized by considering each column as a measured variable and normalized to mean zero and variance equal to one for the I experiments. This step minimizes bias and scale variance effects. The Equations (4.27)–(4.29) are used for the mentioned preprocessing.

$$\mu_j = \frac{1}{I}\sum_{i=1}^{I} x_{ij}, j = 1,...,(2K-1) \tag{4.27}$$

$$\mu = \frac{1}{I(2K-1)}\sum_{i=1}^{I}\sum_{j=1}^{2K-1} x_{ij} \tag{4.28}$$

$$\sigma = \sqrt{\frac{1}{I(2K-1)}\sum_{i=1}^{I}\sum_{j=1}^{(2K-1)} (x_{ij}-\mu)^2} \tag{4.29}$$

where μ_j is the mean of the experimental trials in the same column of $\tilde{X}$, and μ and σ are the mean and standard deviation of all elements of $\tilde{X}$.

Thus, a normalized cross-correlated undamaged matrix $\tilde{x}$ is obtained in a new reduced space of coordinates with minimal redundancy and whose elements correspond to the scaled values of the raw data according to:

$$\tilde{x}_{ij} = \frac{x_{ij} - \mu_j}{\sigma}, i = 1, ..., I, j = 1, .., (2K-1) \tag{4.30}$$

Then, a baseline statistical model is obtained, which consists of a linear transformation (**P**) extracted from the singular value decomposition of the covariance matrix $\tilde{x}$, according to that described in the previous section.

4.4.3.2 Monitoring

The monitoring stage consists of representing the currently acquired signals into the PCA space by means of the *Q-Statistics* using Equation (4.16). The monitoring principle consists of relating changes in the guided wave produced by the presence of stress with changes in the *Q-Statistics* index. In this phase, several experiments are conducted over the steel rod and the tube under load conditions, in order to discriminate different stress states by computing the *Q-Statistics* index and comparing it with the baseline values. The general procedure for detecting and distinguishing stresses on structures based on PCA is depicted in Figure 4.15.

4.4.4 Experimental Results

Several stressed scenarios were sequentially applied on the two specimens (steel rod and hollow cylinder) during a fixed time window. Then, a DAQ and signal processing is implemented to compute the magnitude of the *Q-statistics* index for each sequential trail.

4.4.4.1 Rod

In the case of the rod, stresses were applied by using a MTS equipment. Experimental results are illustrated in Figure 4.16 where, it is depicted the *Q-statistic* index (Q-index) by each stress scenario (40 MPa, 47 MPa, 55 MPa, 64 MPa, 72 MPa and 79 MPa). It is observed different relations between stress and Q-index: one for compression and the other for tension conditions. It can be seen also an increasing Q-index with the absolute stress in both conditions.

These results can be attributed to: (i) the different phase shift in the wavepackets, produced not only for the change in distance between the PZTs as a result of the deformation but also for the acoustoelasticity effect, and (ii) an amplitude variation of the sensed signal due to the induced voltage across the PZT terminals. This voltage is yielded by the sum of two strains:

the one produced by the stress applied to the specimen which is transmitted to the PZT via an adhesive layer, and the latter produced by the dynamic perturbation (guided wave). These two reasons affect the pattern wave in different ways for each load configuration. In other words, for the same stress, the Q-index value is different for compression and tension.

This observation suggests the limitation of the proposed technique to distinguish tension and compression stresses. However, in many real applications, due to the mechanical system configuration in terms of loads, the information of the type of stress can be established a priori or considered redundant.

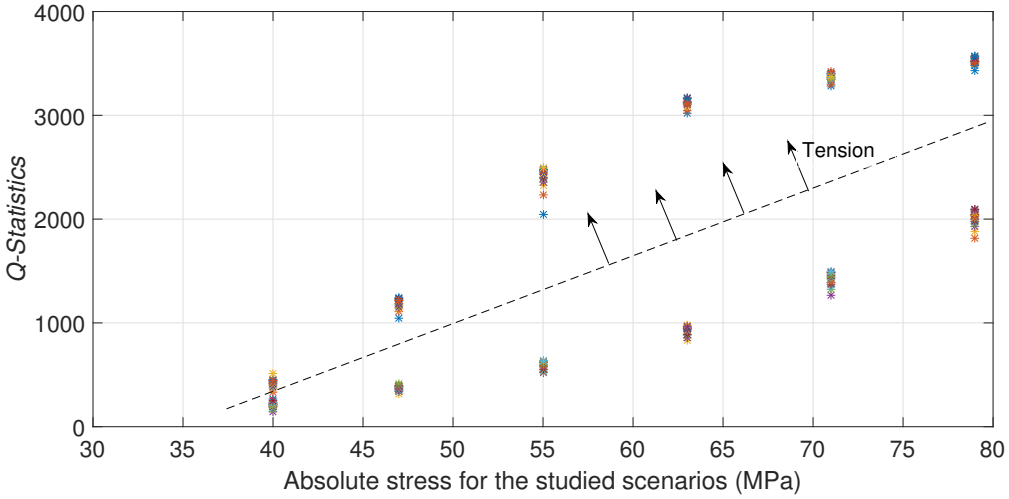

Fig. 4.16 *Q-statistic* for different tension stress scenarios in the rod.

4.4.4.2 Hollow Cylinder

In the case of the hollow cylinder, each stress scenario is well defined by applying different forces in the $\frac{L}{2}$ position with a consequent normal stress generation function of the distance by bending. Experimental results are similar to the presented in the rod case. Figure 4.17 depicts the Q-index by each stress scenario. It is also observed different relations between stress and Q-index: for concave up and for concave down conditions. It can be seen also an increasing Q-index with the absolute stress in both conditions. It is also observed that the Q-index for the D_6 and D_7 scenarios (Concave down) present a decrease regarding the trend of the concave up scenarios. This behavior may be attributed to reasons described in the rod case and also to a wider stress range along the propagation path of the guided wave. Figures 4.18 and 4.19 illustrate the difference between the maximum and the minimum stress for each scenario, e.g., D_4 exhibits $\sigma_{max} = 36.22$ MPa and $\sigma_{min} = 35.12$ MPa ($\Delta_\sigma = 1.1$ MPa), in contrast D_7 has $\sigma_{max} = 36.29$ MPa and $\sigma_{min} = 17.39$ MPa ($\Delta_\sigma = 18.9$ MPa). Clearly, a

large difference means a guided wave propagation in some structure regions with much less stress than used to identify the scenario (σ_{max}), so Q-index shows a consistently increment in magnitude with the stress even in a nonuniform stressed waveguide. Similarly, as shown in the rod case results, the proposed technique is not able to distinguish between concave up and concave down bending.

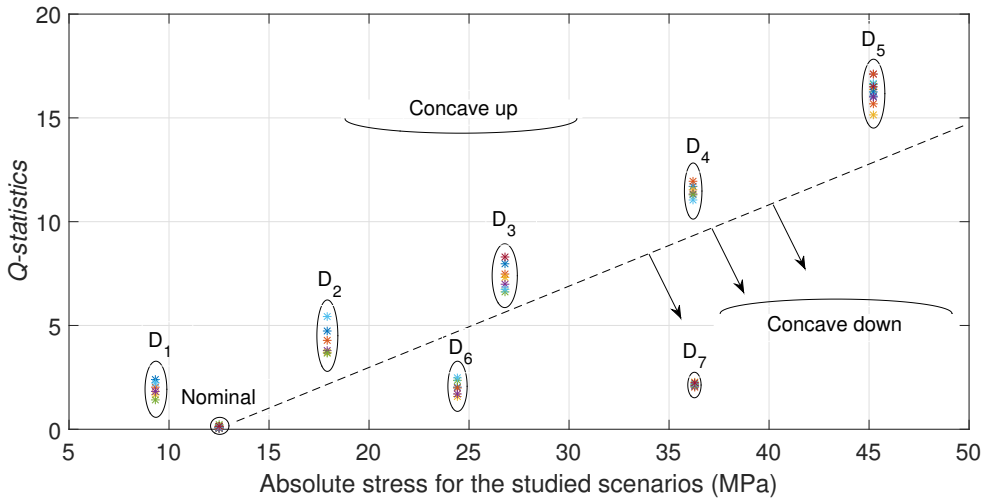

Fig. 4.17 *Q-statistic* for all studied scenarios for the hollow cylinder.

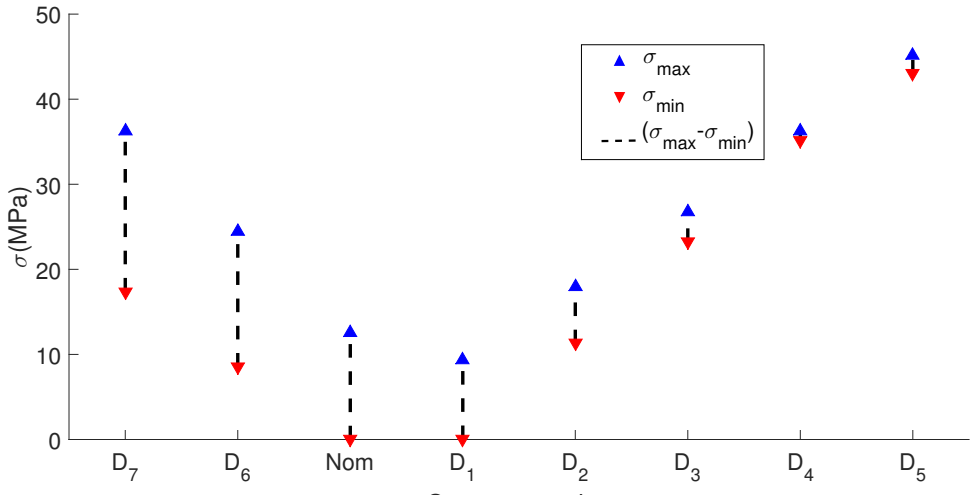

Fig. 4.18 Maximum, minimum and difference of stress by each studied scenario.

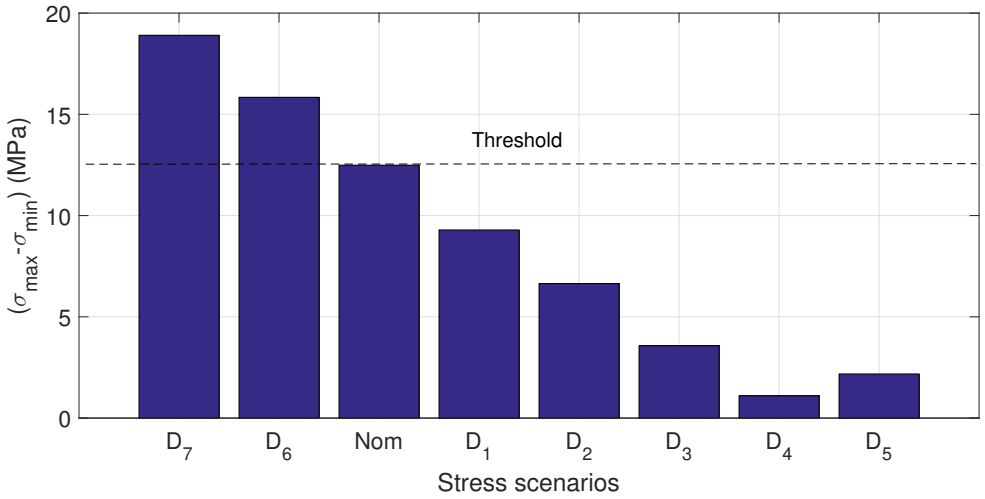

Fig. 4.19 Stress difference by each studied scenario.

4.4.5 Discussion

In this section, a PCA based methodology for monitoring stress conditions at room temperature using PZTs is proposed and experimentally validated in two cylindrical specimens: a solid cylinder (steel rod), subject to a pure axial load, and a hollow cylinder (pipe), subject to bending. The proposed methodology is not intended to estimate stress absolute values, but instead it is able and suitable to track stress variations with respect to a nominal stress state.

The effectiveness of the proposed monitoring scheme was demonstrated to yield stress features indicators and to discriminate different stress scenarios. PCA technique, in particular the Q-index, is a good tool for detecting the presence of different stress conditions, by comparing the current index values with the nominal value via a threshold.

In a structure subjected to stress, stress variations cause changes in the arrival time of the signal due to the elongation or shortening of the path between actuator and sensor. Additionally, a change in the wave velocity is also expected due to the acoustoelasticy effect. Both mentioned effects produce a slight phase shift in the received wavepacket, which were verified by means of the experimental tests. Besides, these experiments revealed variation in amplitude for the different stress scenarios.

In general, in a stress monitoring scheme, PZT-based in a pitch-catch configuration, magnitude changes in the induced voltage across the PZT terminals (i.e., amplitude of the captured signal) are yielded by the sum of the strains due to applied stress and the microstrains produced by the guided wave propagation. All these changes of the ultrasonic guided wave by propagating in a stressed medium can be easily tracked using the proposed methodology.

Specifically, the studied scenarios in the steel rod and the pipe covered the first part of the elastic region of the specimen (not damaged yet). In this region, the proposed strategy was clearly able to distinguish variations in the stress conditions with enough capability to discriminate among them. However, it does not distinguish whether the specimen is subject to tension or compression (rod case), nor the type of bending (pipe case).

Although, the proposed methodology is able to recognize different stress scenarios, the estimation of the applied stress magnitude requires further experimentation in order to determine the appropriate statistical relation. However, in the case of the rod, changes in the stress are with regard to the unstressed condition, hence it can provided a close absolute value of the actual stress once the type of load, tension or compression, is known beforehand. Therefore, the studied index constitutes a base for implementing a classifier algorithm to differentiate stress structural conditions.

4.5 PCA-based stress monitoring for varying temperature conditions

4.5.1 Introduction

In this section, a PCA-based robust stress monitoring scheme is proposed. Robustness in this section refers immunity to changes of temperature to estimate the stress condition. Although formerly it was demonstrated high capabilities of the PCA-based scheme to estimate external mechanical stresses, all the experimentation was performed at room temperature. Since temperature influences in material properties, the geometry of the waveguide and the transducers; whichever monitoring scheme based on wave field pattern recognition substantially reduces its effectivity in estimating the actual conditions when changing environmental conditions such as temperature are present. Experimental and numerical simulations of the guided wave propagating in materials under different temperatures have shown significant variations in the amplitude and the velocity of the wave [21, 40, 43, 74, 30, 48, 3, 111]. This condition can jeopardize the discrimination of the different stress scenarios detected by the PCA indices. Thus, it is proposed a methodology based on an system extended knowledge base, composed by a PCA statistical model which cover the nominal state at different discrete temperatures to produce a robust classification of stress conditions under variable environmental conditions.

4.5.2 Temperature effect on guided waves propagation

Several studies have been achieved to realize the effect of temperature on SHM schemes and the potential side effects on signal-based or model-based monitoring approaches. The side effects of this condition are the result of:

- Changes in properties of:
  1. Piezoelectric transducer (elastic properties, piezoelectric constants)
  2. Bounding layer
  3. The structural substrate (elastic properties, density).
- Thermal expansion affecting geometrical parameters in all component of the monitoring scheme such as:
  1. Thickness
  2. Length

There are many reported effects of temperature fluctuation in the guided wave. The first effect and probably the most noticeable is the amplitude variation. In general, it is reported a magnitude reduction when the temperature is increasing [40]. In addition to the amplitude reduction is also found a velocity decrement (increase time of arrival) as the temperature is raising [102].

The main causes of the effects previously mentioned are explained considering the significant parameters in the guided wave propagation i.e. the Young´s moduli, piezoelectric properties, thermal expansion. In general, a significant decrease in the Young modulus with increasing temperature causing a reduction in velocity. The piezoelectric constants as cited in Section (3.2.4), Equation (3.4), in particular the piezoelectric strain constant d_{31} and the piezoelectric voltage constant g_{31}, vary significantly with the temperature. While d_{31} constant is associated with the actuation, the g_{31} constant is associated with the piezo-sensor sensitivity. The thermal expansion produces alterations in the geometric parameters and a change of length in the path of propagation, causing a translation of the received signal in time. In [21], it is presented an analytical model of the variation of the arrival time TOF or δt with respect to the temperature δT, see Equation (4.31).

$$\delta t = \frac{d}{v}\left(\alpha - \frac{k}{v}\right)\delta T, \tag{4.31}$$

where α is the coefficient of thermal expansion of the waveguide material, typically on the order of $10^{-5}\ {}^{0}C^{-1}$ for metals, d is the distance between actuator and sensor and v is the

wave velocity. The relationship between wave velocity (due to changes in stiffness) and temperature can be written as $\frac{\delta v}{\delta T} = k$, where k is typically of the order on $10^{-1}\ ms^{-1}C^{-1}$. Based on the relations reported by Equation (4.31) and the magnitude order of the variables in it, we can infer that the change in velocity due to changes in temperature is the dominant effect rather than the thermal expansion of the structure. In addition, the term d in Equation (4.31) may assume the proportionality of time shift with distance between emitter and receptor.

As a conclusion, because the proposed stress monitoring depends on features associated to the wave pattern; temperature varying conditions in the system substantially alter the recorded waveform and its effects can jeopardize any intent to detect stress variations in the structure. Experiments have shown nonlinear changes of amplitude and velocity along the propagated wave. In Figure 4.20, it can be observed different time windows of the same captured guided wave along the pipe for different temperatures. As noted in Figure 4.20, different time delays and amplitude changes with respect to the reference state (28 °C) are present for each window. So, all analytical intent to estimate the temperature effect over the wave is a complex task.

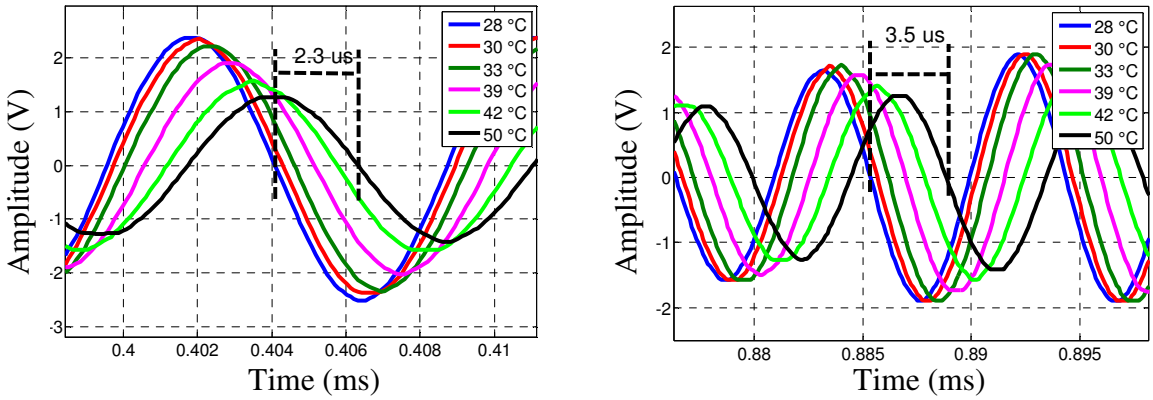

Fig. 4.20 Non-linear behavior in amplitude and velocity of the guided waves in presence of different temperatures for different time windows.

In some conditions, the temperature varying effect in the propagated wave can be highly relevant and influence directly the monitoring result. In [21], it is observed variations in the wavepacket attributed to the temperature more pronounced that the abnormal studied condition. Thus, temperature robustness is an obligate requirement of practical applications SHM schemes based on guided wave pattern recognition.

4.5.3 Temperature effect on the PCA-Based stress monitoring scheme

Experimental test are performed to verify the effectiveness of the proposed scheme under different room temperatures. The baseline is obtained at 25°C room temperature and no special preprocessing is applied to the captured signal. Four different stressed scenarios are experimentally studied ($D1$= 1 cm, $D2$=2 cm, $D3$= 3 cm and $D4$= 4 cm of downwards deflection of the middle part of the pipe). The entire initial tests are performed twice to check repeatability letters D and P are used to identify the different test rounds. In Figure 4.21 can be observed the different configured clusters in the $(T^2 - Q)$ space for each tested scenario at room temperature. Every cluster is clearly distinguishable of each other for the same stress conditions at room temperature.

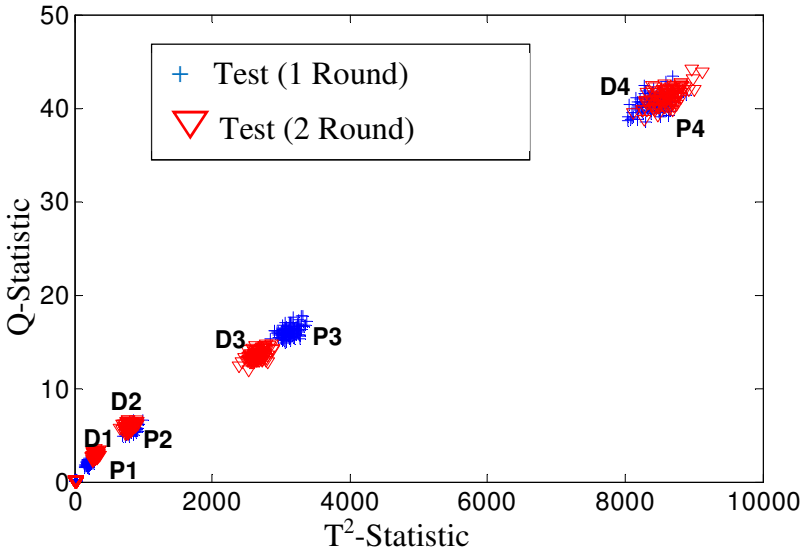

Fig. 4.21 Validation of the proposed methodology at room temperature (25°C) without an extended baseline.

On the other hand, in Figure 4.22 is given the temperature effect on the couple $(T^2 - Q)$, by using the implemented PCA-Based monitoring scheme, in a temperature range between 25°C and 50°C. As presented in Figure 4.22, the configured clusters pertaining to different temperatures at nominal load condition (No deflection in the middle part of the pipe) are further (bigger values of $T^2 - Q$ coordinate) compared with the index values that belong to the stress region at room temperature of 25°C. While for the maximum studied stress condition (4 cm of deflection in the middle part of the pipe) the $Q - index$ is around 40 at 25°C room temperature, the $Q - index$ for a normal condition (no deflection) at room temperature of 50°C reports a $Q - index$ around 1250. Therefore, any attempt to detect a

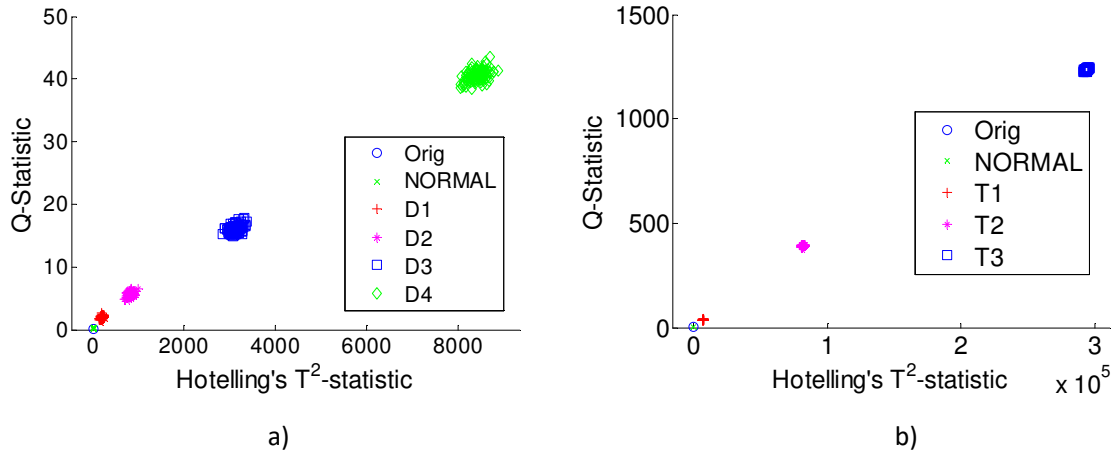

Fig. 4.22 Statistical indices for a) stressed scenarios at the same room temperature. b) nominal stress condition at temperature varying conditions, Normal=25°C, T1=30°C, T2=38°C and T3=50°C

stressed condition under a different room temperature can produce a false alarm by using the implemented monitoring scheme.

4.5.4 Modified PCA-Based stress monitoring scheme

The challenge of the modified methodology is to discriminate between temperature variations in an unloaded specimen and changes in stress, in a temperature-varying environment. The difficulty arises because both produce the same signature in the wave, i.e. changes in amplitude and velocity. In fact, in some of the experimentally studied cases, room temperature variations produce changes (amplitude and velocity) in the wave field more pronounced than the stressed condition being monitoring. This behavior results in bigger values of the proposed statistical indices, T^2 and Q.

The proposed PCA-based robust stress monitoring scheme has the same structure that the previous explained in Section (4.4.3). Only some changes are needed to increase the approach robustness to temperature variations. For the sake of brevity, changes in the scheme steps are just enumerate as follows:

1. A $\mathbf{X}^T$ matrix which superscript T stands for each room temperature is assembled using the normalized cross-correlation between the launched and captured signals. To improve the signal-to-noise ratio, 100 signals are captured and recorded for each scenario of stress condition. Captured signals or experiments are rows in the $\mathbf{X}^T$ matrix

2. An extended baseline,$\mathbf{X}_{Ext}$, i.e. a bigger $\mathbf{X}$ matrix containing the wave pattern for a discrete range of temperatures between 24°C and 38°C, is assembled as shown in Figure 4.23. Thus, X_{Ext} column size now is $\mathbf{X}^T$ column size times the number of discrete wave pattern at different temperature added to the extended baseline.

3. The couple (T^2-Q) statistical indices is determined in the post-processing stage.

$$X_{Ext} = \underbrace{\begin{bmatrix} x_{11} & \cdots & x_{1m} \\ \vdots & \vdots & \vdots \\ x_{n1} & \cdots & x_{nm} \end{bmatrix}}_{X^{28°C}} \underbrace{\begin{bmatrix} x_{11} & \cdots & x_{1m} \\ \vdots & \vdots & \vdots \\ x_{n1} & \cdots & x_{nm} \end{bmatrix}}_{X^{30°C}} \cdots \cdots \underbrace{\begin{bmatrix} x_{11} & \cdots & x_{1m} \\ \vdots & \vdots & \vdots \\ x_{n1} & \cdots & x_{nm} \end{bmatrix}}_{X^{38°C}} \begin{matrix} Exp_1 \\ \vdots \\ Exp_n \end{matrix}$$

Fig. 4.23 Schematic representation of assembly of the X matrix

In the diagnosis stage, the $\mathbf{X}$ matrix for the current state signal is projected onto the PCA model obtained using the extended baseline. Projections onto some of the first components are obtained and the indices (T^2, Q) for the stressed scenarios are calculated and compared with the baseline values. Values of the couple ($T^2 - Q$) for each scenario studied are shown in Figure 4.24, shapes and colors represent different conditions of the pipe under test. In order to verify inference capabilities, the room temperatures used to create the X_{Ext} matrix were different to the room temperatures in the diagnosis or validation stage. In Figure 4.24, it is shown the result for the different stressed scenarios at different room temperatures. The results are obtained after the implementation of the preprocessing and using an extended base of knowledge.

4.5.5 Discussion

Comparing the configured statistical index clusters for different temperatures at different stresses scenarios in Figure 4.24, it can be noted, they are grouping around a limited and defined region. A substantial improvement is appreciated estimating the stressed condition in a varying temperature environment with respect to the scheme without the preprocessing and the extended knowledge base.

As a conclusion, the proposed monitoring scheme, based on an extended data matrix X_{Ext} including data (wave patterns) at different room temperatures; as an input to generate the statistical model of the nominal condition, is effective unmasking the temperature effect in the statistical indices. Some slightly variations are presented in the diagnosis stage under

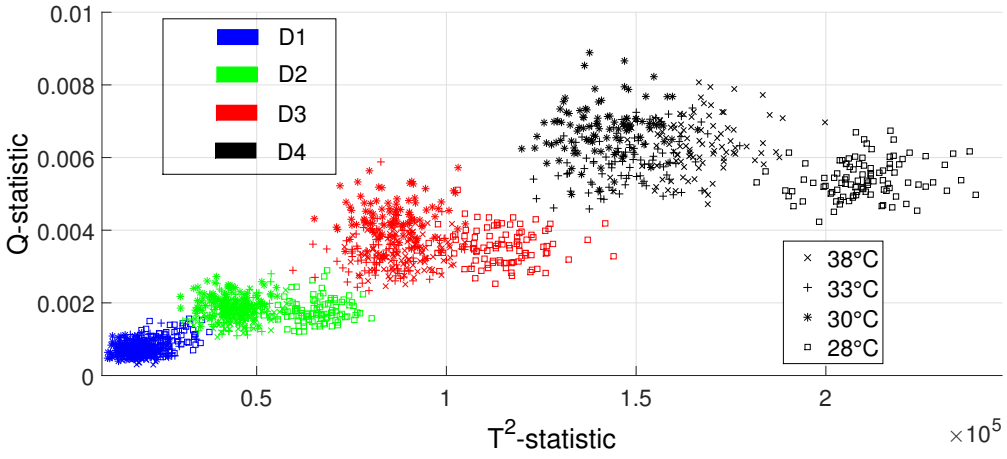

Fig. 4.24 Statistical PCA indices at different stress conditions and at different room temperatures (28°C, 30°C, 33°C and 38°C)

different surroundings temperatures. In order to assure an appropriate monitoring, the same piezo-actuation (PZT couple) must be maintained in the range of temperatures used in the setting stage. The guided wave pattern is highly dependent of the PZT parameters and the characteristics of the adhesive layer. In addition, although the proposed alternative is suitable in the temperature range presented, higher temperatures significantly influence the performance of the proposed monitoring scheme. Thus, a more extended research has to be done searching for a less sensitive to high temperatures monitoring scheme.

Chapter 5

Dispersion curves of uniaxially stressed plates by combining Effective Elastic Constants and SAFE Method

5.1 Introduction

As mentioned in previous chapters, dispersion curves are required to characterize the propagated guided wave pattern at a certain frequency. The exact trace of the dispersion curves is obtained by using transcendent equations assembled by either the transfer matrix or the global matrix methods [72]. Recently, the Semi-Analytical Finite Element (SAFE) method has been proposed to compute rapidly and efficiently the dispersion curves for any constant cross section specimen. SAFE has been used to analyze wave modes in cylindrical waveguides [118, 50, 47, 75], to calculate leaky lamb waves [51], to obtain the dispersion curves in a pipe elbow [52] and in materials with viscoelastic properties [7].

The influence of stress on guided wave propagation is relevant to both nondestructive evaluation and structural health monitoring because of changes in received signals due to both the associated strain and the acoustoelastic effect. The dispersion curves in stress-free isotropic and anisotropic specimens have been widely studied and they can be adequately described based on the theory of elasticity. However, this formulation is insufficient to describe wave propagation in specimens under stress since small non-linearities in the stress-strain relationships become significant, which can be described by using the acoustoelasticity approach. The available literature devote to study the dispersion curves for stressed waves is limited. Nowadays, it is restricted to two main research lines: One, is devoted to consider that dispersion of propagating waves becomes directionally dependent in presence of load.

Under this consideration, stressed wave propagation is studied as an anisotropic problem using in this case the Christoffel equation and the fourth order tensor in the resulting wave equation. This approximation is followed by [36],[35],[37]. The second one approach has been considered by [69],[70],[71], [76] and it uses an extension of the Semi-Analytical Finite Element (SAFE) method applying the full strain–displacement relation due to initial finite strains in the structure. Then, the wave equation is derived in linearized incremental form, where the pre-stressed configuration is considered to slightly deviate from the corresponding unstressed one. In these researching works have been demonstrated a proportionality between the stiffness matrix, required to describe the effect of axial load and the mass matrix, which makes the use of existing software (stress-free) trivial to obtain the dispersion curves for waveguides under stress.

In this chapter, it is proposed the use of effective elastic constants (EEC) in a SAFE framework to calculate the stressed guided wave dispersion curves, considering the anisotropy effect present when an unidirectional load is applied in an isotropic plate. In the context of studies on ultrasonic wave propagation in stressed media (acoustoelasticity), a classic formalism can be considered (second order) by replacing the elastic constants with EECs for which the influence of stress is taken into account [28].

Then, the isotropic specimen subject to loading in one direction is studied by proposing an equivalent stress-free anisotropic specimen. This approximation facilitates determining the dispersion curves by using the well-studied numerical solution for the stress-free cases. Finally, numerical data available in literature were used to validate the proposed methodology, where it could be demonstrated its effectiveness as approximated method.

5.2 SAFE Analytical Model

In SAFE methodology, the waveguide is discretized over the cross section, while in an analytical solution is considered or given in the wave propagation direction. Based on a variational scheme by inserting the kinetic and potential energies into Hamilton´s equation, a system of linear equations can be constructed with the circular frequency and wave number as unknowns under stress-free condition. The unknowns can be solved using standard eigenvalue routines. Therefore, SAFE approach allows computing dispersion curves in waveguides with complex cross sections, such as: multilayered laminates [38] and rails [71, 53, 2], where it is often computationally complex to solve analytical solutions. For semi-infinite waveguides, SAFE has a better performance compared with the traditional FEM due to only the constant cross-section is considered, which reduces the computational cost.

Additionally, SAFE does not have missing roots problem, found in matrix methods, when dispersion curves are computed [60].

In our case, SAFE methodology is derived for an isotropic, homogeneous, and stress-free plate assumed as an infinitely wide waveguide, where the wave propagates along direction x with wavenumber ξ_x and circular frequency ω, see Figure 5.1. Since, the cross-section of the plate lies in the $y-z$ plane, the analysis is formulated as a two-dimensional problem in the plane strain formulation. Thus, the harmonic displacement (u), stress (σ) and strain (ε) field components in cartesian coordinate at each point of the waveguide are expressed by Equation (5.1)

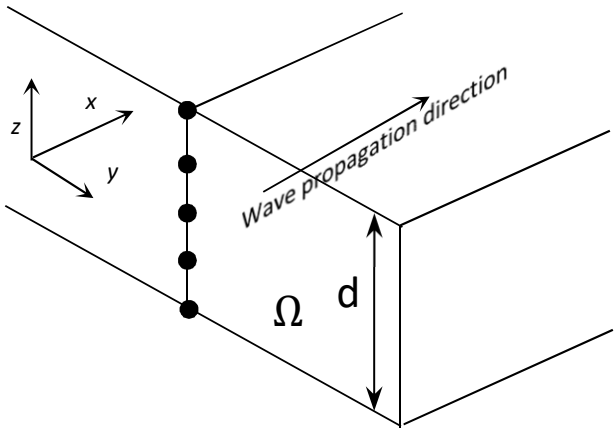

Fig. 5.1 Schematic representation of the plate.

$$\mathbf{u} = [u_x \quad u_z]^T, \sigma = [\sigma_x \quad \sigma_z \quad \sigma_{xz}]^T, \varepsilon = [\varepsilon_x \quad \varepsilon_z \quad \gamma_{xz}]^T. \tag{5.1}$$

The constitutive equation is expressed as follows:

$$\sigma = \mathbf{E}\varepsilon, \tag{5.2}$$

where, $\mathbf{E}$ is the elasticity matrix (real symmetric matrix for isotropic specimen) defined by the following equation:

$$\mathbf{E} = \frac{2G}{(1-2\nu)} \begin{bmatrix} 1-\nu & \nu & 0 \\ \nu & 1-\nu & 0 \\ 0 & 0 & (1-2\nu)/2 \end{bmatrix}, \tag{5.3}$$

where G is the shear modulus and ν the Poisson´s ratio. The strain-displacement relationship can be compactly written as follows:

$$\varepsilon = \mathbf{L}\mathbf{u}, \tag{5.4}$$

where $\mathbf{L}$ is a three-dimensional differential operator defined as Equation (5.5) for the plate

$$\mathbf{L} = \begin{bmatrix} \partial_x & 0 & \partial_z \\ 0 & \partial_z & \partial_x \end{bmatrix}^T. \tag{5.5}$$

Thus, the compatibility equations can be written as Equation (5.6):

$$\varepsilon = \left[\mathbf{L_x}\frac{\partial}{\partial x} + \mathbf{L_z}\frac{\partial}{\partial z}\right]^T u, \tag{5.6}$$

where

$$\mathbf{L_x} = \begin{bmatrix} 1 & 0 & 0 \\ 0 & 0 & 1 \end{bmatrix}^T, \qquad \mathbf{L_z} = \begin{bmatrix} 0 & 0 & 1 \\ 0 & 1 & 0 \end{bmatrix}^T. \tag{5.7}$$

5.2.1 Equations of motion

Cross-section waveguide dynamic is formulated using an energetic approach by inserting the kinetic and potential energies into Hamilton's equation. Although, energy balance must contain dissipative terms, in this analysis the conservative form of Hamilton's principle is used. The variation of the Hamiltonian of the waveguide, which vanishes at all material points, is

$$\delta H = \int_{t_1}^{t_2} \delta\left(\Phi - \mathbf{K}\right) dt = 0, \tag{5.8}$$

where Φ is the strain energy and K is the kinetic energy. The strain energy is given by

$$\Phi = \frac{1}{2}\int_V \varepsilon^{\mathbf{T}}\mathbf{C}\varepsilon dV, \tag{5.9}$$

where the upper script T means a transpose vector and V is the volume. The result of this equation represents the elastic energy transmitted by the excitation source and propagated along the waveguide via stress tensor. The kinetic energy is given by

$$K = \frac{1}{2}\int_V \dot{\mathbf{u}}^{\mathbf{T}}\rho\dot{\mathbf{u}}dV, \tag{5.10}$$

where ρ is the mass density and the dot represents a time derivative. By integrating by parts the kinetic term, Equation (5.8) can be written as

$$\int_{t_1}^{t_2} \left[\int_V \delta\left(\boldsymbol{\varepsilon}^{\mathbf{T}}\right) \mathbf{C}\boldsymbol{\varepsilon} dV + \int_V \delta\left(\mathbf{u}^{\mathbf{T}}\right) \rho \ddot{\mathbf{u}} dV \right] dt = 0. \tag{5.11}$$

5.2.2 Finite Element Scheme

The cross-sectional domain of the plate, Ω, can be represented by a system of mono-dimensional finite elements with domain Ω_e, due to the simplification attributed to the waveguide symmetry. The displacement expressions, discretized over the element domain, can be written in terms of the shape functions $N_i(z)$ and the nodal unknown displacements, (U_{xi}, U_{yi}, U_{zi}), in cartesian coordinates. Such shape functions are considered in this formulation as unidimensional, isoparametrics and quadratics.

$$u^e_{(x,z)}(x,z,t) = \left[\sum_i^k N_i(z) U_{(x,z)i} \right]^e e^{-i(\xi x - \omega t)} = \mathbf{N}(z) f^e e^{-i(\xi x - \omega t)}, \tag{5.12}$$

where

$$\mathbf{N}(z) = \begin{bmatrix} N_1 & 0 & N_2 & 0 & N_3 & 0 \\ 0 & N_1 & 0 & N_2 & 0 & N_3 \end{bmatrix} \qquad f^e = [U_{x1} \;\; U_{z1} \;\; U_{x2} \;\; U_{z2} \;\; U_{x3} \;\; U_{z3}]^T, \tag{5.13}$$

with $N_1 = \frac{\eta^2}{2} - \frac{\eta}{2}$, $N_2 = 1 - \eta^2$ and $N_3 = \frac{\eta^2}{2} + \frac{\eta}{2}$ represented in the local coordinates $\eta \in [-1, 1]$. Consequently, the Jacobian $|J|$ is equal to $l/2$, where l is the length of the element. For a maximum frequency of interest, the mesh criterion of [31] indicates the maximum element length, $L < 2\pi C_T / \beta \omega_{max}$, where C_T is the shear bulk wave velocity and β is 4 for the case of quadratic elements.

The strain vector in the element can be represented as a function of the nodal displacements:

$$\boldsymbol{\varepsilon}^e = (\mathbf{B_1} + i\xi \mathbf{B_2}) f^e e^{-i(\xi x - \omega t)}, \tag{5.14}$$

where $\mathbf{B}_1 = \mathbf{L_z}(\partial \mathbf{N}/\partial z)$, $\mathbf{B}_2 = \mathbf{L_x}\mathbf{N}$.

By considering adiabatic wave propagation, the weak form of the governing balance equation can be obtained by applying Hamilton's principle and adding up the contributions of every element as in the standard FE method. Indicating by n_{el} the total number of cross-sectional elements, the discrete form of the Hamilton formulation of Equation (5.11) becomes

$$\int_{t_1}^{t_2} \left\{ \bigcup_{e=1}^{N_{ele}} \left[\int_{V_e} \delta \left(\varepsilon^{(e)^T} \right) \mathbf{C} \varepsilon^{(e)} dV_e + \int_{V} \delta \left(\mathbf{u}^{\mathbf{T}} \right) \rho \ddot{\mathbf{u}} dV \right] \right\} dt = 0 \tag{5.15}$$

The substitution of Equation (5.14) into the strain energy term of Equation (5.15) with some manipulations produces

$$\begin{aligned} \int_{V_e} \delta \left(\varepsilon^{(e)^T} \right) \mathbf{C} \varepsilon^{(e)} dV_e &= \int_{\Omega_e} \delta \left[f^{(e)^T} \left(\mathbf{B}_1^T - i\xi \mathbf{B}_2^T \right) \right] \mathbf{C} \left(\mathbf{B}_1 - i\xi \mathbf{B}_2 \right) f^{(e)} d\Omega_e \\ &= \delta f^{(e)^T} \int_{\Omega_e} \left[\left(\mathbf{B}_1^T \mathbf{C} \mathbf{B}_1 - i\xi \mathbf{B}_2^T \mathbf{B}_1 + i\xi \mathbf{B}_1^T \mathbf{B}_2 + \xi^2 \mathbf{B}_2^T \mathbf{C} \mathbf{B}_2 \right) \right] f^{(e)} d\Omega_e \end{aligned} \tag{5.16}$$

As for the element kinetic energy contribution in Equation (5.15), by using the displacement expressions of Equation (5.12) and simplifying the harmonic terms $e^{i(\xi x - \omega t)}$ the following can be written

$$\int_{V_e} \delta \left(u^{(e)^T} \right) \rho \ddot{u}^{(e)} dV_e = -\omega^2 \delta f^{(e)^T} \int_{\Omega_e} \mathbf{N}^T \rho \mathbf{N} \mathrm{q}^{(e)} d\Omega_e \tag{5.17}$$

Substituting Equations (5.16-5.17) in Equation (5.15) yields:

$$\int_{t_1}^{t_2} \left\{ \bigcup_{e=1}^{N_{ele}} \delta f^{(e)^T} \left[\mathbf{K}_1{}^{(e)} + i\xi \mathbf{K}_2{}^{(e)} + \xi^2 \mathbf{K}_3{}^{(e)} - \omega^2 \mathbf{M}^{(e)} \right] f^{(e)} \right\} dt = 0 \tag{5.18}$$

The generalized SAFE governing equation for a stress-free structure is obtained as:

$$\left[\xi^2 \mathbf{K}_3 + i\xi \mathbf{K}_2 + \mathbf{K}_1 - \omega^2 \mathbf{M} \right] U = 0, \tag{5.19}$$

where

$$\mathbf{K}_1 = \sum_{e=1}^{N_{elem}} \int_{-1}^{1} \mathbf{B}_1^T \mathbf{C} \mathbf{B}_1 \left| J \right| d\eta, \tag{5.20}$$

$$\mathbf{K}_2 = \sum_{e=1}^{N_{elem}} \int_{-1}^{1} \mathbf{B}_1^T \mathbf{C} \mathbf{B}_2 \left| J \right| d\eta - \int_{-1}^{1} \mathbf{B}_2^T \mathbf{C} \mathbf{B}_1 \left| J \right| d\eta, \tag{5.21}$$

$$\mathbf{K}_3 = \sum_{e=1}^{N_{elem}} \int_{-1}^{1} \mathbf{B}_2^T \mathbf{C} \mathbf{B}_2 \left| J \right| d\eta, \tag{5.22}$$

$$\mathbf{M} = \sum_{e=1}^{N_{elem}} \int_{-1}^{1} \mathbf{N}^T \rho \mathbf{N} |J| \, d\eta, \tag{5.23}$$

where, $\mathbf{K}_1$,$\mathbf{K}_2$,$\mathbf{K}_3$ are the global stiffness matrices and M is the global mass matrix, superscript T denotes the matrix transpose, N_{elem} is the total number discretized elements across the waveguide thickness d and U is the vector of global displacements (and also the eigenvectors) at particular circular frequency ω.

The estimation of dispersion curves is tackled by sweeping the wave number ξ in a set of real values. Thus, the eigenfunction can be solved as a standard eigenvalue problem in $\omega(\xi)$. Real, purely imaginary and complex eigenvalues are obtained, however only the real one values (that correspond to the propagating waves) are considered. In this case, the number of eigenvalues $\omega(\xi)$ obtained is the number of total Degrees Of Freedom (DOF) of the system, N. Thus, N propagating modes (ξ_m, ω_m) are determined for each $\mathbf{U}_N$ cross sectional wave structure. The phase velocity of the propagating N mode can be computed by $C_p^m = \omega/\xi^m$, while the group velocity C_{gr}^m can be calculated using modal properties for conservatives materials and it is defined as follows:[49].

$$C_{gr}^m = \frac{\psi_L^m \mathbf{K}_{,\xi} \psi_R^m}{2\omega_m \psi_L^m \mathbf{M} \psi_R^m}, \tag{5.24}$$

where ψ_L^M and ψ_R^M are the m_{th} left and right eigenvectors of the eigenfunction, $\mathbf{K}_{,\xi}$ is $(2\xi\mathbf{K}_3 + \mathbf{K}_2)$ and $\mathbf{M}$ is the mass matrix.

5.3 Dispersion curves using EEC for a uniaxial stressed structures

As it has mentioned across this thesis, acoustoelasticity is a nonlinear phenomenon that explains velocity changes in bulk waves (longitudinal and shear) as a function of applied stress, based on the continuum theory for small disturbances. The linearization of the relation between stress and strain is no longer valid for the case of ultrasound propagation in a media subject to stress and with finite deformations [37].

For the linear case, only the second order elastic constants λ and μ are needed as parameters to describe the linear constitutive relation stress-strain in an isotropic medium. However, for nonlinear characterization, additional Third Order Elastic Constants (TOECs) have to be added to the constitutive relation.

Stress tensors can be defined relative to different configurations. The Cauchy stress tensor, for example, describes the stresses relative to the present configuration while the Kirchhoff (or the second Piola-Kirchhoff) stress tensor T_{ij} describes the stresses relative to some reference configuration, in our case with respect to a Lagrangian frame which contains the finite deformation.

So, the relation between strain energy function U, and stress is used to express the nonlinear relation between stress-strain, where this function is expressed as a power series in strains as follows [35]:

$$U = C^{(2)}_{ijkl}E_{ij}E_{kl} + C^{(3)}_{ijklmn}E_{ij}E_{kl}E_{mn} + \ldots, \tag{5.25}$$

where E is the Lagrangian strain tensor and $C^{(2)}, C^{(3)}, ..$ are increasing order tensors and correspond to the coefficient of the power series expansion. The stresses are related to the strain energy

$$T_{ij} = \frac{\partial U}{\partial E_{ij}}, \tag{5.26}$$

where T_{ij} is the second Piola-Kirchhoff stress tensor, combining Equation (5.25) and Equation (5.26) yields the non-linear stress-strain relation :

$$T_{ij} = C^{(2)}_{ijkl}E_{kl} + C^{(3)}_{ijklmn}E_{kl}E_{mn} + \ldots. \tag{5.27}$$

As mentioned before, $C^{(2)}_{ijkl}$ is the second order constants for the linear case, and $C^{(3)}_{ijklmn}$ represents the third order elastic constants, for the case of isotropic materials. Henceforth, the second Piola-Kirchhoff stress tensor produces the suitable stress-strain relation to describe the wave propagation in a stressed waveguide.

T_{ij} can be represented in terms of the Murnaghan constants l, m and n [84]. The T_{ij} tensor is the foundation of the EEC to tackle the influence of the acoustoelasticity in the propagation of guided waves [11, 28, 35]. The definition of the EEC tensor results of the equation of motion for incremental displacement. Following the derivation of [37],[28] and referring to Figure 5.2, three deformation states are defined. Following the notation used by [28], the unstressed frame is called the "natural state." The position of a material point is given by the position vector x whose "natural coordinates" are $x(x_1, x_2, x_3,)$. "The initial state" is a finite deformation (applied or residual) in static equilibrium is then given by the position vector $\bar{x}$, whose initial coordinates are $\overline{x}(\overline{x_1}, \overline{x_2}, \overline{x_3})$. Finally, when a dynamic perturbation (wave propagation) is applied at the initial state, the point material reach the third state called the "final state". The position of the material point is then defined by the position vector $\tilde{x}$ whose "final coordinates" are $\tilde{x}(\tilde{x}_1, \tilde{x}_2, \tilde{x}_3)$. A common Cartesian frame (ξ_1, ξ_2, ξ_3) is used to refer

to the position of material points of any of the three states. Deformation between different states i.e. natural to initial, natural to final and initial to final, are given by u_i, u_f and u as follows:

$$\begin{aligned} u_i(\xi) &= \bar{x} - x, \\ u_f(\xi, t) &= \widetilde{x} - x, \\ u(\xi, t) &= \widetilde{x} - \bar{x}. \end{aligned} \tag{5.28}$$

The procedure to determine the equation of motion for the incremental displacement is widely explained by [37]. Here, it is only described the steps to establish this relation and the final result. First the incremental strain tensor in a Lagrangian frame is obtained subtracting initial and final strain tensor. This incremental strain tensor is related to the Second Piola-Kirchoff stress tensor via constitutive equation yields the incremental stress tensor in terms of the second and third order elastic constants, as noted above. Subtracting the equation of static equilibrium (pre-deformation) and the equation of motion for the final state, the equation of motion for the incremental displacement is obtained. The final equation in tensor notation is expressed as follows:

$$A_{ijkl} \frac{\partial^2 u_k}{\partial x_j \partial x_l} = \rho^0 \ddot{u}_i, \tag{5.29}$$

where u is the incremental displacement of the material particle (that is, the displacement due to the wave motion only), ρ^0 is the density of the unstressed material and A_{ijkl} is a tensor that depends on the symmetry of the material and describes the relation between second and third order elastic constants and the strains. The coefficients of A_{ijkl} are the summation of 4^{th} order stiffness tensor plus the infinitesimal strain tensor associated with the initial strains (those due to the applied stresses). In [35], based on the analysis of A_{ijkl}, it is stated that variations of the wave velocity depend on the initial stress value and the initial displacement gradient $\partial u_i / \partial \xi$. So, for the case of stress-free wave motion the equation of motion is given by,

$$C_{ijkl} \frac{\partial^2 u_k}{\partial x_j \partial x_l} = \rho^0 \ddot{u}_i, \tag{5.30}$$

where C_{ijkl} is the stiffness tensor of second order. Comparing the equation of motion for incremental displacement in natural coordinates, Equation (5.29), with the equation of motion relative to a stress-free medium, Equation (5.30), it is found that they are equivalent. The similarity between these equations allows treating a stressed material as an unstressed material with a new stiffness tensor (C^a_{ijkl}). This new tensor considers the disturbances related to the presence of stress [28]. This description regards the following formalism:

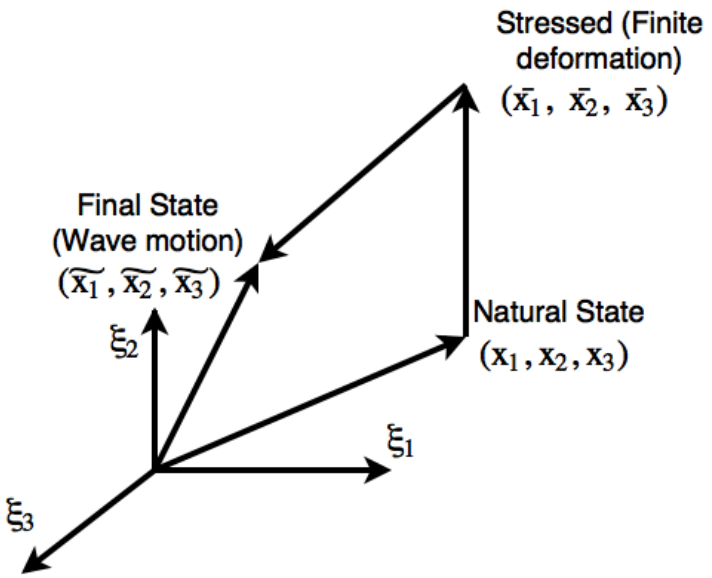

Fig. 5.2 Coordinates of a material point at natural (x), initial ($\bar{x}$) and final ($\tilde{x}$) configuration of a predeformed body [28]

$$C^a_{ijkl} = C_{ijkl} + \delta C_{ijkl}, \tag{5.31}$$

where, C^a_{ijkl} is the tensor which contains the EEC, C_{ijkl} is the tensor of the second order elastic constants for a stress-free material and δC_{ijkl} is the disturbance related to the presence of applied or residual stress. Thus, the particular symmetry of second-order elastic constants (C_{ijkl}=C_{jlik}) is no longer valid for C^a_{ijkl}. Since, EEC allows the use of the second order approach to describe the guided wave propagation in the case of stressed materials or, in other words, the wave propagation in a stressed specimen can be considered as a the wave propagation in a stress-free material presenting a stiffness matrix different from those of an unstressed material.

In bulk waves analysis, the Christoffel equation provides a set of eigenequations whose eigenvector defining the wave polarization direction. Now, an interesting conclusion of using the Christoffel equation in the acoustoelasticity frame can be obtained by comparing the eigenequation in the two scenarios, i.e. The eigenfunction which satisfy the guided wave modal propagation $u_i = U_i e^{i(\xi \eta_j \eta_j - \omega t)}$, where ξ is the wavenumber, η_j is the propagation unit vector, can be written for the stress-free propagation as presented by Equation (5.32) and for the stressed propagation as shown in Equation (5.33) follows:

$$\left(C_{ijkl}\eta_k\eta_l - v^2\delta_{il}\right)U_l = 0, \tag{5.32}$$

$$\left(C^a_{ijkl}\eta_k\eta_l - v^2\delta_{il}\right)U_l = 0, \tag{5.33}$$

where v corresponds to the ultrasonic wave phase velocity, $\eta_k\eta_l$ are the direction cosines of the normal to the wavefront and $U_i = U_l\delta_{il}$, where δ is the Kronecker delta. Comparing the Equations (5.32 and 5.33), it can be concluded a new symmetry with respect to ultrasonic wave propagation emerge due to a different stiffness tensor in the Christoffel equation. As it should be inferred the velocity behavior will be different in direction of the externally applied stress compared with other directions. Finally, the C^a_{ijkl} terms proposed by [28] are listed in appendix A of this thesis.

5.4 Numerical validation

In order to validate the proposed approach, dispersion curves obtained by [35] for an aluminum isotropic plate ($\rho = 2800kg/m^3$) of thickness $d = 6.35$ mm with material constants in GPa, $l = -252.2; m = -324.9; n = -351.2; \lambda = 54.9; \mu = 26.5$, were used. It is a benchmark data from an analytical model based on the acoustoelasticity principle and the Christoffel equation. Figure 5.3 illustrates the used plate Cartesian frames, while Figure 5.4 shows the dependence of phase velocity on the direction of propagation, by comparing the S_1 modes about 600 kHz, propagating at varying angles with respect to the x_1'. Herein, analytical solution by [35] is represented by solid lines while the proposed approach by markers.

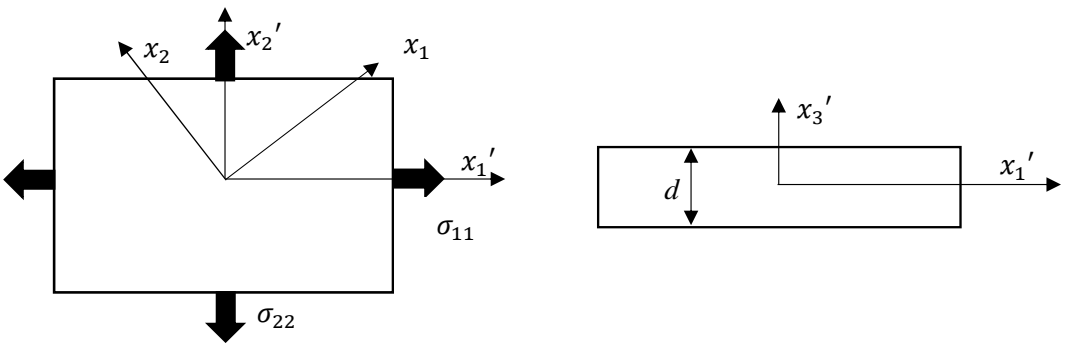

Fig. 5.3 Plate's Cartesian frames.

Figure 5.5 presents the dispersion curves for the S_1 mode about 600 kHz by applying different stresses values in order to observe the variations of phase velocity respect to the applied load, where all curves are at an angle of $\phi = 45°$. Moreover, Figure 5.5 presents the deviation of S_1 mode between the proposed scheme and the previous analytical solution in the case of different applied stresses.

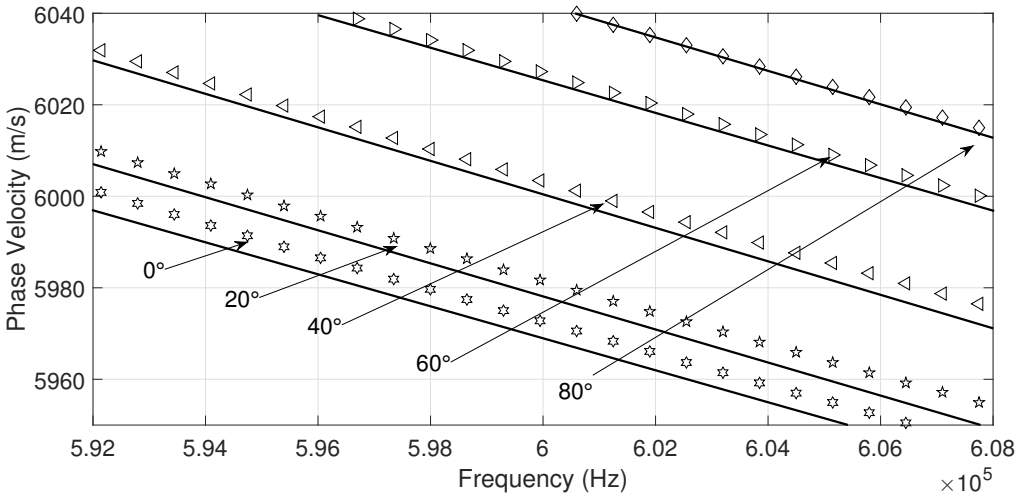

Fig. 5.4 Comparison of angle dependence of S_1 mode for an uniaxial load of 120 MPa.

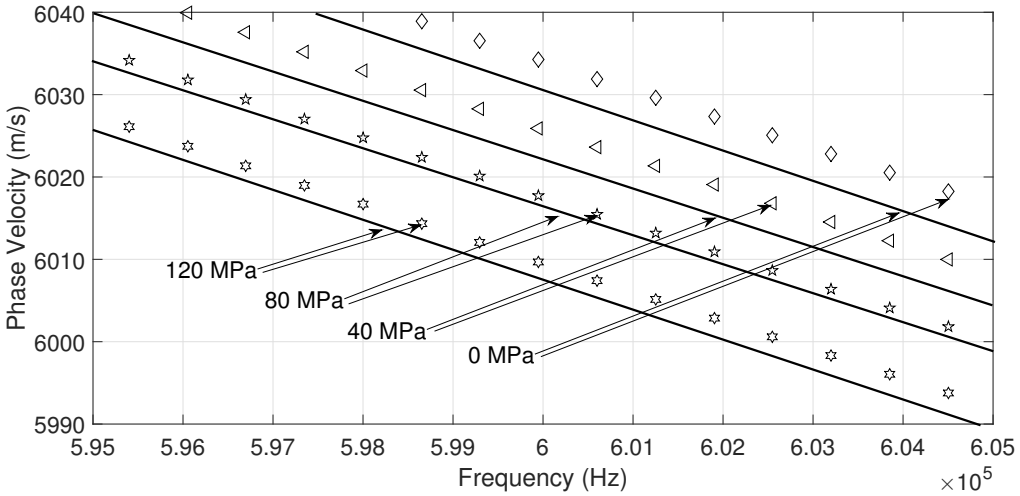

Fig. 5.5 Comparison of stress dependence of S_1 mode for an uniaxial load at $\phi = 45°$. Analytical solution by [35] is represented by solid lines while the proposed approach by markers

As stated by [35] and corroborated in the estimated dispersion curves using the approach proposed, when different wave modes are propagating in the stressed specimen, they could have different phase velocity variation with respect to stress-free condition at the same frequency. Thus, a different wave pattern is expected instead of the same pattern in different time trace.

According to Figure 5.4, the dispersion curves of S_1 mode (represented by markers) computed by means of EEC approach, for a load of $\sigma_{11} = 120$ MPa, are close to the analytical solution proposed by [35]. However, this should not be generalized since the deviation of EECs from the theoretical model depends on the mode and frequency range under consideration [35].

In the case of the stress dependence Figure 5.5, it can be observed a good agreement in the range of analyzed dispersion curves between analytical model based on anisotropy, and combined EEC´s and SAFE proposed model.

5.5 Discussion

As a conclusion, an approximate method for computing dispersion curves of guided waves, phase and group velocity, in homogeneous, prismatic and isotropic specimens under stress based on SAFE and EEC is proposed in this chapter. The main contribution of the proposed approach is accounting for the presence of stress in the waveguide by using EEC as stiffness matrix in a SAFE scheme.

The proposed methodology was validated for a plate on several propagation angles at constant load in order to verify the influence of the direction of the applied load in the variation of the velocity in a different direction. Finally, it is studied the behavior of the phase velocity at different load conditions, for the same propagation angle. All the information is gathered and a good agreement is obtained with the published results of [35].

Chapter 6

Support stiffness monitoring in cylindrical structures

6.1 Introduction

This chapter is devoted to propose a support stiffness monitoring scheme, based on the wave field interaction of the fundamental torsional mode with a support with different stiffnesses. The main motivation of this study was to develop a monitoring tool capable of detecting stiffness loss in pipelines supports, allowing corrective actions to prevent the presence of large mechanical stresses in pipelines avoiding a risky condition for persons and facilities. The capability of early detection of support stiffness loss can improve the integrity management of pipelines and consequently provides safe conditions, assures an effective maintenance and an economic benefit.

Supports integrity inspection presents several challenges, e.g. mechanical stress variations are produced along the pipeline when the support loads are changing. Therefore, any suitable support monitoring scheme should be focused on determining the variation of the axial stress condition in the pipe or any other feature that revels varying load conditions in the supports since load variations measurement in the support itself is difficult, impractical and often prohibitively expensive. Additionally, this abnormal condition can appear suddenly as result of terrain movements or soil weakening by variations in the soil's water content.

Among the suitable techniques to evaluate supports integrity i.e. cracks [96], corrosion [4], contact loads [19, 33], the ultrasonic based is gaining attention. The successful of detecting abnormal load condition at support spots relies on the capability to discriminate the variation of the ultrasonic guided wavepacket between the support on a normal load condition (even in presence of discontinuities i.e. corrosion or notch reflected signals) and in

abnormal condition (lack of rigidity foundation in the support). Consequently, it is essential to estimate changes influence in the support load condition in the guided wave; few works have been reported on this subject. The effect of clamped supports on the propagation of the torsional mode $T(0,1)$ is studied in [19] by means of simulation and experiments. The focus of this study was the attenuation caused by the presence of rubber gaskets in the support and its consequences on the detectability of discontinuities located after the support. Moreover, a growth of the reflection produced by the support is found, as the tightness of the clamp support increase, for the $T(0,1)$ mode. In [112] and [113], the interaction of the torsional mode $T(0,1)$ with a longitudinal welded support in a pipe is modeled using FEM. Energy leakage from the pipe to the support via transmission and mode conversion are detected. The mode $T(0,1)$ is used in [114] to evaluate the effect of a longitudinal support welded on the wavepacket propagation in a pipe using both simulation and experimental methods. It is determined that reflected signals by the longitudinal welded support are much greater than reflections from other discontinuities beyond the support.

The interaction of the fundamental torsional mode with simple supports is studied by experimental tests and analytical methods, finite elements and Semi-Analytical Finite Elements (SAFE) [33]. A SAFE analysis establishes which modes can propagate in a stress-free pipe. They concluded that exist a mode conversion from $T(0,1)$ into a suitable mode which is propagated along that supported section. The reflection coefficient for the support will be then high where there is no mode similarity to $T(0,1)$ in the region around the support.

As mentioned above, variations of the normal stress in pipelines can be attributed to the changes in the supports load conditions. Therefore, tracking stress variations along the pipe in a region close to the support should provide information of the support integrity. Presence of stress in the structure affects damage localization in the case of using methods that utilize elastic wave propagation. Wave propagation velocity decreases with increasing stress [87]. The study of the guided wave propagation in stressed specimens is mainly based on the acoustoelasticity effect (stress dependence of acoustic bulk wave velocities i.e. shear and longitudinal velocities). The foundation of the acoustoelasticity theory can be endorsed to the Murnaghan [84] and Hughes and Kelly [57] works in the middle part of the last century. Since, part of the research has been aimed to the determination of the acoustoelastic guided wave dispersion curves [36, 71, 69]; others are devoted to determine the load condition or the residual stress of the specimen based on the velocity change of the guided waves[18, 97, 85, 14, 117]. On the other hand, an investigation of wave propagation in double cylindrical rods based on Hertz contact theory and considering the effect of prestressing found that at low frequencies, group velocity of torsional-like modes

are very sensitive to the variation of prestress [65]. In [26] the effect of stress applied perpendicular to the propagation-direction on guided wave propagation is accounted for through nonlinear elasticity and finite deformation theory (Acoustoelasticity). Emphasis is placed on the stress dependence of the energy velocity of the S_0 lamb modes. For this purpose, an expression for the energy velocity of leaky Lamb waves in a stressed plate is derived. It has been investigated by [106] the transfer of energy inside a multi-wire cable with a SAFE method. An energy transfer parameter has been proposed in order to determine the power flow distribution inside the cable and the exchange of energy between wires. Based on this parameter, a new compressional mode excited with an axial excitation of the central wire mainly localized inside the central wire has been found. Finally, some specific engineering applications such as bolted structural connections, grouted tendons and steel stands, have been object to monitoring using the acoustoelasticity effect of guided waves[110, 8, 15, 23].

In summary, previous research works have been focused on the study the influence of the support material changes (cracks, pinholes, corrosion, contact loads) in the guided wave propagation and how the presence of the support in the propagation path affects the detection of material discontinuities in the waveguide under investigation. The work presented here is focused specifically on formulate a methodology to monitoring changes in the load condition in the support. To do that, it is needed an understanding of how the mode $T(0,1)$ interacts with simple supports under varying support load conditions. Experimental and numerical tests reveal a greater effect of the energy leakage instead of velocity changes as a result of the Acoustoelasticity effect.

6.2 Axisymmetric torsional guided waves propagating in cylindrical waveguides

In order to develop an axisymmetric wave propagation model for torsional guided waves, certain assumptions are needed. The model assumes that the cylindrical system is geometrically axisymmetric, infinitely long, stress-free in the boundaries for some specific directions and surrounded of vacuum. The material is elastic, homogeneous and isotropic (Its mechanical and thermal properties are the same in all directions). The waves will be assumed to be continuous, the frequency real (transients effects are no considered), and the energy is finite and constant. The solutions to motion equation will only be sought explored for guided waves, which are propagated axially.

Three guided waves modes can be developed in cylindrical systems: longitudinal (L), flexural (F) and torsional (T). Although the formers (L and F) are widely used in Structural

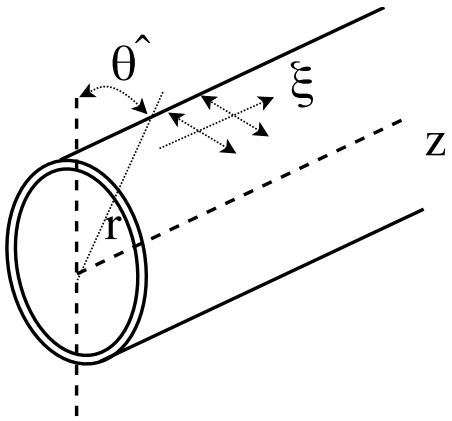

Fig. 6.1 Schematic representation of the cylindrical waveguide.

Health Monitoring (SHM) applications, they are strongly affected by an acoustic coupling between these modes and the surroundings. On the contrary, the latter does not.

The torsional modes are characterized mainly by a displacement primarily in the θ-direction. The axisymmetric torsional mode corresponds to an uniform azimuthal displacement in θ-direction (angular displacement) of the entire cylindrical waveguide; the higher order torsional modes exhibit a more complicated behavior. However, the angular displacement is not constant through the radius of the cylinder. Different locations through the radius of the cylinder can twist in different directions and nulls of displacement can exist. Figure 2 depicts cylindrical θ and z directions.

The guided waves propagation model is based on the combination of Euler's equation of motion and the generalized Hooke's law. Both relations yield the Navier's displacement equation of motion as follows:

$$(\lambda + 2\mu)\nabla(\nabla \cdot u) + \mu\nabla \times (\nabla \times u) = \rho\left(\frac{\partial^2 u}{\partial t^2}\right), \tag{6.1}$$

where u is the displacement vector, ρ is the mass density per unit volume and λ, μ are the Lame's constants. The resulting Navier's equations constitute a system of three partial differential equations of second-order, where $(\lambda + 2\mu)\nabla(\nabla \cdot u)$ considers the dilatation (compressional) portion and, $\mu\nabla \times (\nabla \times u)$ the rotational (equivoluminal) portion of the model. These two terms are decoupled and individually belong to a wave equation of the scalar field Φ and the H vector field as follows

$$C_1\nabla^2\Phi = \frac{\partial^2\Phi}{\partial t^2}, \tag{6.2}$$

$$C_2 \nabla^2 H = \frac{\partial^2 H}{\partial t^2}, \tag{6.3}$$

where C_1 and C_2 are the longitudinal and shear bulk velocities respectively. Since Equation (6.1) is separable in cylindrical coordinates, the solution may be divided into the product of functions of each one of the spatial dimensions in cylindrical coordinates as:

$$\Phi, H = \Gamma_{\Phi,H}(r)\,\Gamma_{\Phi,H}(\theta)\,\Gamma_{\Phi,H}(z)\,e^{i(kr-\omega t)}, \tag{6.4}$$

where k is the wavenumber vector, and $\Gamma_{\Phi,H}(r)$, $\Gamma_{\Phi,H}(\theta)$, and $\Gamma_{\Phi,H}(z)$ describe the field variation in each spatial coordinate. Assuming that the wave does not propagate in the radial direction (r) and that the displacement field does not vary in the θ-direction either z-direction except for the harmonic oscillation described by the wavenumber as follows

$$\Phi, H = \Gamma_{\Phi,H}(r)\,e^{ip\theta}\,e^{i(\xi z-\omega t)}, \tag{6.5}$$

where ξ is the component of the complex vector wavenumber in the z-direction, p is referred to as the circumferential order; which must be a whole number, since only propagation in the direction of the axis of the cylinder is considered and the field variables must be continuous in the angular direction. Recalling from Equation (6.1) and Hooke's law, the field variables such as displacements and stresses can be expressed in terms of potential functions, which can be numerically solved (see [95, Viola and Marzani, 6, 46] for more details on this subject).

On the other hand, the family of torsional modes results when only the u_θ displacement is assumed to exist $(u_r, u_z = 0)$. Such a displacement field is obtained only if rotational potential function in z, $h_z \neq 0$. Then, for sake of brevity, only the expressions for u_θ, h_z, and the stress ($\sigma_{r\theta}$ as boundary condition), are used in forward to study the axisymmetric torsional modes as follows [46].

$$h_z(r) = C_1 J_p(\beta r), \tag{6.6}$$

$$u_\theta = h_{z'}(r)\cos(p\theta)\,e^{i(\xi z-\omega t)}, \tag{6.7}$$

$$\sigma_{r\theta} = \mu\left[-\left(2h_{z''} - \beta^2 h_z\right)\right], \tag{6.8}$$

$$\beta^2 = \frac{\omega^2}{C_2^2} - \xi^2, \tag{6.9}$$

where J_p is the Bessel function of the first kind an order p, r is the cylinder radius, and C_1 is a constant. The family of Bessel functions J_p represent standing waves. For the case of the axisymmetric modes, p=0, and by using the property of Bessel functions J_0' $(x) = -J_1(x)$,

the corresponding u_θ can be expressed as follows.

$$u_\theta = -\frac{\partial h_z}{\partial r} = (C_1\beta)\, J_1(\beta r)\, e^{i(\xi z-\omega t)}. \tag{6.10}$$

The frequency equation for the torsional modes may be obtained by using the boundary condition $\sigma_{r\theta}|_{r_{ext}} = 0$, for the studied case only $\sigma_{zz} \neq 0$, in this way

$$\left[\beta^2 a^2 J_0(\beta a) - 2\beta a J_1(\beta a)\right] - \left[\beta^2 b^2 J_0(\beta b) - 2\beta b J_1(\beta b)\right] = 0. \tag{6.11}$$

Noting that this equation belongs to the dispersion equation for the torsional waves propagating in the axial direction of a cylinder of inner and outer radius a and b respectively. The lowest axisymmetric torsional mode, the first root of Equation (6.11), is $\beta = 0$, in which involves the rotation of each transverse section of the cylinder as a whole about its center, is not adequately described by the Bessel equations [5]. This mode corresponds to the zero order torsional modes -$T(0,1)$- and, therefore from Equation (6.9), and considering $\beta = 0$ it is obtained that

$$\omega = \xi C_2. \tag{6.12}$$

Considering the previous result and the phase velocity definition, let state the following relation:

$$V_p = \frac{\omega}{\xi} = C_2. \tag{6.13}$$

The last expression shows that $T(0,1)$ propagates at a constant phase velocity equivalent to the bulk shear velocity of the material. The $T(0,1)$ mode is preferred in pipeline monitoring for two main reasons: (i) it propagates non-dispersively at the shear velocity of the medium and, (ii) since the fluid layers do not support shear waves, the $T(0,1)$ propagates solely in the steel wall of the pipe with no energy leakage to the fluid and no attenuation. On the other hand, The zero order torsional modes can be expressed analytically in a similar fashion as the '*SH*' modes in a plate.

6.3 Experimental Setup

The pipe test bench described in Section (4.2) is again used in this chapter. Variations in the support's loading will produce an increment in the normal stress along the pipe. This test mock up is implemented to emulate a failure or a change in the loading support conditions. In the proposed methodology, a scheme of two magnetostrictive collars in a pitch-catch configuration is adopted to produce the $T(0,1)$ torsional mode.

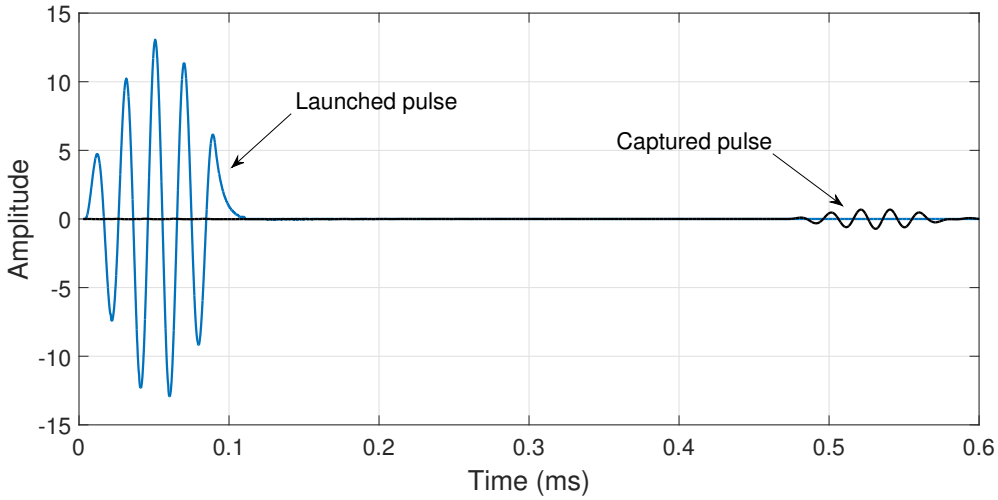

Fig. 6.2 Launched and captured $T(0,1)$ pulses

The waveguides are excited with a sinusoidal pulse of 5 cycles Gaussian-modulated at 32 kHz via magnetostrictive actuator (see Figure 6.2). The magnetostrictive actuator is composed by two elements wrapped around the pipe; a thin FeCo alloy strip (adhered to the pipe by epoxy) to yield a circumferential magnetic field and, an electromagnetic coil with an alternate current flowing in circumferential direction used to produce an axial magnetic field. The combined action produces a helicoidally strain pulse along the pipe. Therefore, torsional guided waves are generated by axisymmetric surface loading. In order to launch only the $T(0,1)$ mode, a tunning process is performed through an appropriate selection of the excitation frequency and wide of the strip (See Figure 6.3). The torsional guided wave propagates along the pipe and it is captured 1.5 m. ahead of the actuator with a magnetostrictive sensor. As it is expected, the velocity of propagation was very close to the shear velocity for the material of the pipe 3200 m/s). No other modes were detected in the tests. A picoscope 2208 is used as DAQ system.

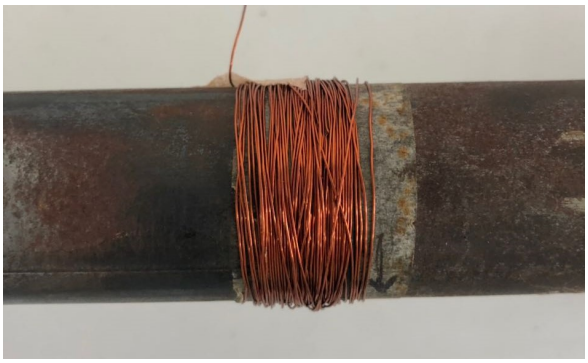

Fig. 6.3 Magnetostrictive transducer used in the experimentation

The experiments were conducted in such a way that it replicates a common real pipe under a simplified loading and support conditions. Variations in the stiffness are emulated by changing the magnitude of the variable support. First the nominal condition is determined considering the absence of deflection with respect to the vertical (g-direction) in the middle variable support. Under this condition the middle part of the pipe ($L/2$) is experimenting a negative bending moment and the pipe develops an internal stress of around 5% of the yield strength, under this scenario the load in Newtons between support and pipe is 92.2 N (reference stiffness). The magnitude of the load applied for the variable support to the pipe is decreasing for $D_1 - D_4$ scenarios for deflections in gravity direction and is increasing for $D_6 - D_9$ in opposite direction. In this way, D_1 belongs to a deflection of 10 mm downwards (74.1 N), D_2 to 20 mm (57.03 N), D_3 to 30 mm (39.46 N) and D_4 to 40 mm (21.9 N). Similarly, D_6 belongs to 10 mm upwards (109.75 N), D_7 to 20 mm (127.3 N), D_8 to 30 mm (143.9 N) and D_9 to 40 mm (160 N). The test are configured in such way that the stresses correspond to an incipient strength condition ($< 30\%$ of yields strength). The variation of the deflection yields an increase in the magnitude of the bending moment in the middle part of the pipeline, as shown in Figure 6.4.

Figure 6.4 provides an estimation of the normal stresses along the pipe ($z - direction$), expressed in terms of percentage of yield strength, generated by bending. The maximum bending stress in a cross-section for a specific position along the pipe axis is located at the outer distance (the exterior radius) which means the pipe's surface is the area under highest stress.

So, as shown in Figure 6.4, changes in the supports reaction will produce a distributed normal stress response along the path of propagation. In fact, the longitudinal normal stress varies from point to point along the pipe's axis, and linearly with the radius, passing from tension to compression in the neutral axis or cylinders center; reaching a maximum normal stress value at the outmost distance from neutral axis or external radio. As shown in Figure

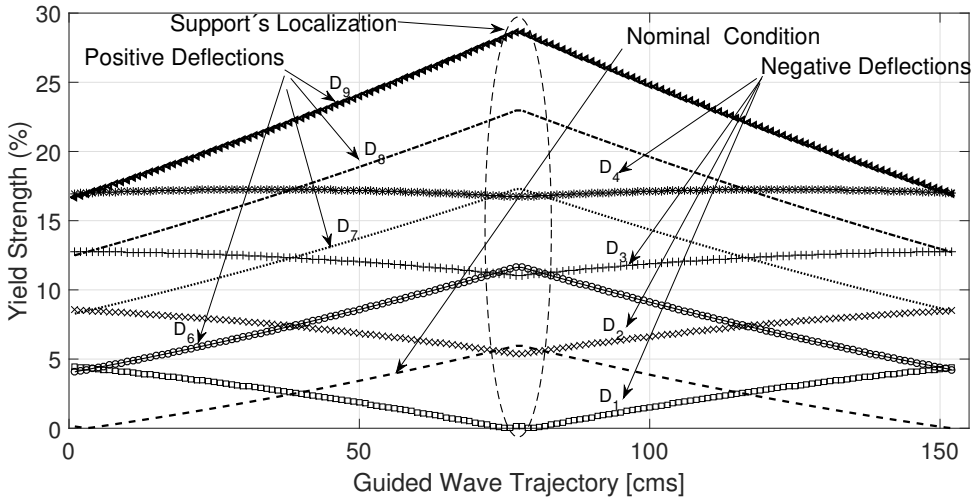

Fig. 6.4 Stress variation along the pipe subject to different reaction forces in the support

6.5, the wave structure obtained by using the GUIGUW software [9], the maximum azimuthal displacement component of the torsional wave expressed in the wave structure matches the maximum azimuthal axial stress obtained in pipes cross-section. Changes from tension to compression in a specific cross section in the cylinder must produce variations of phase velocity of $T(0,1)$ in the same plane. Therefore, different phase velocities around of V_0 for the same cross-section may result when the torsional mode is propagating in a bending pipe. On the other hand, variations in the guided waves velocities can also be attributed to a thickness reduction of the waveguide produced by corrosion or erosion. Nevertheless, these discontinuities slowly appear in the waveguide in a much greater time scale compared to the most probable scenario of unexpected change in the supports reaction. Therefore, any suddenly change in the TOF of the wave can be interpreted as a modification in the stress condition in the waveguide.

6.4 Experimental Results

This section provides the results of the experiments carried out under the conditions described above. One hundred tests were conducted by each scenario and the propagated torsional wave were captured. As an example, in Figure 6.6 it is shown one of the captured signals for the scenarios D_3 and D_1.

Contrary, to the expressed by the acoustoelasticity effect, variations in the pipe's stress are not enough to produce any significant change in the TOF of the torsional guided wave under the test experimental conditions, not even the material elongation effect is observed.

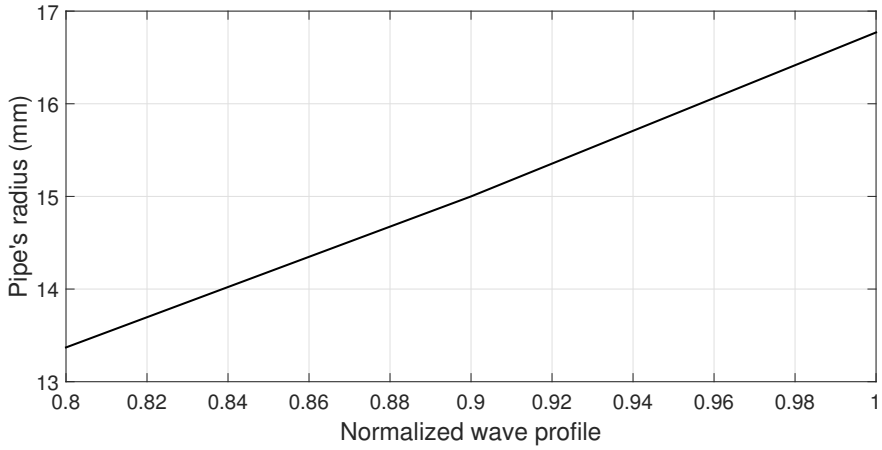

Fig. 6.5 Sample wave structure of U_θ for $T(0,1)$ at 32 kHz in a 1" sch. 40 pipe.

Considering the DAQ sampling frequency (18 MHz), the frequency of the signal (32 KHz) and the velocity of the torsional wave (around 3200 m/s), the minimal change of velocity that can be detected is 0.38 m/s (without considering noise), which represent a capability to detect phase velocity variations around of 0.012%. The inability for detecting $\Delta(TOF)$ may be attributed to the phase velocity in a specific pipe cross-section for a bending pipe is radius dependent due to the linear stress distribution in r, going from tension to compression or vice versa at the same cross section, i.e. the magnetostrictive sensor is capturing at the same time, torsional waves propagating at different phase velocities, in the case of tension stresses $V_\sigma < V_0$ and $V_\sigma > V_0$ for compression stresses.

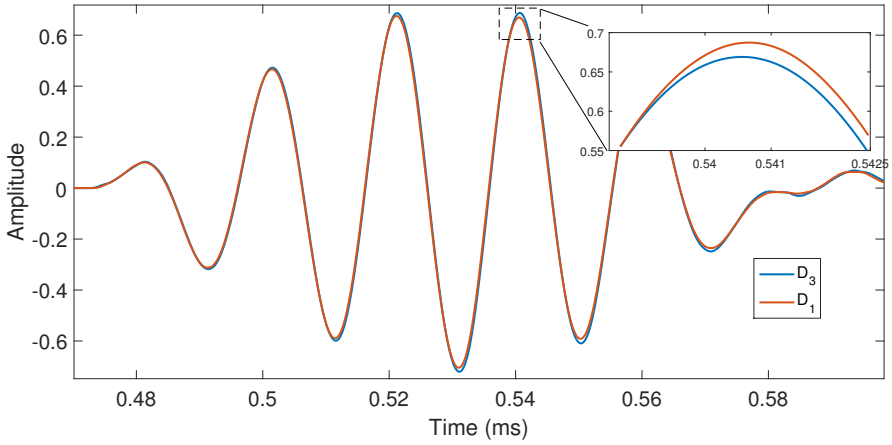

Fig. 6.6 Captured fundamental torsional signals for D3 and D1

On the other hand, as it is expected, no dispersion is observed in the captured torsional wave. So, only amplitude changes are observed in the wavepackets when they are compared

in time domain. The variations in the wave amplitude, which can be interpreted as energy variations, could be attributed to the fact that the interaction between the torsional guided wave and the support has been altered. Although the experimental tests reveals tiny amplitude changes in the captured signal, the abnormal condition to be monitored, a decrease of the support stiffness, produces an anomalous behavior in the guided wave, i.e. an increase of the transmitted pulse magnitude.

In order to create a feature associated to the amplitude variation of the captured signal as a result of the acoustic coupling between pipe and support, an auto correlation of the incident signal, r_{xx}, and a cross correlation between the current sensed signal $S_1(t)$ and the incident signals $S_0(t)$, r_{xy}, are used instead of the raw signals to produce a relation between both signals. Autocorrelation and cross correlation are calculated as follows:

$$r_{xx}(n) = \frac{1}{N}\sum_{n=0}^{N} S_0(n)S_0(n-t), \tag{6.14}$$

$$r_{xy}(n) = \frac{1}{N}\sum_{n=0}^{N} S_0(n)S_i(n-t), \tag{6.15}$$

where N is the number of signal samples, t is defined in the interval $(-N*T_s,(N-1)*T_s)$. Then, the Root Mean Square Deviation (RMSD) is

calculated as:

$$RMSD = \sqrt{\frac{\sum_{i=1}^{N}(G_i - ref)^2}{N}}, \tag{6.16}$$

where G_i is a scalar calculated using the peak values of the correlated signals:

$$G_i = \frac{max(r_{xy})}{max(r_{xx})}. \tag{6.17}$$

G_i denotes the peak value of the current scenario, ref is the peak value of the averaged signal (100 experiments) at nominal condition, (no deflection in the pipe at the center). Since only magnitude changes are expected in this monitoring scheme, $RMSD$ is proposed to evaluate the supports rigidity. In Figure 6.7, it can be seen the RMSD values for the different scenarios. Now, ten runs were averaged and presented in Figure 6.8 and finally, Figure 6.9 presents the relation between force and RMSD for the different cases.

Although D_6 to D_9 are improbable scenarios in a real installation, deflection opposite to the gravity, here, they are used to determine in a wide perspective how the torsional guided wave interacts with the reaction force exerted by the simple support. Variations in α are the

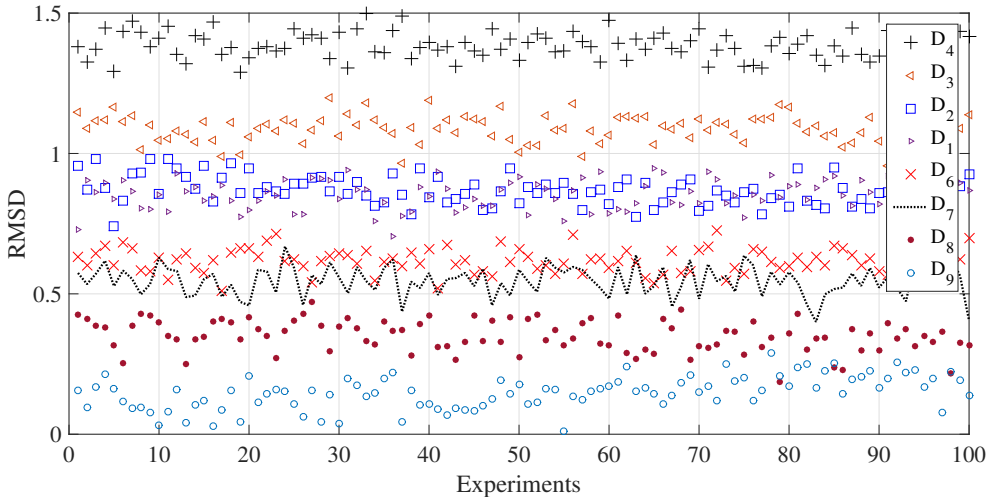

Fig. 6.7 RMSD for the studied scenarios

result of change in the contact conditions or the magnitude of the supports force. Clearly, as the magnitude of the supports reaction decrease, the amplitude of the wave captured by the sensor increase. This result can be explained from an energy perspective, in which, a reduction of the force between the pipe and the support produce a decrease of the transmitted energy to the supports material and therefore, a greater wave refraction.

6.5 Finite Element modeling analysis

Considering the previous results: a very small acoustoelastic effect and a change in the amplitude of the wave, in the following numerical analysis it is investigated the support influence in the pipe, $T(0,1)$ propagation by means of FEM simulations. This analysis has been restricted to the transmission of ultrasound energy to the support. Thus, the FEM does not pretend the estimate the actual change of the magnitude of the transmitted pulse, its only aim is to observe the relation between reaction force and SH_0 generation. A mode conversion of $T(0,1)$ transmitted through the support, modeled as a plate, is expected because the tangential nature of the $T(0,1)$ and the mechanical coupling between the pipe (cylinder) and the simple support (plate). are adopted.

Since surfaces between pipe and support are rough, a contact interface can be assumed as a series of parts in contact and voids. Due to the high acoustic impedance of the air, voids act as reflectors for the ultrasonic waves. Thus, an increase of force will result in a reduction of the number and size of these voids and, at the same time, an increase of the ultrasound energy transmitted through the interface. When two surfaces of the same material are in contact,

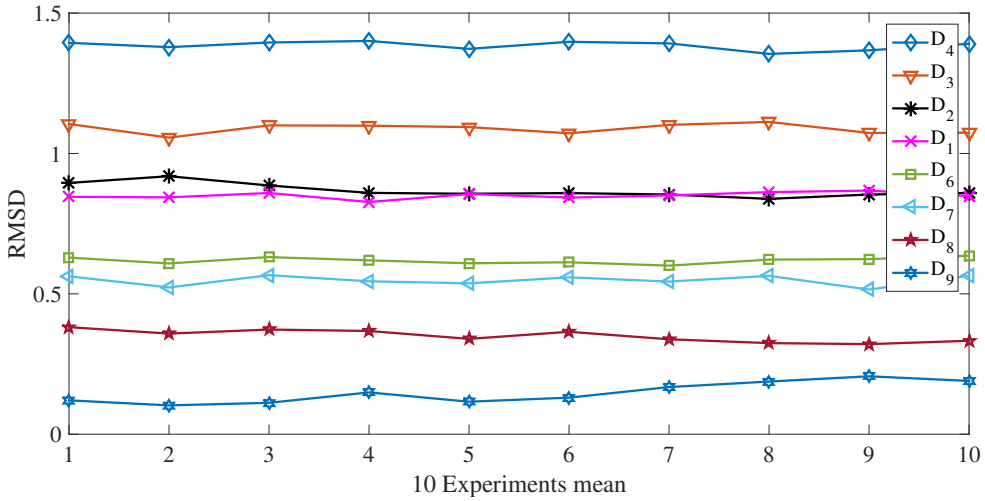

Fig. 6.8 Experimental Ten-averaged RMSD values for the studied cases

there are no variations of acoustic impedance in the contact area created by the matching micro-asperities generating the absence of material discontinuities for the transmission of the ultrasonic waves [89]. In numerical analysis, a real contact in metallic interfaces (no perfect) is not an easy task to model, a simple version of the contact area is implemented in the performed simulations.

A 3D FEM model was built representing a scaled but equivalent version of the experimental setup to reduce the size of the FEM model and consequently the computational cost. The steel pipe of 1 inch schedule 40 (outer diameter: 33.4 mm and wall thickness: 3.38 mm) is modeled as a hollow cylinder with an axial length of 0.4 m. The simple support is represented by a steel plate of 6 mm of thickness and with the same material as the pipe, two boundary conditions in the cylinder constrain the displacement in $y-direction$ of both extremes of the cylinder. Changes in support stiffness are configured varying the magnitude of a vertical concentrated force in upward direction situated in the middle part of the plate as shown in Figure 6.10.

The material properties used for steel were assumed as follows: Density ρ = 7830 kg/m3, Young's modulus (E) = 210 GPa and Poisson's ratio ν = 0.3. To ensure an adequate mesh refinement level, the minimum allowed inter-nodal length L_{min} is calculated. The lowest phase velocity C_T (i.e., transverse or shear wave speed), and consequently the shortest wavelength establishes the minimum permissible mesh size so spatial aliasing due to the finite element discretization does not occur [48]. Considering the frequency and the steel

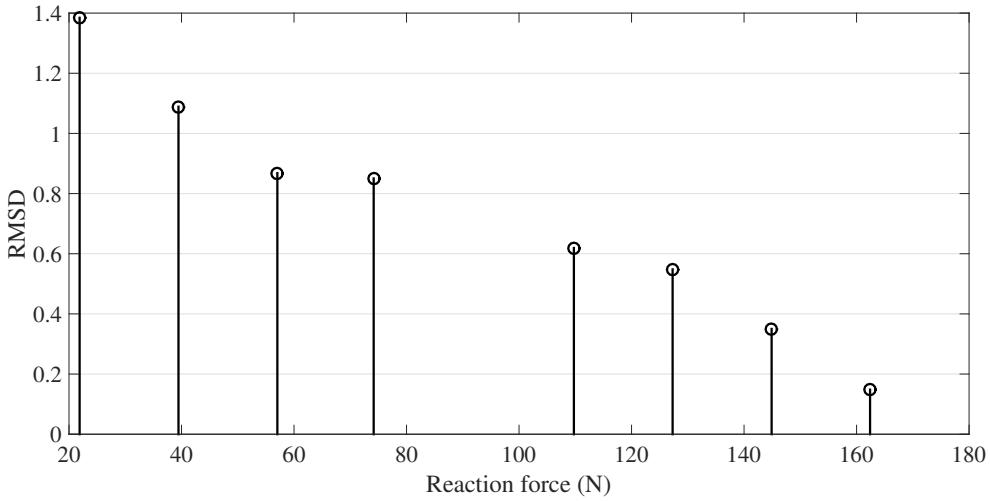

Fig. 6.9 Experimental results of RMSD versus Reaction force between pipe and support

shear wave velocity, L_{min} is calculated as follows:

$$L_{min} = \frac{C_T}{n_{min} f_{max}} = \frac{\lambda_{min}}{n_{min}}, \tag{6.18}$$

where, n_{min} is the number of elements across the smallest wavelength of interest (assumed in this case as $n_{min} \geq 10$) [73], and f_{max} the maximum frequency of interest. Considering $n_{min} = 15$, $f_{max} = 3200$ Hz and $C_T = 3200$ m/s, the minimum element length results, approximately 6.66 mm. Therefore, seeds size of 2 mm can be considered as a sufficient mesh refinement. In addition, for time domain models solved with an explicit scheme, an adequate integration time step Δt assures a more accurate solution. In general, simulation accuracy can be increased with increasingly smaller integration time steps but punished by a higher computational cost. So, the time step Δt has to be smaller than the critical time step Δt_{cr} which is the transit time of a dilatational wave through the smallest element in the model can be calculated as follows [25]:

$$\Delta t \leq \Delta t_{cr} = \frac{L_{min}}{C_L}, \tag{6.19}$$

where C_L is the velocity of the dilatational wave. A Δt of 5ns meets these criterion (Considering $L_{min} = 2\ mm$ and $C_L = 5944\ m/s$) and it is used to solve the model. A total of 9980 linear eight node brick element (C3D8) has been used with 52 elements around the circumferential section of the pipe.

The torsional wave is produced by a shear load at the left end face of the cylinder by a 5 cycles Hanning-window tone burst of 32 kHz. The model is configured such as the torsional wave freely propagates along the z-axis for 50 mm until a contact with the simple

support. A 12 mm contact line is established between the pipe and the support. The whole length of the pipe model is 0.2 m with a mesh of 9980 C3D8 elements and 104 semi-infinite CIN3D8 elements. In Figure 6.10, a schematic representation of the simulated geometry is presented. The latter elements are used at the cylinder right face to avoid reflections (absorbing boundary) [73]. The torsional wave propagates continuously into the absorption elements without any reflection.

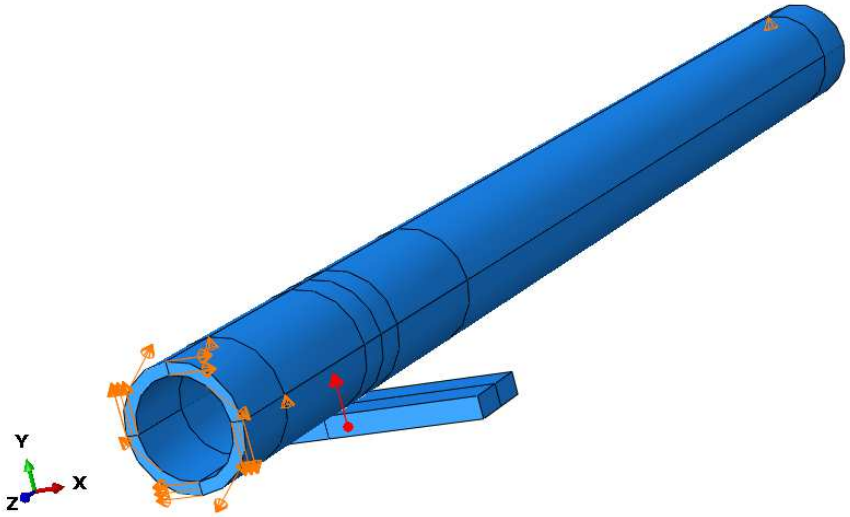

Fig. 6.10 Schematic representation of the simulated pipe with a simple support

A key aspect of the problem at hand is the surface contact FEM modeling between the pipe and simple support. This part of the modeling must be exhaustively considered in order to derive the most realistic acoustic coupling. Nevertheless, it is worth noting that though the connection between applied force and the transmission of ultrasonic waves from the interface is qualitatively known, it is not so easy to establish a general quantitative relationship, since too many parameters (surface roughness, type of material and frequency of incident wave) influence the phenomena. The acoustic interaction between two bodies in mechanical contact is a relatively complex model, therefore several simplifying assumptions are made: The Contact between the two surfaces is assumed to have smooth surfaces, applied normal stress within the elastic limits of their materials and contact surface be non-conformable.

Now, Considering a portion of pipeline lying on a simple support, represented as a plate, such as that shown in Figure 6.10. A idealized contact interface (line) occurs between the two specimens with an extent l along the axial direction of the pipe, a width w along the pipe perimeter. In Hertzian contact theory, two stiffness must be defined, a normal stiffness S_n that acts in the radial direction, and a tangential stiffness S_t that acts in the θ and z directions.

In order to simplify the use of the Hertzian contact theory the assumption of non-conformable contact between the two bodies is assumed, i.e. both surface keep their shape around the contact zone during the contact. In practice, this assumption is not realistic because under loading, the plate may curve around the pipe, or the pipe may flatten around the contact zone depending on their stiffness. In such case, the contact model increases its degree of complexity since the contact stiffness can vary considerably along the interface. This complex model is beyond to the scope of the study of the acoustic coupling between the fundamental torsional mode $T(0,1)$ and the $SH0$ mode of a plate.

Because the contact is assumed to occur in a line, infinitely long cylinders with parallel axes come into contact; away from end effects, the (2D) Hertzian theory must be used. Hertzian approach provides the width in the interface of the contact area when a normal load is applied to the contact surface. Assuming Young's modulus and Poisson ratio is close enough in magnitude between the two bodies in contact. The following expression is used to determine the width of the contact area:

$$w = \sqrt{\frac{8FR^*}{eE^*}}, \tag{6.20}$$

where F, also referred as contact loading, is the total normal force by the two bodies are pressed together along the interface length e, E^* is the contact module and R^* is the relative radius between the two bodies, determined by:

$$\frac{1}{R^*} = \frac{1}{R_1} + \frac{1}{R_2}. \tag{6.21}$$

Note, Equation (6.21) is originally expressed for an interface between two cylinders, where R_1 and R_2 are, respectively, the radius of the first and second cylinder. Notice, for the studied case, the contact interface is produced by a cylinder (pipe) of exterior radius R_1, and a plate with R_2 tends to infinity. Therefore, The relative radius R^* is R_1. The contact modulus E^* for the same material is given by

$$E^* = \frac{E}{2(1-\nu^2)} \tag{6.22}$$

The interface width obtained by Equation (6.20) to simulate contact between the 1" pipe and the plate of (6x9x20 mm), result be smaller than the gap between nodes (mesh size) used for the guided wave simulation. So, the interface width is assumed as a line of shared nodes between the cylinder and the plate.

Contact treatment is internally represented by linear springs between the slave nodes (plate) and the nearest master segments (pipe). The stiffness of these springs determines

the force that will be applied to the slave nodes and the master nodes. The mathematical model chosen to enforce the contact compatibility is the penalty method which requires the estimation of normal and tangential contact stiffness. In [34], it is reported that normal interface stiffness S_n for contact between two bodies of identical material properties is given by:

$$S_n = \frac{\pi e}{2\left(\frac{1-\nu^2}{E}\right)d^* - \frac{1}{E^*}}, \tag{6.23}$$

where,

$$d^* = 2\ln\left(\frac{4d}{w}\right) - 1, \tag{6.24}$$

$d = 2R_1$. Although, there is a lack of knowledge with respect to the small-scale properties and the small-scale dynamics of the contact interface, one of the most convenient ways to establish a realistic value for the tangential stiffness of a contact interface is to use empirical models such as the one for contact between rough surface using ultrasonic method developed by [63]

$$\frac{S_t}{S_n} = \frac{2(1-\nu)}{2-\nu} \tag{6.25}$$

Equation (6.25) describes a constant ratio between tangential and normal stiffness. It is acknowledged that there is not an effective analytical method to determine contact properties when the bodies in contact are real. So, here it is assumed values close to the obtained by the expressions cited above and checking the result against experimental evidence.

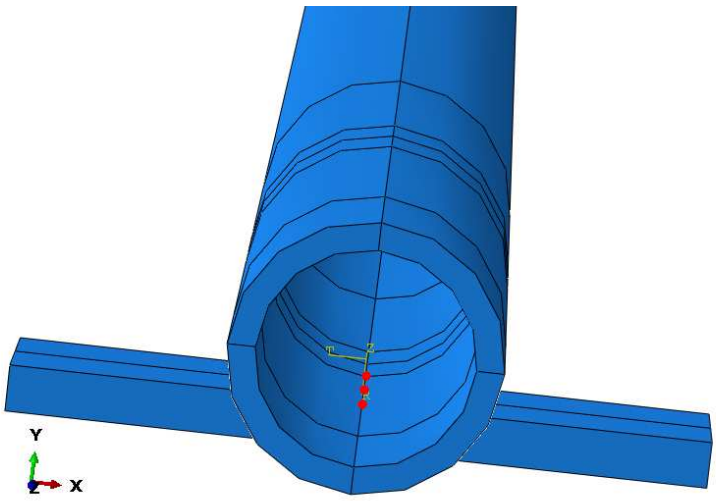

Fig. 6.11 Coupling nodes in the simulated contact interface

Some details of the contact implementation are the following: The interface between cylinder and plate is performed by a surface-surface contact and their interaction is achieved using a dynamic coupling between the nodes belonging to the contact line as presented in Figure 6.11. Discretization of the contact area into elementary units (contact nodes) is responsible for the contact stress (strain) acoustic transmission of the guided wave from pipe to support. The node to node discretization is appropriate for ultrasonic transmission problems because this method is suitable for small deformations and small slip. Although, both materials are modeled with the same mechanical properties, the pipe is assumed as master surface and the support as slave. Besides, a linear behavior of the Pressure-Overclosure relation is assumed.

The Finite Element Analysis (FEA) has been performed to study the effect of the supports stiffness (plate) in the transmitting potential of ultrasound energy through the contact interface between the cylinder and plate. $T(0,1)$ mode primarily has a tangential displacement U_θ which is transmitted by coupling to the plate. As previously mentioned, the frequency spectrum of $T(0,1)$ has the same shape as for *SH* waves in a plate. In fact, the torsional modes for a cylindrical waveguide are considered the analogue of the *SH* plate modes [46]. Thus, for the studied case is highly likely the generation of *SH* waves in the support.

The FEM simulation results of the interaction between cylinder and plate when a torsional guided wave $T(0,1)$ mode is propagating is presented in Figure 6.12. This Figure reveals that when the $T(0,1)$ mode impinges on the support, some portion of the ultrasound energy is transmitted to the plate producing *SH* lamb waves.

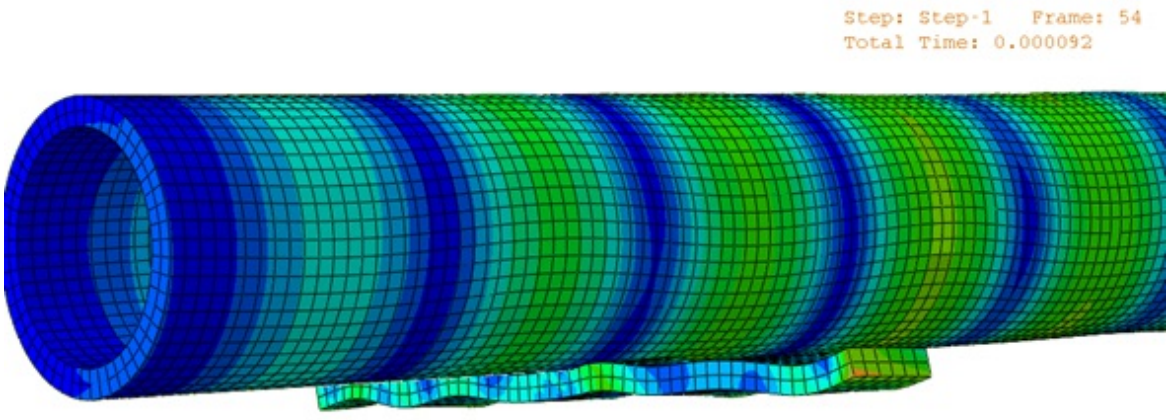

Fig. 6.12 Snapshots of $T(0,1)$ mode propagation in a pipe with a simple support

In Figure 6.13, it is depicted the generated wavepacket in the plate, it is identified as a SH_0 mode by using three different tests. First, the calculation of the phase velocity of the generated pulse belongs to velocity of the SH_0 mode reported in the dispersion curves. Second, although in Figure 6.13, the generated pulse seems dispersive, variations in the wave pattern are attributed to plate edge reflections. Shorter time period FEM simulations, (not showed here) reveals a non-dispersive behavior. Lastly, after several simulations by using different plate thickness, in all cases the magnitude of the SH_0 phase velocity is constant and equal to the velocity of the shear wave. Therefore, SH_0 phase velocity is independent to plate thickness.

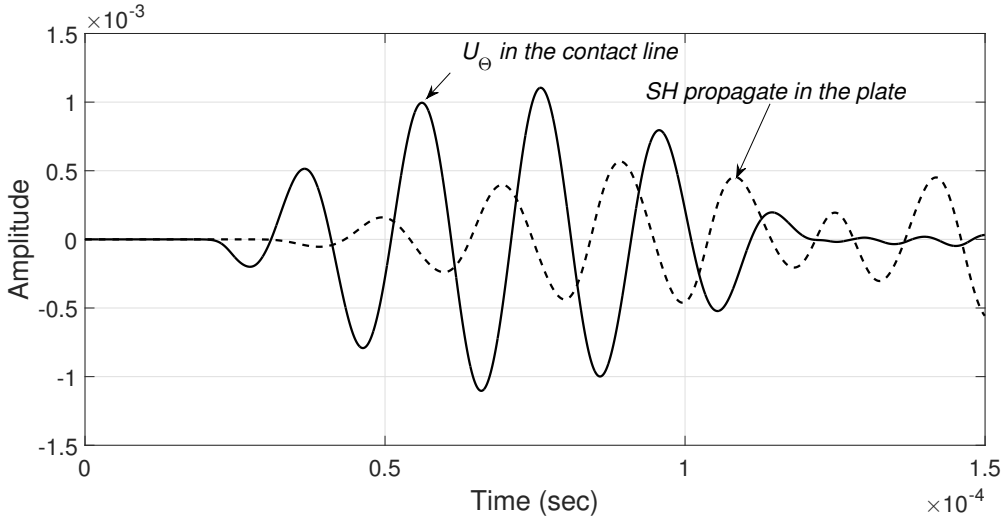

Fig. 6.13 $SH0$ generated in the plate for mode conversion of $T(0,1)$

On the other hand, as long as the contact force between pipe and support is increasing, a higher ultrasonic energy is transmitted to the plate in the shape of SH_0 waves. This fact is revealed in Figure 6.15; where it is noted an amplitude reduction in the captured pulse for a node which it is set up as a sensor in the model; for loads which emulate different support stiffness i.e. (0, 100, 200 and 500 N). Although in Figure 6.15 the zoom view correspond to the highest peak, the described behavior, decrease of the wave magnitude, is presented along the simulated $T(0,1)$. So, a reduction of the reaction force between the pipe and the support by a loss of rigidity in the support foundation produces an increase with respect to a pre-defined stiffness in the magnitude of the $T(0,1)$ captured pulse located ahead the support contact area.

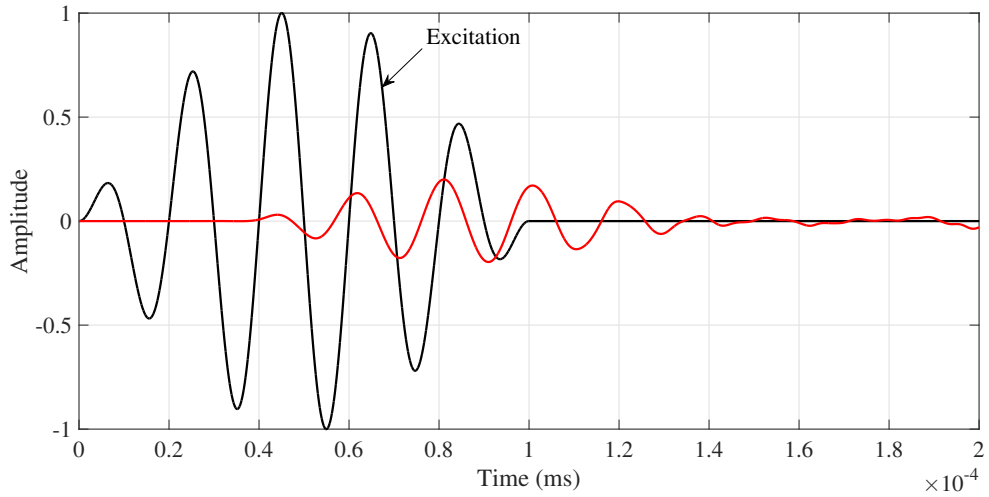

Fig. 6.14 Numerical results of $T(0,1)$ mode captured at 0.12 m of the excitation surface and at 0.07 m of the interaction point between support and pipe for the nominal condition

6.6 Discussion

The effects of supports external loading, stiffness, on the propagation of torsional guided wave mode $T(0,1)$ was investigated. Experimental tests were conducted for various magnitudes of loading in a one-inch sch 40 pipe. Experimental results showed an unnoticeable influence of pipe normal stress levels, generated by bending, in the velocity of the $T(0,1)$ mode as a consequence of the acoustoelasticity effect. No change in the TOF were reported among the different stress levels under loading varying reactions in the supports. FEM simulations of the effect of the mechanical contact between pipe and support in the propagation of $T(0,1)$ revel a mode conversion in the interface from $T(0,1)$ propagating in the pipe to SH_0 generated in the support, modeled as a plate. The leakage is identified comparing the magnitude of $T(0,1)$ propagating with and without mechanical contact with the support. No damping is considered in both conditions. Experimental results exposed amplitude change of the captured torsional guided wave for different stiffness in the supports. Although, the setup is plenty of symmetry (geometry of the waveguide, in loads, in the guided wave propagated, in the energy and stress distribution in the cross-section) the only asymmetric effect was the variations in the amplitude of the captured torsional wave. It is noted an attenuation growth in the transmitted wave for an increment of the supports reaction force, independent of the shape adopted by the pipe, i.e. concave upwards and concave downwards. Additionally, scattering, variations in the thickness, notches are absent in the experimentation performed. Based on these, it can be concluded that the mechanism responsible of the variations of the magnitude in mode $T(0,1)$ transmitted in a pipe in mechanical contact with a support is the

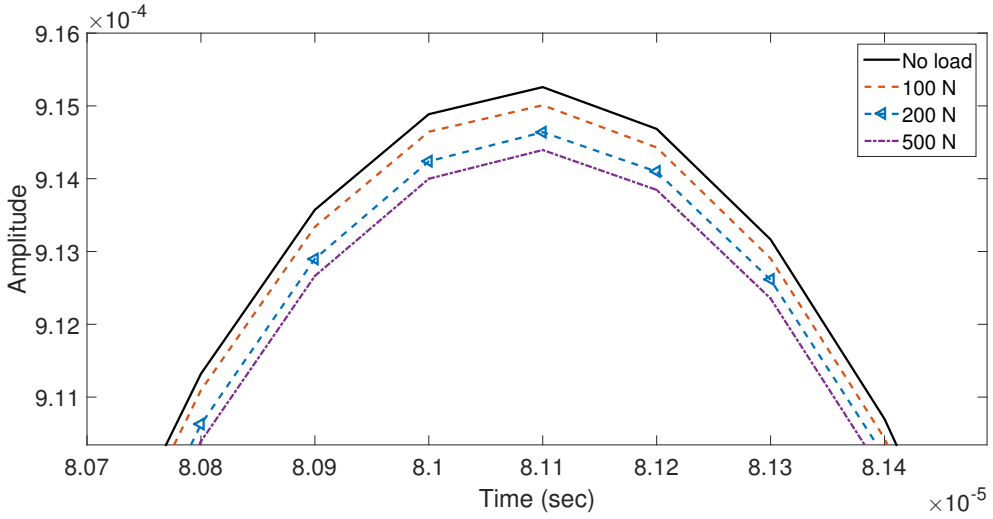

Fig. 6.15 Zoom view of the highest pulse of the simulated signals for different loads in the plate

transmitted ultrasonic energy for the guided wave to the support via mode conversion from $T(0,1)$ to SH_0 in the support. On the other hand, the presence of geometrical and material acoustic discontinuities in the guided waves such as notches, changes in the dimensions of the members cross section, corrosion or erosion, produce a reduction of the transmitted energy due to the interaction of the wave with the discontinuity (scattering, mode conversion, reflection). For all the cases, the energy reflection and mode conversion will produce a decrease in magnitude in the wave transmitted past the discontinuity. So, any ultrasound wavepacket magnitude increment for a pitch-catch configuration located in the path of a support with nonexistence of an extra ultrasound source must be unequivocally considered as a loss of rigidity in the support. Besides, the material discontinuities appear in the waveguide in a much greater time scale compared to the most probable scenario of unexpected change in the supports reaction. Therefore, it can be proposed a dedicated supports stiffness monitoring scheme which basis is the tracking of short time amplitude increments of $T(0,1)$ mode propagated in the path of the support.

Chapter 7

Conclusions and future work

7.1 Concluding remarks

This thesis was focused on developing a stress monitoring scheme, mainly in cylindrical structures, based on guided waves and using statistical tools (PCA) and signal processing in time domain (Residuals). In addition, experimentally and analytically the influence of stress and temperature in the proposed monitoring scheme was investigated. An experimental setup was implemented by employing two types of actuation principles: piezoelectricity and magnetostriction. The first one permitted to generate longitudinal and flexural guided waves in the specimen and the second one, the fundamental torsional mode only.

Initially, mechanical stress monitoring is tackled using an intuitive scheme, the signal-based approach. Different stress conditions in the specimen under investigation influence the information carried by the guided wave. Thus, subtracting the actual guided wave from a reference may provide symptoms of abnormal conditions. Experimental results demonstrate an additional requirement of post-processing (RMS and the residuals peak location) to obtain enough information to produce a stress change detection. However, this approach is highly affected by the temperature, for this reason, it was required to explore a new scheme, more sophisticated, capable to contain wave field information of the nominal state for different room temperatures.

Then, PCA is introduced as a promising tool for stress monitoring in cylindrical specimens (pipe and rod) subject to a stress distribution constant over the cross-section, in the case of the rod, and to a stress distribution variable with respect to the cross-section and distance of propagation for the pipe under bending. The launched pulse, although it is variable with the distance (dispersion), it is rich in information and justify the implementation of a data-driven scheme. Now, detection of abnormal conditions based on the guided wave pattern is highly sensitive to the environmental conditions such as temperature. Thus, a temperature

PCA-based stress robust monitoring scheme is proposed and evaluated by using an extended base of knowledge which correspond to the guided wave field of the nominal condition at different temperatures, all of them in a temperature range close to real environmental conditions. Effective detection and estimation of different stress levels under different room temperatures was verified at laboratory scale.

In order to exhaustively study the influence of stress in the guided wave propagation velocity (Acoustoelasticity effect), a new approximate scheme FEM-based was explored to determine the dispersion curves of stressed guided waves. Results reveal the complexity of evaluating changes of velocity in the propagation of multimode wave fields due to a distinct influence of stress in each mode. This result validates the requirement of data-driven tools for stress monitoring when the guided wave pattern is influenced by dispersion, is multimode and the wave propagation presents overlapping by the shape of the waveguide.

Next, The influence of changes in the support stiffness on the propagation of torsional mode $T(0,1)$, generated via a magnetostrictive transducer, was studied. Tests revealed unnoticeable influence of the generated bending stress condition in the velocity of the torsional wave transmitted.

Numerical analysis of the mechanical contact between pipe and support showed a mode conversion from $T(0,1)$ to SH_0 and a consequent energy leakage from the pipe to the support revealed by amplitude reduction with the increment of the contact force in the interface between pipe and support.

Finally, based on tracking the amplitude of the captured pulse after the support a support stiffness monitoring scheme is proposed . This monitoring scheme was the initial thesis motivation. This scheme is inherently robust because all material discontinuities produce an amplitude decreasing (energy transformation) in the transmitted guided wave. So, $T(0,1)$ magnitude increment with absent of an ultrasound source must be unequivocally considered as a loss of rigidity in the support.

7.2 Suggestion for future work

This research work has presented various techniques for stress monitoring using guided waves. This work has laid the foundation for future investigations to extend the methodologies to more complicated structures and explore some aspects beyond the scope of this thesis. The suggestions for future work are listed below:

- Influence of adhesive layer aging in the ultrasonic wave transmitted to the specimen
- Effect of the humidity in a dedicated PCA-based stress monitoring scheme

- Dispersion curves estimation in cylindrical waveguides using SAFE and EEC
- The use of T(0,1) mode to monitoring mechanical loosen in different cylindrical structures
- Study of the effect of external mechanical stress in the performance of PZT and magnetostrictive transducers via FEM simulation
- Investigate energy leakage of the T(0,1) mode into the surrounding material and its influence in the proposed stiffness monitoring scheme.
- Validation of the proposed stiffness monitoring scheme on an industrial scale

References

[1] Allen, D. and Sayers, C. (1984). The measurement of residual stress in textured steel using an ultrasonic velocity combinations technique. *Ultrasonics*, 22(4):179–188.

[2] Andhavarapu, E., Loveday, P. W., Long, C. S., and Heyns, P. S. (2010). Accuracy of semi-analytical finite elements for modelling wave propagation in rails. *Proc. Seventh South African Conference on Computational and Applied Mechanics (SACAM10)*, pages 1–11.

[3] Andrews, J. (2007). *Lamb Wave Propagation in Varying Thermal Enviroments*. Master thesis of science in astronautical engineering, Air Force Institute of Technology Air.

[4] Andruschak, N., Saletes, I., Filleter, T., and Sinclair, A. (2015). An NDT Guided wave technique for the identification of corrosion defects at support locations. *NDT & E International*, 75:72–79.

[5] Armenakas, A., Gazis, D., and Herrmann, G. (1969). *Free Vibrations of Circular Cylindrical Shells*. Pergamon Press, london, 1 edition.

[6] Auld, B. (1973). *Acoustic Fields and Waves in Solids. Vol. II*. Wiley-Interscience, Stanford, California, 1 edition.

[7] Bartoli, I., Marzani, A., Lanza di Scalea, F., and Viola, E. (2006). Modeling wave propagation in damped waveguides of arbitrary cross-section. *Journal of Sound and Vibration*, 295(3-5):685–707.

[8] Beard, M. D., Lowe, M. J. S., and Cawley, P. (2003). Ultrasonic Guided Waves for Inspection of Grouted Tendons and Bolts. *Journal of Materials in Civil Engineering*, 15(June):212–218.

[9] Bocchini, P., Asce, M., Marzani, A., and Viola, E. (2011). Graphical User Interface for Guided Acoustic Waves. *Journal of Computing in Civil Engineering*, 25(June):202–210.

[10] Boller, C., Chang, F., and Fujino, Y. (2009). *Encyclopedia of Structural Health Monitoring*.

[11] Bosher, S. H. B. and Dunstan, D. J. (2005). Effective elastic constants in nonlinear elasticity. *Journal of Applied Physics*, 97(10):1–7.

[12] Buethe, I., Torres-Arredondo, M. A., Mujica, L. E., Rodellar, J., and Fritzen, C. P. (2012). Damage detection in piping systems using pattern recognition techniques. In *Proceedings of the 6th European Workshop - Structural Health Monitoring 2012, EWSHM 2012*, volume 1, pages 624–631.

[13] Chaki, S. and Bourse, G. (2009a). Guided ultrasonic waves for non-destructive monitoring of the stress levels in prestressed steel strands. *Ultrasonics*, 49(2):162–171.

[14] Chaki, S. and Bourse, G. (2009b). Stress level measurement in prestressed steel strands using acoustoelastic effect. *Experimental Mechanics*, 49(5):673–681.

[15] Chaki, S., Corneloup, G., Lillamand, I., and Walaszek, H. (2007). Combination of Longitudinal and Transverse Ultrasonic Waves for In Situ Control of the Tightening of Bolts. *Journal of Pressure Vessel Technology*, 129(3):383.

[16] Cheeke, D. (2002). *Fundaments and Applications of Ultrasonic Waves*, volume 2. CRC Press, Boca Raton, second edition.

[17] Chen, B. and Zang, C. (2009). Artificial immune pattern recognition for structure damage classification. *Computers and Structures*, 87(21-22):1394–1407.

[18] Chen, F. and Wilcox, P. D. (2007). The effect of load on guided wave propagation. *Ultrasonics*, 47(1-4):111–122.

[19] Cheng, J.-W., Yang, S.-K., and Li, B.-H. (2007). Guided wave attenuation in clamp support mounted pipelines. *Materials evaluation*, 65(3):317–322.

[20] Colombo, S., Giannopoulos, A., Forde, M. C., Hasson, R., and Mulholland, J. (2005). Frequency response of different couplant materials for mounting transducers. *NDT and E International*, 38(3):187–193.

[21] Croxford, A., Wilcox, P., Drinkwater, B., and Konstantinidis, G. (2007). Strategies for guided-wave structural health monitoring. *Proceedings of the Royal Society A: Mathematical, Physical and Engineering Sciences*, 463(2087):2961–2981.

[22] Demma, A. (2003). The interaction of guided waves with discontinuities in structures. *Mechanical Engineering*, (January).

[23] di Scalea, F. L. and Rizzo, P. (2003). Stress measurement and defect detection in steel strands by guided stress waves. *Journal of materials in civil engineering*, 15(June):219.

[24] Ditri, J. J. and Rose, J. L. (1992). Excitation of guided elastic wave modes in hollow cylinders by applied surface tractions. *Journal of Applied Physics*, 72(7):2589–2597.

[25] Drozdz, M. B. (2008). *Efficient Finite Element Modelling of Ultrasound Waves in Elastic Media*. PhD thesis, University of London.

[26] Dubuc, B., Ebrahimkhanlou, A., and Salamone, S. (2017). Effect of pressurization on helical guided wave energy velocity in fluid-filled pipes. *Ultrasonics*, 75(November):145–154.

[27] Dugmore, K., Jonson, D., and Walker, M. (2002). A comparison of signal consistency of common ultrasonic couplants used in the inspection of composite structures. *Composite Structures*, 58(4):601–603.

[28] Duquennoy, M., Ouaftouh, M., Devos, D., Jenot, F., and Ourak, M. (2008). Effective elastic constants in acoustoelasticity. *Applied Physics Letters*, 92(24):1–3.

[29] Farrar, C. R. and Worden, K. (2007). An introduction to structural health monitoring. *Philosophical transactions. Series A, Mathematical, physical, and engineering sciences*, 365(1851):303–315.

[30] Fritzen, M. A., Tibaduiza, D. A., Torres-Arredondo, M. A., Pozo, F., Ruiz, M., Mujica, L. E., Rodellar, J., and Claus-Peter (2014). Data-driven methodology to detect and classify structural changes under temperature variations. *Smart Materials and Structures*, 23(4):45006.

[31] Galán, J. M. and Abascal, R. (2002). Numerical simulation of Lamb wave scattering in semi-infinite plates. *International Journal for Numerical Methods in Engineering*, 53(5):1145–1173.

[32] Galán, J. M. and Abascal, R. (2003). Elastodynamic guided wave scattering in infinite plates. *International Journal for Numerical Methods in Engineering*, 58(7):1091–1118.

[33] Galvagni, a. and Cawley, P. (2011a). The reflection of guided waves from Circumferential Notches in Pipes. *The Journal of the Acoustical Society of . . .* , 129(September):1869–1880.

[34] Galvagni, A. and Cawley, P. (2011b). The reflection of guided waves from simple supports in pipes. *journal of Acoustic Society*, 129(4):1869–1880.

[35] Gandhi, N. (2010). *Determination of dispersion curves for acoustoelastic lamb wave propagation*. PhD thesis, Georgia Institute of Technology.

[36] Gandhi, N., Michaels, J. E., and Lee, S. J. (2011). Acoustoelastic lamb wave propagation in a homogeneous, isotropic aluminum plate. *AIP Conference Proceedings*, 1335(2011):161–168.

[37] Gandhi, N., Michaels, J. E., and Lee, S. J. (2012). Acoustoelastic Lamb wave propagation in biaxially stressed plates. *The Journal of the Acoustical Society of America*, 132(3):1284–93.

[38] Gao, H. (2007). *Ultrasonic guided wave mechanics for composite material structural health monitoring (Doctoral dissertation)*. PhD thesis, The Pennsylvania State University.

[39] Gazis, D. (1959). Three-Dimensional Investigation of the Propagation of Waves in Hollow Circular Cylinders. *The Journal of the Acoustical Society of America*, 31(5):573–578.

[40] Gharibnezhad, F. (2014). *Robust Damage Detection in Smart Structures*. PhD thesis, Technical University of Catalunya.

[41] Gharibnezhad, F., Mujica, L. E., and Rodellar, J. (2015). Applying robust variant of Principal Component Analysis as a damage detector in the presence of outliers. *Mechanical Systems and Signal Processing*, 50-51:467–479.

[42] Gharibnezhad, F., Mujica, L. E., Rodellar, J., and Fritzen, C. (2012). Damage Detection Using Robust Fuzzy Principal Component Analysis. In *6th European Workshop on Structural Health Monitoring*, pages 1–8.

[43] Gharibnezhad, F., Mujica, L. E., Rodellar, J., and Todd, M. (2014). Fuzzy Similarity Classifier as damage index : Temperature effect and compensation. *EWSHM - 7th European Workshop on Structural Health Monitoring*, pages 1325–1332.

[44] Giurgiutiu, V., Yu, L., and Thomas, D. (2004). Embedded ultrasonic structural radar with piezoelectric wafer active sensors for damage detection in cylindrical shell structures BT - Collect. of Pap. - 45th AIAA/ASME/ASCE/AHS/ASC Struct., Struct. Dyn. and Mater. Conf.; 12th AIAA/ASME/AHS Adapt. Struct. 7:4984–4997.

[45] Gopalakrishnan, S., Chakraborty, A., and Mahapatra, D. R. (2008). *Spectral Finite Element Method*.

[46] Graff, K. (1975). Wave Motion in Elastic Solids,.

[47] Gravenkamp, H. (2016). A remark on the computation of shear-horizontal and torsional modes in elastic waveguides. *Ultrasonics*, 69:25–28.

[48] Han, S. (2007). *Finite Element Analysis of Lamb Waves*. PhD thesis, Department of Aeronautical and Astronautical Engineering.

[49] Han, X., Liu, G. R., Xi, Z. C., and Lam, K. Y. (2002). Characteristics of waves in a functionally graded cylinder. *International Journal for Numerical Methods in Engineering*, 53(3):653–676.

[50] Hayashi, T. (2004). Guided wave animation using Semi-Analytical Finite Element method. Technical report.

[51] Hayashi, T. and Inoue, D. (2014). Calculation of leaky Lamb waves with a semi-analytical finite element method. *Ultrasonics*, 54(6):1460–1469.

[52] Hayashi, T., Kawashima, K., Sun, Z., and Rose, J. L. (2005). Guided Wave Propagation Mechanics Across a Pipe Elbow. *Journal of Pressure Vessel Technology*, 127(3):322.

[53] Hayashi, T., Song, W. J., and Rose, J. L. (2003). Guided wave dispersion curves for a bar with an arbitrary cross-section, a rod and rail example. *Ultrasonics*, 41(3):175–183.

[54] Hot, A., Kerschen, G., Foltête, E., and Cogan, S. (2012). Detection and quantification of non-linear structural behavior using principal component analysis. *Mechanical Systems and Signal Processing*, 26(1):104–116.

[55] Huang, B., Koh, B.-H., and Kim, H. S. (2014). PCA-based damage classification of delaminated smart composite structures using improved layerwise theory. *Computers & Structures*, 141:26–35.

[56] Huang, S. and Wang, S. (2016). *Electromagnetic Ultrasonic Guided Waves*.

[57] Hughes, D. and Kelly, J. (1953). Second-Order Elastic Deformations of Solids. *Physical Review*, 92(5):1145–1150.

[58] Kannan, E., Maxfield, B. W., and Balasubramaniam, K. (2007). SHM of Pipes Using Torsional Waves Generated by In Situ Magnetostrictive Tapes. *Smart Materials and Structures*, 16(6):2505–2515.

[59] Khennane, A. (2013). *Introduction to Finite Element Analysis Using MATLAB® and Abaqus*.

[60] Kim, J. H. and Kwak, H.-G. (2011). Rayleigh wave velocity computation using principal wavelet-component analysis. *NDT & E International*, 44(1):47–56.

[61] Kim, Y. Y. and Kwon, Y. E. (2015). Review of magnetostrictive patch transducers and applications in ultrasonic nondestructive testing of waveguides. *Ultrasonics*, 62:3–19.

[62] Konishi, S. and Kitagawa, G. (2008). *Information Criteria and Statistical Modeling*.

[63] Królikowski, J. and Szczepek, J. (1993). Assessment of tangential and normal stiffness of contact between rough surfaces using ultrasonic method. *Wear*, 160(2):253–258.

[64] Lhémery, A., Calmon, P., Chatillon, S., and Gengembre, N. (2002). Modeling of ultrasonic fields radiated by contact transducer in a component of irregular surface. *Ultrasonics*, 40(1-8):231–6.

[65] Li, C., Han, Q., Liu, Y., Liu, X., and Wu, B. (2015). Investigation of wave propagation in double cylindrical rods considering the effect of prestress. *Journal of Sound and Vibration*, 353:164–180.

[66] Li, J. and Rose, J. L. (2006). Natural beam focusing of non-axisymmetric guided waves in large-diameter pipes. *Ultrasonics*, 44(1):35–45.

[67] Li, J. and Rose, R. L. (2001). Excitation and propagation of non-axisymmetric guided waves in a hollow cylinder. *The Journal of the Acoustical Society of America*, 109(2):457–464.

[68] Lillamand, I., Chaix, J. F., Ploix, M. A., and Garnier, V. (2010). Acoustoelastic effect in concrete material under uni-axial compressive loading. *NDT and E International*, 43(8):655–660.

[69] Loveday, P. W. (2009). Semi-analytical finite element analysis of elastic waveguides subjected to axial loads. *Ultrasonics*, 49(3):298–300.

[70] Loveday, P. W., Long, C. S., and Wilcox, P. D. (2012). Semi-Analytical Finite Element Analysis of the Influence of Axial Loads on Elastic Waveguides. In Moratal, D., editor, *Finite Element Analysis - From Biomedical Applications to Industrial Developments*, chapter 18, pages 439–454. InTech.

[71] Loveday, P. W. and Wilcox, P. D. (2010). Guided wave propagation as a measure of axial loads in rails. *Proc. SPIE*, 7650:765023–765028.

[72] Lowe, M. J. S. (1995). Matrix Techniques for Modeling Ultrasonic-Waves in Multilayered Media. *Ieee Transactions on Ultrasonics Ferroelectrics and Frequency Control*, 42(4):525–542.

[73] Lowe, P. S., Sanderson, R. M., Boulgouris, N. V., Haig, A. G., and Balachandran, W. (2016). Inspection of Cylindrical Structures Using the First Longitudinal Guided Wave Mode in Isolation for Higher Flaw Sensitivity. *IEEE Sensors Journal*, 16(3):706–714.

[74] Lu, Y. and Michaels, J. E. (2005). A methodology for structural health monitoring with diffuse ultrasonic waves in the presence of temperature variations. *Ultrasonics*, 43(9):717–731.

[75] Marzani, A. (2008). Time-transient response for ultrasonic guided waves propagating in damped cylinders. *International Journal of Solids and Structures*, 45(25-26):6347–6368.

[76] Mazzotti, M., Marzani, A., Bartoli, I., and Viola, E. (2012). Guided waves dispersion analysis for prestressed viscoelastic waveguides by means of the SAFE method. *International Journal of Solids and Structures*, 49(18):2359–2372.

[77] Mohrbacher, H. and Salama, K. (1993). The Temparature Dependence of Third-Order Elastic Constants in Metal-Matrix Composites. *Review of Quantitative Nondestructive Evaluation*, 12:2091–2097.

[78] Mojtahedi, A., Lotfollahi Yaghin, M., Ettefagh, M., Hassanzadeh, Y., and Fujikubo, M. (2013). Detection of nonlinearity effects in structural integrity monitoring methods for offshore jacket-type structures based on principal component analysis. *Marine Structures*, 33:100–119.

[79] Moser, F., Jacobs, L. J., and Qu, J. (1999). Modeling elastic wave propagation in waveguides with the finite element method. *NDT & E International*, 32(4):225–234.

[80] Muir, D. D. (2009). *One-Sided Ultrasonic Determination of Third Order Elastic Constants using Angle-Beam Acoustoelasticity Measurements*. PhD thesis, Georgia Institute of Technology.

[81] Mujica, L., Rodellar, J., Fernandez, A., and Guemes, A. (2011a). Q-statistic and T2-statistic PCA-based measures for damage assessment in structures. *Structural Health Monitoring*, 10(5):539–553.

[82] Mujica, L. E., Ruiz, M., Pozo, F., and Rodellar, J. (2011b). *Damage Detection Index Based on Statistical Inference and PCA*.

[83] Murayam, R. and Misumi, K. (2006). Development of a non-contact stress measurement system during tensile testing using the electromagnetic acoustic transducer for a Lamb wave. *NDT & E International*, 39(4):299–303.

[84] Murnaghan, F. (1937). Finite deformations of an elastic solid. *America Journal of Mathematics*, pages 235–260.

[85] Nikitina, N. and Ostrovsky, L. (1998). An ultrasonic method for measuring stresses in engineering materials. *Ultrasonics*, 35(8):605–610.

[86] Olabi, A. G. and Grunwald, A. (2008). Design and application of magnetostrictive materials. *Materials and Design*, 29(2):469–483.

[87] Ostachowicz, W., Kudela, P., Krawczuk, M., and Zak, A. (2012). *Guided Waves in Structures for SHM*.

[88] Palanichamy, P., Joseph, A., Jayakumar, T., and Raj, B. (1995). Ultrasonic velocity measurements for estimation of grain size in austenitic stainless steel. *NDT & E International*, 28(3):179–185.

[89] Pau, M., Aymerich, F., and Ginesu, F. (2002). Distribution of contact pressure in wheel-rail contact area. *Wear*, 253(1-2):265–274.

[90] Pavlakovic, B. N. (1998). Leaky Guided Ultrasonic Waves in NDT. *Dissertation*, (October).

[91] Qing, X. P., Chan, H. L., Beard, S. J., Ooi, T. K., and Marotta, S. A. (2006). Effect of adhesive on the performance of piezoelectric elements used to monitor structural health. *International Journal of Adhesion and Adhesives*, 26(8):622–628.

[92] Quiroga, J. E., Quiroga, J. L., Villamizar, R., and Mujica, L. E. (2015a). Application of the PCA to guided waves to evaluate tensile stress in a solid rod. In *Proceedings in IWSHM 2015*, pages 1814–1824, Stanford, California.

[93] Quiroga, J. L., Quiroga, J. E., and Villamizar, R. (2015b). Influence of the Coupling Layer on Low Frequency Ultrasonic Propagation in a PCA Based Stress Monitoring. In *6th Panamerican Conference for NDT*, pages 2–10, Cartagena, Colombia.

[94] Raghavan, A. (2007). *Guided-wave structural health monitoring*. PhD thesis.

[95] Rose, J. L. (2014). *Ultrasonic Waves in Solid Media*. Cambridge University Press.

[96] Satyarnarayan, L., Chandrasekaran, J., Maxfield, B., and Balasubramaniam, K. (2008). Circumferential higher order guided wave modes for the detection and sizing of cracks and pinholes in pipe support regions. *NDT and E International*, 41(1):32–43.

[97] Shi, F., Michaels, J. E., and Lee, S. J. (2012). An ultrasonic guided wave method to estimate applied biaxial loads. *Review of Progress in Quantitative NDE*, 1430:1567–1574.

[98] Shin, H. J. and Rose, J. L. (1999). Guided waves by axisymmetric and non-axisymmetric surface loading on hollow cylinders. *Ultrasonics*, 37(5):355–363.

[99] Sibilio, E., Ciampoli, M., and Beck, J. L. (2007). Structural health monitoring by Bayesian updating. (June):13–16.

[100] Sinou, J.-J. (2009). A review of damage detection and health monitoring of mechanical systems from changes in the measurement of linear and non-linear vibrations. *Mechanical Vibrations: Measurement, Effects and Control*, pages 643–702.

[101] Soh, C-k; Yang, Y., Bhalla, S., Soh, C., Yang, Y., and Bhalla, S. (2012). *Smart Materials in Structural Health Monitoring, Control and Biomechanics*, volume 1. Zhejiang University Press, Springer.

[102] Stobbe, D. (2005). *Acoustoelasticity in 7075-T651 Aluminum and Dependence of Third Order Elastic Constants on Fatigue Damage.* PhD thesis, Georgia Institute of Technology.

[103] Tibaduiza, D. A., Mujica, L. E., Anaya, M., and Rodellar, J. (2011). *Combined and I Indices Based on Principal Component Analysis for Damage Detection and Localization*.

[104] Tibaduiza, D. A., Torres-Arredondo, M. A., Mujica, L. E., Rodellar, J., and Fritzen, C. P. (2013). A study of two unsupervised data driven statistical methodologies for detecting and classifying damages in structural health monitoring. *Mechanical Systems and Signal Processing*, 41(1-2):467–484.

[105] Tindaro, C. (2009). *Signal Processing for Guided Wave Shm*. PhD thesis.

[106] Treyssède, F. (2016). Investigation of the interwire energy transfer of elastic guided waves inside prestressed cables. *The Journal of the Acoustical Society of America*, 140(1):498–509.

[107] Vinogrado, S., Eason, T., and Lozev, M. (2018). Evaluation of magnetostrictive transducers for guided wave monitoring of pressurized pipe at 200 ° C. *Journal of Pressure Vessel Technology, Transactions of the ASME*, 140(2).

[Viola and Marzani] Viola, E. and Marzani, A. Exact Analysis of Wave Motions in Rods and Hollow Cylinders.

[109] Viola, E. and Marzani, A. (2007). Mechanical Vibration: Where Do We Stand. In Elishakoff, I., editor, *International Centre for Mechanical Sciences*, pages 83–104.

[110] Wang, T., Song, G., Liu, S., Li, Y., and Xiao, H. (2013). Review of bolted connection monitoring. *International Journal of Distributed Sensor Networks*, 2013.

[111] Yan, A. M., Kerschen, G., De Boe, P., and Golinval, J. C. (2005). Structural damage diagnosis under varying environmental conditions - Part I: A linear analysis. *Mechanical Systems and Signal Processing*, 19(4):847–864.

[112] Yanf, S.-K., Lee, P.-H., Jeng, J.-J., and Cheng, J. W. (2007). Modeling the Interaction of Guided Wave with the welded Support in Pipes. In *14 International Conference on Sound & Vibration*, Cairns, Australia.

[113] Yang, S. K., Lee, J. H., Lee, P. H., and Cheng, J. W. (2006). The Effect of the Longitudinal Welded Support on the Pipe for Guided Wave Propagation. In *12th A-PCNDT 2006-Asian -Pacific Conference on NDT*, pages 2–7, Auckland, New Zeland.

[114] Yang, S.-K., Lee, P.-H., and Cheng, J.-W. (2009). Effect of Welded Pipe Support Brackets on Torsional Guided Wave Propagation. *Materials evaluation*, 67(8):935–944.

[115] Zhong, L., Song, H., and Han, B. (2006). Extracting structural damage features: Comparison between PCA and ICA. *Lecture Notes in Control and Information Sciences*, 345:840–845.

[116] Zhu, L., Wang, Y., and Sun, F. (2013). Single torsional guided wave excitation in pipes by frequency selection using magnetostrictive sensor technology. *Proceedings of 2013 IEEE 11th International Conference on Electronic Measurement and Instruments, ICEMI 2013*, 2:872–876.

[117] Zhu, Z. H., Post, M. A., and Meguid, S. A. (2012). The Potential of Ultrasonic Non-Destructive Measurement of Residual Stresses by Modal Frequency Spacing using Leaky Lamb Waves. *Experimental Mechanics*, 52(9):1329–1339.

[118] Zhuang, W., Shah, A. H., and Dong, S. B. (1999). Elastodynamic Green's Function for Laminated Anisotropic Circular Cylinders. *Journal of Applied Mechanics*, 66(3):665–674.

Appendix A

Expressions for the EEC proposed by [19]

$$C_{11}^{a} = k_2 + k_1\left[4\lambda + 10\mu + 4\nu_2 + 8\nu_3 + k_3\left(-2\mu + \nu_1 + 2\nu_2\right)\right] \tag{A.1}$$

$$C_{22}^{a} = C_{33}^{a} = k_2 + k_1\left[k_4 + k_3\left(\lambda + 2\mu + \nu_1 + 4\nu_2 + 4\nu_3\right)\right] \tag{A.2}$$

$$C_{44}^{a} = \mu + k_1\left[-2\mu - 2\nu_3 + k_3\left(\mu + \nu_2 + 2\nu_3\right)\right] \tag{A.3}$$

$$C_{55}^{a} = C_{66}^{a} = \mu + k_1\left[2\mu + \nu_3 + \left(1 - 2\nu\right)\left(\nu_2 + \nu_3\right)\right] \tag{A.4}$$

$$C_{12}^{a} = C_{13}^{a} = \lambda + k_1\left[\lambda + \nu_2 + k_3\left(\nu_2 + \nu_1\right)\right] \tag{A.5}$$

$$C_{23}^{a} = \lambda + k_1\left[-2\lambda - 2\nu_2 + k_3\left(\lambda + \nu_1 + 2\nu_2\right)\right] \tag{A.6}$$

Where λ and μ are the Lamé constants, ν_1, ν_2 and ν_3 are the Toupin and Berstein constants which are equivalent to $\nu_1 = n, \nu_2 = m - 0.5n$ and $\nu_3 = 1 - \nu_2$ in terms of Mourghanan (l, m, n) constants.